Stabilization and Aggregation of Preformed Silver Clusters in Room Temperature Ionic Liquids: A UV/Vis and X-Ray Absorption Spectroscopy Study

DISSERTATION

zur Erlangung des Doktorgrades der
Naturwissenschaften

vorgelegt von
Stefanie Roese

Lehrstuhl für Experimentelle Physik I
Fakultät Physik
Technische Universität Dortmund
November 2017

technische universität
dortmund

1. Gutachter: Prof. Dr. Heinz Hövel
2. Gutachter: Prof. Dr. Manfred Bayer

Contents

List of Figures

List of Tables

Chapter 1

Motivation

The reduction of particle sizes down to the nanoscale opens a new field of physics. The term "nanotechnology" was coined in the 1970s [Tan74]. Although nanotechnology is a quite young field of research, remarkable progress has already been achieved in interdisciplinary fields of science with a wide range of various application in medicine [Hae04; Pis06], catalysis [San99; Lu12; Tan12], sensor applications [Shi00; Fer09] and many more fields.

In order to explore the full potential of nanoparticles their characteristics and properties have to be understood. The fascinating physicochemical properties of nanoparticles, also referred to as clusters, are strikingly different from their bulk counterparts. Since fundamental research becomes more and more application orientated, for any application cluster stabilization is inevitable due to their aggregation-prone characteristics.

Ionic liquids, which are basically molten salts, have attracted enormous attention in both science and industry due to their fascinating properties [Ple08]. In particular, they have proven to be a suitable medium for cluster stabilization because of their electrosteric characteristics [Dup10; He15; Jan13; Weg17]. However, the stabilizing mechanism and the aggregation behavior are still subject of controversial discussions [Ric11; Van12; Dup02; Suz09; Fu17].

This thesis aims to contribute to the understanding of sample stability by introducing a new approach of using preformed silver clusters stabilized in ionic liquids, not accessible with other sample production methods. Sample aggregation is analyzed by combining two complementary experimental techniques. The interaction between clusters and ionic liquid is investigated using UV/Vis absorption spectroscopy and electrodynamic calculations, while the atomistic cluster arrangement during the sample aggregation process is monitored by X-ray absorption spectroscopy.

The outline of this work is as follows: **Chapter 2** introduces the physics of clusters as well as the comparably new class of solvents, namely ionic liquids, which offer a wide range of applications due to almost countless combinations of cations and anions. The current state of research on nanoparticles in ionic liquids is presented, illustrating the potential of using preformed clusters for discussing sample stability.

The laboratory setup, the cluster production in a supersonic expansion and the subsequent cluster deposition in the ionic liquid in a custom built mixer is presented in **chapter 3**.

Sample stability is investigated using two different experimental techniques. **Chapter 4** deals with the optical and electronic properties of the weakly bound electrons of the silver clusters. The interaction of the clusters, embedded in a dielectric medium, with light is described in the fundamental Mie theory, which can be extended to calculate the optical spectra of larger, arbitrarily formed aggregates numerically.

The results of the optical measurements obtained by UV/Vis absorption spectroscopy are presented in **chapter 5**. At first the spectra recorded during deposition are discussed in order to find optimal deposition parameters, leading to a stable sample with high cluster concentration. The ionic liquid - cluster interaction can directly be measured. Afterwards the temperature-dependent sample aggregation is studied and compared with theoretical Generalized Mie theory calculations. Varying the anion or cation of the ionic liquid can have dramatic influence on sample stability. The first experimental results of those experiments are presented at the end of this section.

The properties of tightly bound electrons are discussed in **chapter 6**. To reconstruct the geometric structure of ionic liquid stabilized clusters the absorption of X-rays by excitation of core level electrons is applied.

After introducing the experimental setup at beamline P64, the results of data analysis are presented in **chapter 7**. By combining two different analysis methods structural changes between separated and aggregated clusters can be investigated.

Combining both UV/Vis and X-ray absorption spectroscopy, conclusions regarding sample aggregation can be drawn. A summary and an outlook are finally given in **chapter 8**.

Chapter 2

Introduction

This chapter starts with a brief introduction into cluster physics, which offers a wide range of applications due to their remarkable properties and explains the associated need for cluster stabilization. Afterwards an overview about ionic liquids and a short historical summary is given. Ionic liquids have some outstanding properties and are a promising medium for cluster stabilization. Depending on their composition the properties of ionic liquids can alter significantly, this is why ionic liquids became a famous, new class of solvents for a broad range of applications. Some of their most relevant properties will be discussed.

Finally, the concept of ionic liquid stabilized clusters is introduced. In common preparation methods the cluster growth takes place by agglomeration inside the ionic liquid; compared to that an alternative approach is presented: the deposition of preformed clusters into ionic liquids. This approach involves that clusters with a well-known size distribution are investigated, which ensures that each change in the cluster-ionic liquid dispersion can be assigned to sample aggregation.

2.1 Clusters

The research field of cluster physics can be found between the physics of a single atom and condensed matter physics. Clusters are small, multi-atom particles that can consist of 3 to 1000 atoms, corresponding to particle sizes of 10^0 to 10^1 nm [Hab06]. In this thesis the term *clusters* is used to address nanoparticles of a well-defined size. Cluster physics studies the gradual evolution of collective phenomena that characterize a solid. Structure and thus electronic properties alter significantly with size and shape of the clusters as well as with environmental influences. Very interesting differences to the corresponding bulk material can be observed for particles smaller than 10 nm not only due to the larger surface to volume ratio. For example the conduction bands in the solid state consists of overlapping orbitals, while we find discrete energy levels for nanoparticles. The band gap is increasing for decreasing particle size [Sei91].

The study of metal clusters has led to remarkable scientific developments in the past decades. Due to the high percentage of surface atoms clusters have a large number of atoms interacting with the environment, which makes clusters potentially more active than currently used catalysts. The ability of producing clusters with different sizes, shapes, compositions, and surface structures resulted in a broad range of applications like biochemical sensors [Yua13; Liu13] or catalysis [Liu13; Lu12; Tan12] since they are considered as models for ideal surfaces [Did03]. Due to their potential in antibacterial applications especially silver clusters are of great interest [Ras11].

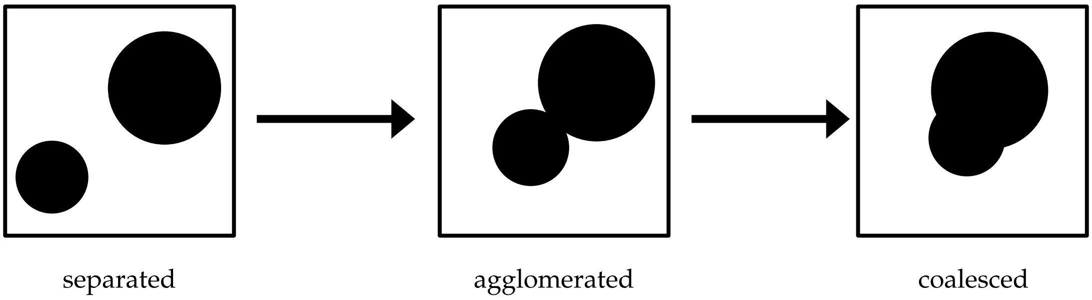

Figure 2.1: Schematics of cluster agglomeration and coalescence [Qui11].

For clusters, the surface atoms exhibit an unsaturated coordination sphere with a state of higher energy enabling the interaction with other atoms, which induces the lowering of their surface area (see figure 2.1). In general, this process will be denoted as aggregation. If the physical interaction between two clusters is weak, the process is called *agglomeration*. The clusters are joined together, but their total surface area does not noticeably differ from the sum of the individual primary clusters and the single cluster shape is not changed. However, if the clusters *coalesce*, the boundary between the particles disappears, resulting in a change of the primary particle shape and a decrease of the total surface area [Wal13].

Due to strong short range attractive forces between the clusters they tend to aggregate. Their aggregation-prone characteristics complicates the cluster production for applications. It is therefore inevitable to terminate the particle growth to produce stable nanoparticles. The stabilization of the surface requires long range repulsion, which needs to be at least as strong as the attractive forces. Several stabilization methods have been introduced and investigated in literature. The particles are surrounded by either adsorbed macromolecules (steric stabilization), by an electric double layer (electrostatic stabilization) or by a combination of both as schematically shown in figure 2.2.

Steric repulsion (figure 2.2a)) occurs, if macromolecules (for example polymers, thiols, alcohols or long alkyl-chain surfactants) are adsorbed on the particle surface. An encapsulating sphere around the cluster [Ast05] is formed. If two of those particles are approaching, their capping shell will be compressed, which results in a strong repulsion. This effect prevents the particles to get close together in the range of attractive forces [Lia07]. The stabilizer has to adsorb strong enough to the cluster surface in order to prevent desorption. Strongly adsorbing molecules with bulky structure are therefore prime candidates for the steric stabilization of clusters. The main drawback of those common stabilizing mechanisms is their

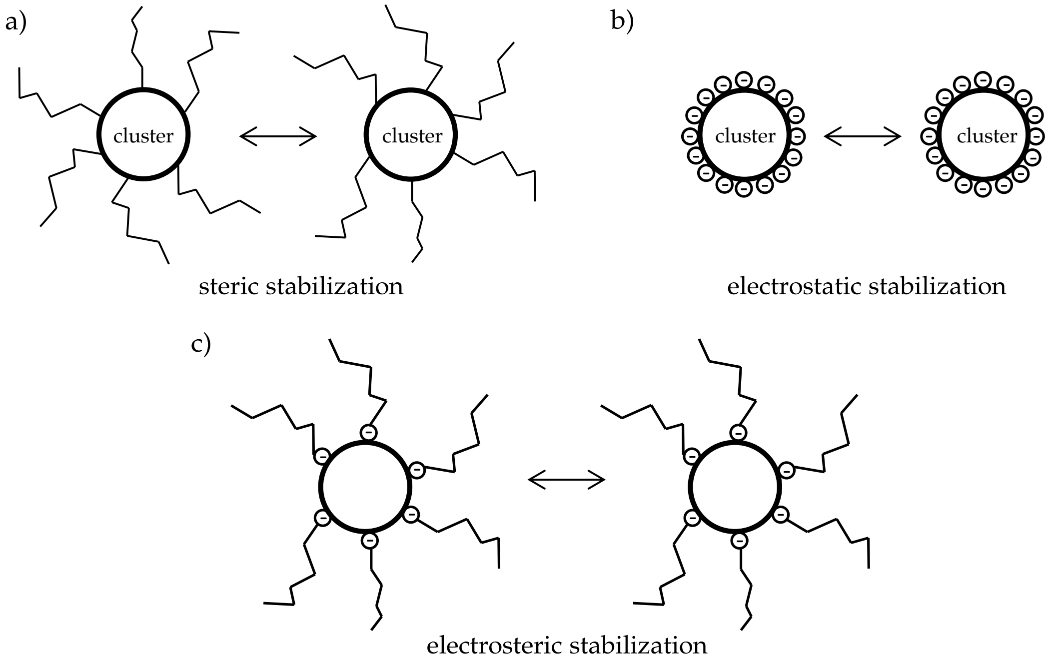

Figure 2.2: Different mechanism of cluster stabilization.

interaction with the active sites of the cluster surface, resulting in a partial deactivation of the surface for catalytic applications [Kra11].

For electrostatic stabilization (figure 2.2b)) the van-der-Waals attraction is counterbalanced by Coulomb repulsion. Ions can form a charged layer around the particles. To retrieve electrical neutrality a second layer consisting of counter ions is formed. Since cations and anions interact differently due to their different chemical nature, the cluster surface will be surrounded predominately with one sort of ions and a shell of counter ions, forming a so-called double layer. The forces between interacting charged surfaces are described in the DLVO theory [Der93; Ver47].

Furthermore, there are compounds that combine both introduced concepts in the so-called electrosteric stabilization (figure 2.2c)). It could be shown that the effectiveness of steric stabilization increases with decreasing particle size, while the effectiveness of electrostatic stabilization decreases with increasing particle size [Mor02].

Ionic liquids are solvents that are used to stabilize nanoparticles electrosterically. The following chapter describes this new class of solvents and motivates the unique possibilities they offer particularly concerning the production of long-term stabilized cluster samples with amounts up to several ppm [Kra11].

2.2 Ionic Liquids

By definition, ionic liquids (ILs) are molten salts, more precisely salts with a melting point below 100 °C, consisting entirely of organic cations (for example pyrolidinium, ammonium or imidazolium) and organic or inorganic anions [Fre10; He15]. Ionic liquids with a melting point below 25° are specified as room temperature ionic liquids. Lately, ILs have developed as a new class of ionic solvents with remarkable properties like negligible vapor pressure, high ionic conductivity and good solubility, which are dominated by the inherently strong, long-range Coulomb interactions among the ions. Due to these properties ILs have proven to be suitable *electrosteric* stabilizers for clusters [He15; Kra11; Jan13].

The large success of ionic liquids in a broad range of applications arises from the fact that their molecular structure of the IL (i.e. the combination of anion and cation) affects the IL properties dramatically. Against the backdrop of seemingly endless combinations of anion and cation, ILs are often referred to as designer solvents [Fre10]. This fact attracted interest in most diverse branches, resulting in applications in analytics, biology, electrochemistry, physical chemistry, engineering, solvents and catalysis [Ple08].

2.2.1 Historical Development

Although the exact discovery date of the first "ionic liquid" is worthy of discussion, the history of ionic liquid chemistry can be traced back to the late nineteenth century, when Friedel and Crafts 1877 described a "red oil" appearing as a separated phase during Friedel-Crafts reactions [Fri77]. This red oil later was found to be consisting of an alkylated aromatic ring cation and a chloroaluminate anion [Nam76], forming the first liquid consisting entirely of ions. The first protic ionic liquid ethanolammonium nitrate with a melting point below 100 °C was discovered by S. Gabriel and J. Weiner in 1888 [Gab88]. The first room temperature ionic liquid (melting point of 12 °C) was synthesized by Paul Walden in 1914 by neutralization of ethylammonium nitrate $[EtNH_3][NO_3]$ with nitric acid [Wal14].

The interest in synthesis and research in those low melting salts (mainly haloaluminate-based ILs) grew subsequently slow because these first generation ionic liquids were not stable in water or air, being of no interest for researchers. The pioneering of Osteryoung and Wilkes in the 1980s lead to the synthesis of the first ionic liquids with anions being stable in water and air in 1992 (imidazolium-based cation with weakly coordinated anions acetate, tetrafluoroborate and nitrate) [Wil92]. Now researchers were not reliant on using glove boxes anymore and in many studies these ILs were used as replacements for ordinary solvents spurring significant research efforts. Ionic liquids began to boom in the early 2000 with third generation task-specific ionic liquids, resulting in a number of exponentially increasing research publications.

The continuous research in ionic liquids already resulted in commercial applications, for example BASF's BASIL^{TM} (Biphasic Acid Scavenging utilizing Ionic Liquids) process, commenced in early 2002 in Ludwigshafen, Germany, which is - up to now - the most successful example of the use of ionic liquids in industrial processes. Often chemical processes produce hydrochloric acid as by-products. Usually these by-products are scavenged by triethylamine. However, in this process (see figure 2.3) ammonium salt is generated, which can lead to unwanted side reactions. In the BASIL process, the triethylamine is replaced by 1-methylimidazole, that reacts with ammonium salt to the ionic liquid 1-methylimidazolium chloride. Both liquids can easily be separated by a phase separator. Further, the reaction rate dramatically increased by a factor of more than 80,000, while the reaction yield also increased from 50% to 98%. Numerous examples for diverse applications can be found in [Ple08].

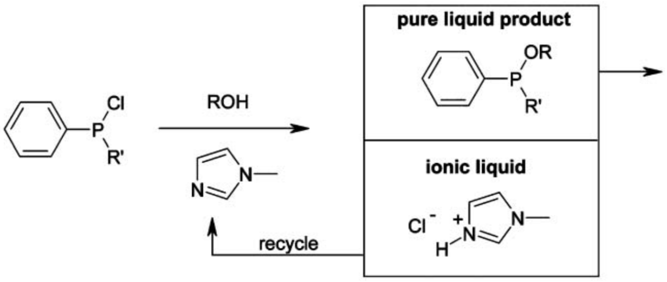

Figure 2.3: BASF's BASIL^{TM} process [Ple08].

2.2.2 Ionic Liquid Nomenclature

As already mentioned, by choosing different anions and cations an almost endless number of ionic liquids is possible. Therefore various notations and nomenclatures for ionic liquids are common in scientific literature. This thesis focuses on imidazolium-based ionic liquids since they are known from literature to be promising candidates for nanoparticle stabilization [Ric11]. The imidazolium cation (1-*alkyl*-3-methyl-imidazolium) is shown in figure 2.4 together with four selected anions: hexafluorophosphate (PF_6), dicyanamide (DCA), bis-(trifluoromethylsulfonyl)imide (Tf_2N) and tetrafluoroborate (BF_4), which will be discussed later on.

The cation is made from a nitrogen-containing organic aromatic ring with linear alkyl side chains. Its name is abbreviated with [C_nMIM]. C_n describes the number of carbon atoms in the linear alkyl chain (methyl=C_1, ethyl=C_2, propyl=C_3, butyl=C_4, pentyl=C_5, hexyl=C_6, heptyl=C_7, octyl=C_8,...) in the rest R_1. The second rest R_2 is always a methyl group (symbol: M). The term IM indicates the imidazolium ring. Occasionally the C_n term is replaced by the abbreviation of the corresponding alkyl. So for example the cation 1-butyl-3-methyl-imidazolium can be referred to as C_4MIM or BMIM.

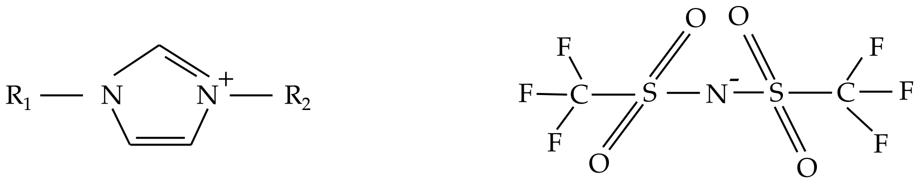

1-alkyl-3-methyl-imidazolium $[C_nMIM]^+$

bis(trifluoromethylsulfonyl)imide $[Tf_2N]^-$

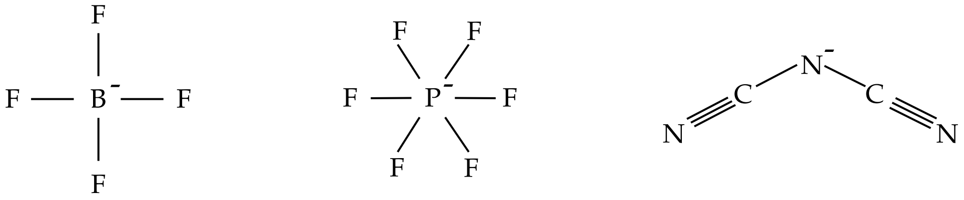

tetrafluoroborate $[BF_4]^-$

hexafluorophosphate $[PF_6]^-$

dicyanamide $[DCA]^-$

Figure 2.4: 1-*alkyl*-3-methyl-imidazolium cation with different anions used in this thesis.

2.2.3 Ionic Liquid Properties

For a long time ionic liquids have been oversimplified by generically claiming that ILs are electrochemically stable, non-flammable, non-volatile, thermally stable and intrinsically "green" [Mac07]. The properties of ionic liquids cannot easily be generalized and compared to common solvents since due to the large number of possible combinations of cations and anions. Some of the most important properties and the dependence on the corresponding IL structure will be discussed hereinafter. A detailed overview of ionic liquids, their properties and applications can be found in [Fre10].

Until 2006 ILs were claimed to have no **vapor pressure**. Therefore ILs are often treated as "green solvents" (although this initial claim is currently being revised [Swa03; Nel02]), resulting in a low risk potential and efficient recycling, making them competitive to common organic solvents and - most important for their use in this thesis - enabling vacuum applications [Kuw10]. Earle *et al.* were the first to distillate an ionic liquid at 600 K and 10^4 bar [Ear06], later the vapor pressure of $[C_1C_4IM][PF_6]$ was determined to 10^{-15} bar at 298 K, in comparison to $3 \cdot 10^{-2}$ bar at 298 K for H_2O [Pau03].

The low **melting point** can be explained by steric effects and asymmetric structures: small cations and anions can be efficiently packed to form crystal structures like NaCl, while ions with different chain lengths suppress symmetry. Further, the combination of the delocalization of the positive charge in the large cation with a weakly coordinated anions results in a weak attractive interaction and thus a repression of crystallization [Lóp07]. For larger anions the melting point of the IL decreases. Also small variations in the alkyl chain or the symmetry of the cation can lead to remarkable differences in the melting point. Examples are given by Freemantle [Fre10].

The **viscosity** of a fluid describes its internal resistance to flow and varies for ILs in a wide range, depending on the chosen anion and cation. Generally ILs have a viscosity that is several magnitudes higher than the one of common solvents. While organic solvents typically have viscosities of about 0.2 up to 10 cP [Rid74] (for comparison: acetone and methanol have viscosities of 0.31 and 0.54 cP, respectively [Nod82]), at room temperature the viscosity of ILs ranges from 10 to 10^5 cP. This can adversely affect applications requiring fast dynamics, but for several purposes (as the stabilization of nanoparticles, see section 5.2) this IL property is very helpful. The viscosity decreases significantly with increasing temperature. By raising the temperature from 25 °C to 80 °C, the viscosity of [C_4MIM][PF_6] is decreased by a factor of ten from 273 mPa to 25.5 mPa [Har05].

2.2.4 Used Ionic Liquids

Most experiments in this thesis have been performed with the ionic liquid C_4MIM PF_6. C_4MIM PF_6 is together with C_4MIM BF_4 the most investigated ionic liquid since they have been the first ionic liquids being stable in air [Wil92]. Former studies by Richter and Vanecht [Ric11; Van12] have shown that 1-butyl-3-methyl-imidazolium ionic liquids with weakly coordinating ions can be suitable stabilizers for metal nanoparticles.

In order to study the influence of different anion and cation combinations, experiments with other ionic liquids selected to certain criteria according to the study of Richter [Ric11] have been performed. The cation alkyl-side chain length is varied as well as the anion donor strength. The results will be presented in section 5.3. Table 2.1 gives an overview of the ionic liquids used in the experiments (see also figure 2.4) in this thesis, including their CAS numbers and selected, relevant properties.

name (short form)	CAS no.	viscosity η [Pa·s]	refractive index n_D
C_4MIM Pf_6	174501-64-5	$0.354^{(1)}$	1.4115
C_4MIM Bf_4	174501-65-6	$0.095^{(1)}$	1.4200
C_4MIM Tf_2N	174899-83-3	$0.056^{(1)}$	1.4288
C_4MIM DCA	448245-52-1	$0.032^{(1)}$	1.5085
C_8MIM Pf_6	304680-36-2	$0.603^{(2)}$	1.4232

Table 2.1: Ionic liquids used in this thesis. Important properties like viscosity at room temperature and refractive index are also given.
$^{(1)}$ [Van11], $^{(2)}$ [AlT14]

Since the refractive index of an ionic liquid directly affects the cluster plasmon resonance position (cf. section 4.3.3), it has been determined for all used ionic liquids using an Abbe type refractometer [Ins]. The measuring principle is based on the fact that the critical angle α_c of the total reflection depends on the refractive indices of the involved media. The total reflection is measured between a glass prism with a high refractive index n_{p} and the ionic liquid having a smaller refractive index n_{IL}. Since the refractive index of the prism is known, n_{IL} can be determined via

$$n_{\mathrm{IL}} = n_{\mathrm{p}} \cdot \sin \alpha_c. \tag{2.1}$$

Usually those measurements are performed using light with the wavelength of the sodium D-line (589 nm). Since the refractive index depends on the wavelength of the incident light, also the Abbe number V_D is determined, which describes the material dispersion: $V_D = \frac{n_D - 1}{n_F - n_C}$. n_D, n_F and n_C are the refractive indices of the Fraunhofer D-, F- and C-lines. This linear approximation of the dispersion (solid lines) and the linear extrapolation (dashed lines) are shown in figure 2.5. The measurements of the refractive indices have been performed in the framework of F. Lippert's master thesis [Lip17].

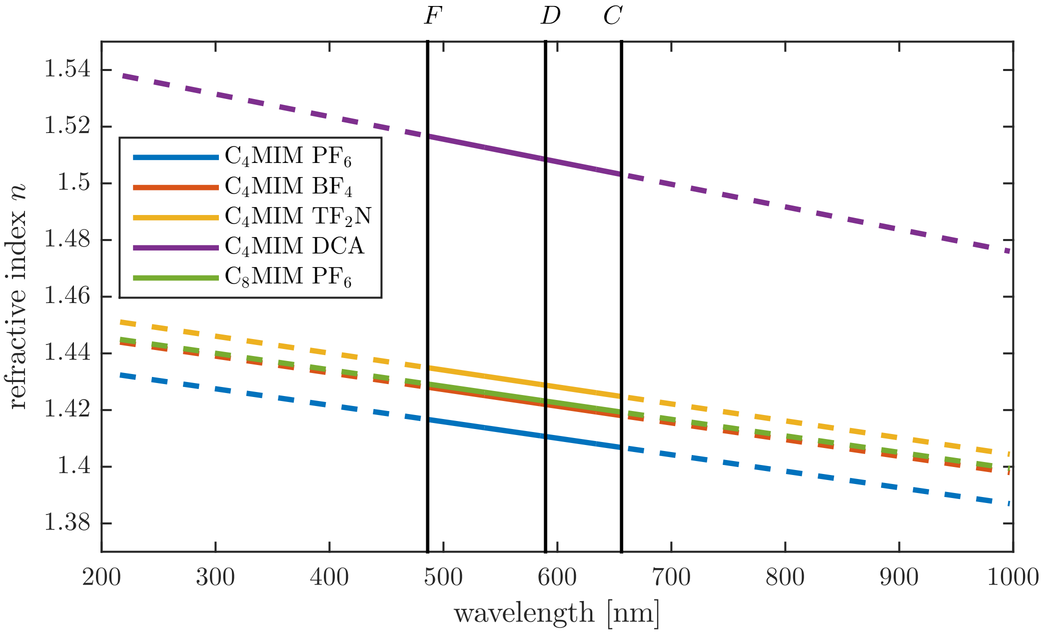

Figure 2.5: Based on the measurement of n_D at 589 nm and the corresponding Abbe number $V_D = \frac{n_D - 1}{n_F - n_C}$ a linear approximation is used to calculate the refractive index for the different investigated ionic liquids for wavelengths in the UV/Vis range.

Further, there is a trend towards higher viscosity for increasing length n of the alkyl-side chain C_nMIM from n=2 to n=8. For n=4 the anions follow the viscosity order PF_6 > BF_4 > Tf_2N > DCA. This is in accordance with the anion donor strength and shows that the anion-cation interaction plays a significant role on IL viscosity [Hol08]. A high viscosity corresponds to a low refractive index.

2.3 Preparation Concepts for Ionic Liquid Stabilized Metal Clusters

As discussed in the previous sections, both clusters and ionic liquids are highly topical and offer a broad field of applications; thus a combination of these two topics is obvious. Two examples for applications of metal nanoparticles in ionic liquids are the possibility of re-using nanoparticles in catalysis [Fon04; Des01; Dup02] and for biosensors [Fer09]. Consisting exclusively of anions and cations, ionic liquids enable remarkably strong electrostatic stabilization due to their high ion density, while concurrently anion and cation can be chosen in a way that either cation or anion adsorbs strongly on the cluster surface while the counter ion provides a bulky steric structure. Furthermore the thermal movement of the clusters stabilized in an IL is suppressed due its high viscosity because of the reduced self diffusion coefficient of approximately 10^{-12} to $10^{-11}\,\mathrm{m^2s^{-1}}$ [Kow08] compared to the self diffusion coefficient of common solvents ($10^{-9}\,\mathrm{m^2s^{-1}}$ [Sla07]) with viscosities comparable to water.

Ionic liquids are not only suitable for nanoparticle stabilization, but represent also a medium for the synthesis of nanoparticles. In many cases metal nanoparticles are synthesized by chemical reduction of metal salts, where the metal atom is in a positive oxidation state. Reducing agents as gases (H_2) or organic (e.g. citrate, ascorbic acid) and inorganic (e.g. $NaBH_4$) agents are used to generate neutral metal atoms. In the absence of stabilizers those atoms agglomerate to microscopic crystals. Also thermal decomposition of organometallic compounds results in the formation of metal nanoparticles stably dispersed in ILs. Dupont *et al.* were the first who successfully synthesized nanoparticles in an IL, namely iridium in C_4MIM PF_6 [Dup02]. However, during synthesis by-products and impurities can enter the IL, possibly influencing the nanoparticle stability significantly [Das09].

Due to the negligible vapor pressure a new technological concept was introduced: the application of liquids in vacuum technologies. Torimoto *et al.* presented the synthesis of gold onto ionic liquids by sputter deposition [Tor06]. Argon atoms are bombarding a gold target ejecting gold atoms, that are deposited onto the surface of an IL film surface. Different particle sizes depending on the kind of IL were found. Alternative methods for nanoparticle preparation in ILs are the plasma reduction method [Abe07] and the physical vapor deposition technique [Ric10]. Here the metal is evaporated at high temperature and condensed onto the ionic liquid. An extensive review on different production techniques has recently been given by Dupont and Scholten [Dup10]. The samples were stable and also highly disperse in contrast to common synthesis methods without additional stabilizing agents.

However, the stability of nanoparticles in ionic liquids is controversially discussed. While some groups report the stability of their samples on timescales of several weeks [Van12; Gao15; Uen08], other groups observe immediate aggregation [Red08; Sch07; Ito04], depending on the selected ionic liquid. Richter *et al.* [Ric11] found increased stability using weak coordinating and fluorinated anions. The most stable colloid was found using C_4MIM PF_6.

Moreover, different kinds of stabilization mechanisms for metal clusters in ionic liquids are discussed in terms of which compound of the IL mainly contributes to cluster stabilization: the imidazolium rings of the cations, the alkyl chains of the cation or the anions are reported to be responsible for cluster stabilization. A discussion of different experimental results should be handled with care since different systems using different cluster material and different cluster sizes as well as size distributions. However, the experimental results are controversially discussed in literature and only a few examples are given here.

^{2}H NMR experiments reveal that C_4MIM cations form an N-heterocyclic carbine on the surface of 2 nm Ir clusters independent on the choice of anion [Ott05]. These results have been confirmed for C_4MIM BF_4 stabilized 6 nm Ag clusters in surface enhanced Raman scattering measurements [Rub08]. Size dependent molecular dynamics simulation of Au clusters in C_4MIM BF_4 revealed the alkyl chains are responsible for the stabilization of small clusters, while the imidazolium rings dominate the interaction with large clusters [Fu17]. In contrast, Khare *et al.* have observed a strong dependence of cluster growth and stability on the chosen anion of C_2MIM base ILs using transmission electron microscopy and X-ray diffraction [Kha10b]. Their results are supported by experiments performed by Redel *et al.* [Red08] in size-dependent measurements with Ag clusters.

All these presented preparation methods have in common that the resulting particle size can hardly be controlled. For example, in sputtering depositions the particle size depends on sputtering parameters like current, voltage and gas pressure as well as on the time passed after production since the particle growth within the liquid is known to take place several minutes up to hours. Also the combination of anion and cation can have significant influence on the particle size. These dependencies complicate the discussion concerning timescales of stability and stabilizing mechanisms, which becomes obvious in the enormous amount of contradictory literature. Often it is not possible to distinguish between the end of the particle growth process and the starting point of aggregation. Moreover, size and size distribution of the particles are highly dependent on small variations of the physiochemical properties of the IL.

This thesis aims to shed new light into the intensely discussed topic of nanoparticle stabilization in ionic liquids. A new approach of sample preparation is introduced. In order to avoid the above mentioned problems of uncontrolled particle sizes the clusters are preformed with known diameter and narrow size distribution in the cluster source and are deposited into the ionic liquid with well-known properties afterwards (for details see section 3). Therefore every measured change in the sample can be assigned to aggregation. Most experiments in this thesis have been performed using C_4MIM PF_6. The first results for other imidazolium based ionic liquids are discussed in section 5.3.

Chapter 3

Sample Production

There are several methods introduced in literature describing technical possibilities for cluster production. The silver clusters investigated in this thesis are produced in a supersonic expansion with THECLA [Höv93], a thermal cluster apparatus described in detail in section 3.2.

The initial idea for choosing this type of cluster source was to produce a highly intense and focused cluster beam to investigate the optical properties of free Ag clusters and how they change after deposition into different matrix materials [Höv95]. Alternative methods like the cluster production in a gas aggregation source [Fra85] or a magnetron sputtering source [Hab91] have not been suitable for these experiments due to the too low cluster flux. In THECLA the cluster material is vaporized in a graphite oven by a tantalum heater into a streaming inert carrier gas. The noble gas-stream-mixture is expanded through a supersonic nozzle into a region with less pressure and cluster growth takes place.

To prepare the ionic liquid samples with macroscopic amount of clusters (up to several ppm) used in this thesis it is made use of THECLA's potential to produce a high cluster deposition rate up to 9 nm/s [Höv95]. A high amount is required for a sufficient signal to noise ratio in X-ray absorption experiments (see chapter 7). The gas dynamics and cluster condensation in THECLA is described in this chapter, followed by the description of the deposition of the preformed silver clusters in ionic liquids.

3.1 Gas Dynamics in a Supersonic Expansion

The following description of a supersonic expansion is based on [Höv95]. If a gas is expanded from a region with high pressure into a region of low pressure through a nozzle, there are two limiting cases for gas molecule acceleration (see figure 3.1). The so-called Knudsen number *Kn* is defined as the ratio of the molecular mean free path length $\overline{\lambda}$ and the diameter d of the nozzle:

$$Kn = \frac{\overline{\lambda}}{d} \tag{3.1}$$

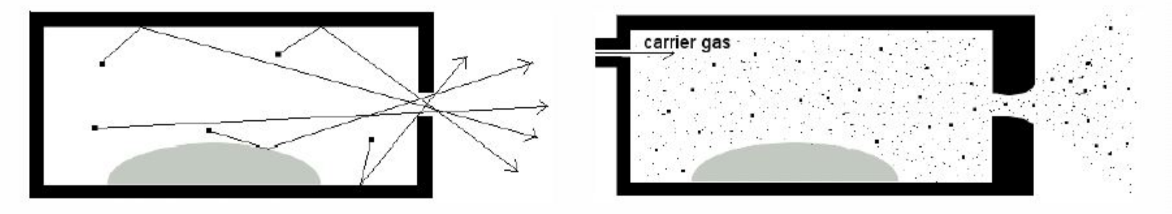

Figure 3.1: Expansion through a nozzle for two limiting cases. Left: Molecular flow, $Kn \gg 1$, right: Supersonic flow, $Kn \ll 1$ [Hof12].

If $Kn \gg 1$, the particles pass the nozzle with almost no collisions (molecular flow). Their velocity and direction can be described by a Maxwell distribution. In the other limiting case, for an increased vapor pressure, the mean free path decreases ($Kn \ll 1$) and the particles collide with each other. This process can be described by a gas dynamic continuum. During expansion into a vacuum, the beam is adiabatically cooled and intensely directed along the beam axis. The particles are accelerated up to supersonic speed, which results in a supersaturation of metal molecules leading to cluster growth. The addition of argon as a carrier gas is not mandatory for cluster growth, however, without any additional gas the cluster beam would consist of liquid clusters with a temperature $T > T_{\text{melting}}$ [Gsp86], because the clusters absorb the condensation heat in each growth step. The carrier gas cools down the beam by interaction of gas and clusters. However, the carrier gas needs to be removed after cluster condensation to obtain a beam consisting of almost exclusively clusters for further investigations.

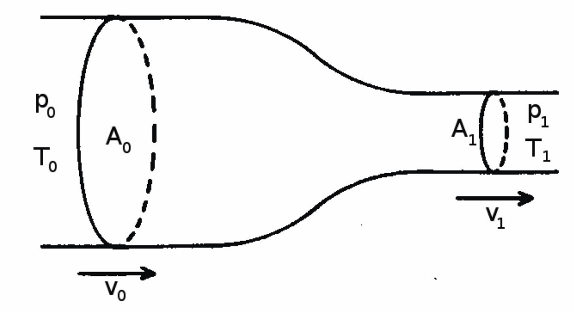

Figure 3.2: Flow tube with slowly changing cross section [Höv95].

The phenomenon of a supersonic expansion can be described by gas continuum dynamics for an ideal gas with temperature T, pressure p, cross section A, velocity v and specific heat c_p flowing through a tube with slowly changing cross section as illustrated in figure 3.2. The expansion of this gas from the initial state into the final state (denoted with indices 0 and 1) is adiabatic, hence energy and mass are conserved. Taking conservation of energy and mass into account, for an ideal gas with $pV = nRT$ (n: amount of substance and R: ideal gas constant) this leads to

$$\left(\frac{1}{2}\rho_0 v_0^2 + \rho_1 c_p T_0\right) A_0 v_0 = \left(\frac{1}{2}\rho_1 v_1^2 + \rho_1 c_p T_1\right) A_1 v_1 \tag{3.2}$$

and

$$\rho_0 A_0 v_0 = \rho_1 A_1 v_1. \tag{3.3}$$

Here c_p denotes the specific heat capacity. Assuming $v_0 = 0$ at $T = T_0$, equations (3.2) and (3.3) yield

$$c_p T_0 = \frac{1}{2} v_1^2 + c_p T_1. \tag{3.4}$$

The local speed of sound is defined as $a = \sqrt{\frac{\gamma \cdot k_\mathrm{B} \cdot T}{m}}$. Here the abbreviation $\gamma = \frac{c_p}{c_V}$ is used, k_B is the Boltzmann constant and m the mass of a gas molecule. Then c_p can be written as

$$c_p = \frac{\gamma}{\gamma - 1} \cdot \frac{k}{m}. \tag{3.5}$$

By introducing the Mach number $M = v/a$ as the ratio of flow velocity to the local speed of sound equation, equation (3.4) holds

$$\frac{T}{T_0} = \left(1 + \frac{1}{2}(\gamma - 1)M^2\right)^{-1}. \tag{3.6}$$

Based on the adiabatic character of this process, the other parameters can be rewritten using Poisson's equation

$$\left(\frac{p}{p_0}\right) = \left(\frac{V_0}{V}\right)^{\gamma} = \left(\frac{T}{T_0}\right)^{\gamma/(\gamma-1)} = \left(\frac{\rho}{\rho_0}\right)^{\gamma} \tag{3.7}$$

to get expressions for the local pressure and density along the beam axis:

$$\frac{p_1}{p_0} = \left(\frac{T_1}{T_0}\right)^{\gamma/(\gamma-1)} = \left(1 + \frac{1}{2}(\gamma - 1)M^2\right)^{-\gamma/(\gamma-1)} \tag{3.8}$$

$$\frac{\rho_1}{\rho_0} = \left(\frac{T_1}{T_0}\right)^{1/(\gamma-1)} = \left(1 + \frac{1}{2}(\gamma - 1)M^2\right)^{-1/(\gamma-1)} \tag{3.9}$$

With increasing adiabatic cooling the Mach number increases along the beam axis to values $M \gg 1$. Thus this kind of expansion is called a supersonic expansion. The velocity in the nozzle can be written as a function of the Mach number

$$v = M \cdot a = M \cdot a_0 \left(\frac{T}{T_0}\right)^{1/2} = M \cdot a_0 \cdot \left(1 + \frac{1}{2} \cdot (\gamma - 1) \cdot M^2\right)^{-\frac{1}{2}} \tag{3.10}$$

with $a_0 = \sqrt{\gamma \frac{k_\mathrm{B} T_0}{m}}$.

The limit of the flow velocity (with $\gamma = 5/3$) is

$$v_\infty = \lim_{M\to\infty} v = a_0\sqrt{\frac{2}{\gamma-1}} \approx 2.24 \cdot \sqrt{T_0 \cdot \frac{k_B}{m}}. \tag{3.11}$$

With this a Mach number can be found at which the partial pressure in the nozzle at given temperature is higher than the saturated vapor pressure. This is the state in which cluster condensation can take place. Hövel [Höv95] calculated some parameters for the used source at $M = 1$: $T = 1725\,\mathrm{K}$, $p_\mathrm{p} = 208\,\mathrm{mbar}$ and p_V=4.5 mbar.

In conclusion, in THECLA's cluster source vaporized silver and argon as a carrier gas are expanded through a supersonic nozzle. As the ordered motion of the particles increases, temperature, density and pressure decrease and cluster aggregation can take place. Here a nozzle with an opening angle of $2\alpha = 10°$, a diameter of $d = 0.42\,\mathrm{nm}$ and a length of $L = 25\,\mathrm{mm}$ produces a strongly aligned cluster beam with a velocity of $v = 1500\,\mathrm{m/s}$, which corresponds to a kinetic energy of $400\,\mathrm{eV/cluster}$. The size distribution of the produced clusters was determined in transmission electron microscopy (TEM) measurements. As a result the volume-averaged cluster

$$\overline{R} = \left(\frac{\sum n_i R_i^3}{\sum n_i}\right)^{1/3} = (2 \pm 0.6)\,\mathrm{nm} \tag{3.12}$$

was obtained [Höv95; Hil01b], which corresponds to $(2.5^{+2.8}_{-1.7} \cdot 10^2)$ atoms per cluster.

3.2 Thermal Cluster Apparatus

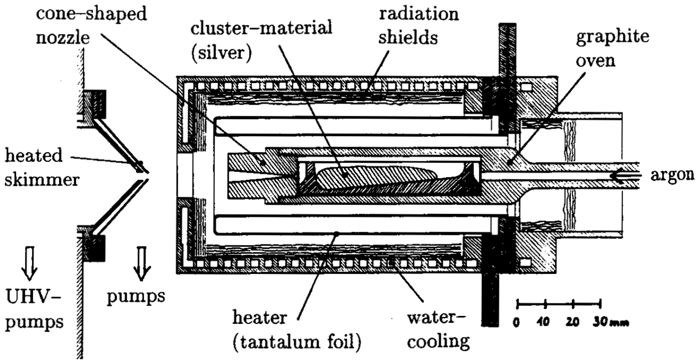

Figure 3.3: Cross section of THECLAS's cluster source [Höv95]. Ultra pure silver (99.99% silver powder purchased from ChemPUR, Karlsruhe, Germany) is located in the middle of the graphite oven with an argon inlet on the one side and a supersonic nozzle on the other side. Around that a water-cooled tantalum heater is mounted, which can be heated up to 2300 K in order to vaporize the silver.

Figure 3.3 shows an illustration of the cluster source. Here the silver powder is heated up in a graphite oven enclosed in a tantalum heater with an electric power of 2 kW, reaching temperatures up to 2300 K and a saturated vapor pressure of 400 mbar. Pressurized argon

(4500 mbar) is used as carrier gas. This heated gas mixture is expanded through a nozzle into the vacuum. A large percentage of the argon is already pumped out in the source chamber. The outer, diffuse part of the cluster beam is cut out by a heated aperture, the so called skimmer made of tantalum and operated at 2300 K to prevent a closing of the aperture due to aggregated silver.

An overview of THECLA is given in figure 3.4. After cluster condensation the residual carrier gas needs to be removed to obtain an undisturbed cluster beam by freezing it out in the double-stage cryogenic pumping stage that is connected to the skimmer by Teflon isolation.

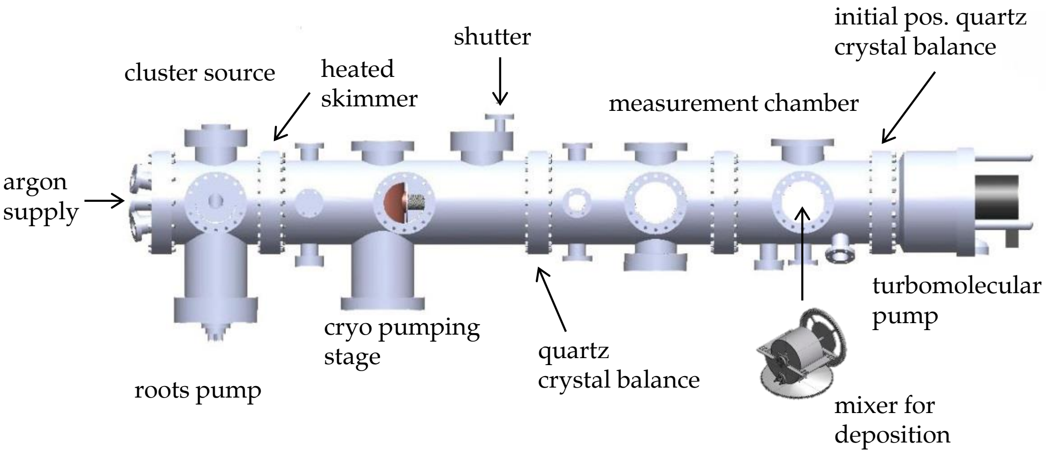

Figure 3.4: Overview of the thermal cluster apparatus THECLA [Hen09]. Silver clusters are produced in the cluster source in a supersonic expansion and are deposited into an ionic liquid using a mixer described in section 3.3.

In principle cluster deposition in THECLA is possible at two sample positions. The first one is equipped with a manipulator that enables the cluster deposition on solid sample surfaces or into matrices like PDMS [Roe16]. This thesis focuses on the cluster deposition into liquids, which is performed at the second sample position. The current cluster deposition rate is determined using a quartz crystal micro balance, which is in detail described in section 3.3. If necessary, the cluster beam can be interrupted by a rotatable shutter. The turbomolecular pump (pumping speed 1000 l/s) at the end of the vacuum chamber combined with the roots pump (pumping speed 70 l/s) and the cryogenic pumping stage produces a final residual pressure of ~10^{-8} mbar in the measuring chamber. The rare gas pressure (argon) during cluster beam operation is $1 \cdot 10^{-5}$ mbar.

3.3 Cluster Deposition

To realize a homogenous mixture of the clusters and the ionic liquid a custom-built stainless steel mixer was used (designed by [Eng14] and modified in the framework of this thesis). It is shown in figure 3.5a). 15 ml of an ionic liquid is filled into the tub. A rotating roller is used to stir the IL so that the upper part of the roller is always moistened with a thin film of ionic liquid. The roller is placed perpendicular to the cluster beam. To save weight, the roller is hollow inside with four holes for a fast evacuation. The clusters are hitting the IL film and are immediately mixed into the volume to prevent aggregation. The mixer is driven by two gearwheels made of aluminum, the lower one is powered by a step motor from outside the vacuum chamber. The step motor operates with rotation frequencies between 0.1 and 1.3 Hz. At each head of the tub a fused silica window is mounted, enabling *in-situ* UV/Vis measurements during cluster deposition. This method is used to pre-characterize the amount and shape of the deposited clusters (see chapter 5 for details). The optical path length in the tub is 6 cm.

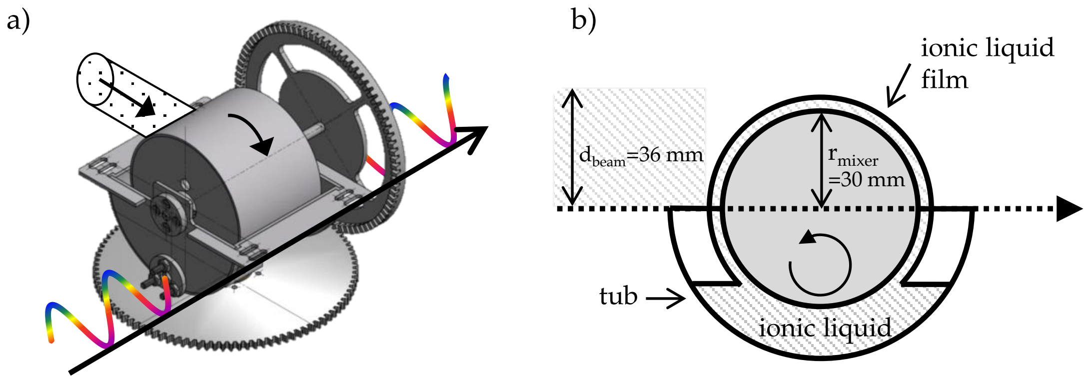

Figure 3.5: a) Mixer used for cluster deposition in ionic liquids. The tub contains a volume of 15 ml ionic liquid and is equipped with two fused silica windows for *in-situ* UV/Vis measurements as indicated by the wave traveling through the tub. b) Sketch of cluster deposition onto the IL film, which is mixed in the IL reservoir by rotation (figure not drawn to scale).

The quartz crystal micro balance needs to be moved out of the beam during cluster deposition. For checking purposes of the current cluster deposition rate it can be moved back into the beam at every time during deposition.

During the first experiments a crystal balance right in front of the turbo molecular pump was used. During deposition the mixer was moved into the cluster beam, covering the surface of the crystal balance. Therefore, a check of the cluster deposition rate during deposition was not possible without moving the mixer down again. To move the mixer, the connection between mixer and step motor was realized with gearwheels coupled with a magnetic rod manipulator. The disadvantage of this procedure was that the optical adjustment is very error-prone since mechanical drifts can occur. Although the optical adjustment could be done at the correct height before the deposition started, it had to be corrected after moving the mixer back into the beam axis, which sometimes led to small discrepancies.

To remedy this problem the mixer was mounted rigidly at a rotary feedthrough, fixing the mixer to the beam axis. To measure the current cluster deposition rate a second crystal balance was installed at the marked position that can be moved into the beam with a transfer rod during deposition to control the current cluster deposition rate. Due to the modified position, the beam diameter, which varies along the length of THECLA, needs to be taken into account while calculating the total deposition amount for comparison with earlier experiments.

Within the scope of Z. Batsoev's bachelor thesis [Bat14] the operating parameters of the mixer were optimized with regard to an ideal mixing. The mixing process was visualized with five stripes of ink, that were evenly distributed across the entire width of the roller. By observing the mixture of the IL with the ink the mixing process was evaluated. Besides an optimal rotation frequency of $1\,\mathrm{Hz}$ those measurements revealed that the insertion of a barrier made from stainless steel wire at the bottom of the tub against the direction of rotation as a flow resistance significantly improves the mixing inside the tub.

Remaining water may have a large impact on the physical and chemical properties of an ionic liquid [Van12; Sed00]. To degas these water impurities the IL is dried for 24 hours at $340\,\mathrm{K}$ under a vacuum of about 10^{-3} mbar in a vacuum furnace. Following this process, the IL has a water content less than $20\,\mathrm{ppm}$ [Hat10]. Another problem occurring, if the IL has not been degassed before filling it into the tub is, that the remaining water evaporates at pressures of several mbar and a significant amount of IL is spurted out of the tub. Quadrupole mass spectra reveal, that most impurities can be assigned to water incorporations [Eng14], which can be removed by degassing the IL and storing it in the rotating mixer under vacuum conditions for several hours in order to reduce the partial pressure in the measurement chamber. The above described procedure was carried out for all cluster depositions.

3.4 Calculation of Deposited Cluster Material

Following the dimensions given in figure 3.5b) the total amount of deposited silver can be calculated. In THECLA cluster beam and roller are axial to each other. The beam has a diameter of $36\,\mathrm{mm}$ and the diameter of the roller is $60\,\mathrm{mm}$. Thus the upper half of the roller is completely covered with the cluster beam. Therefore the effective deposition area is $A_{\mathrm{Ag}} = \pi R^2 = \pi 15^2\,\mathrm{mm}^2 = 706\,\mathrm{mm}^2$. From the deposition rate x_{depo} and the deposition time t_{depo} a total deposition amount of $h_{\mathrm{eff}} = x_{\mathrm{depo}} \cdot t_{\mathrm{depo}}$ results. From these data the volume of the deposited clusters $V_{\mathrm{Ag}} = A_{\mathrm{Ag}} \cdot h_{\mathrm{eff}}$ and finally the mass m_{Ag} with $\rho_{\mathrm{Ag}} = 10.49\,\mathrm{g/cm^3}$ can be calculated:

$$m_{\mathrm{Ag}} = \rho_{\mathrm{Ag}} \cdot A_{\mathrm{Ag}} \cdot x_{\mathrm{depo}} \cdot t_{\mathrm{depo}} \tag{3.13}$$

Chapter 4

Theory: Interaction of Small Silver Clusters with Light

The following sections introduce briefly the basics needed to understand the optical properties of silver nanoparticles: classical electrodynamics in matter and solid state theory.

Maxwell's equations (section 4.1) explain the behavior of electromagnetic fields in both vacuum and matter. However, material parameters like the dielectric function ϵ are used as input parameters to Maxwell's equations and cannot be explained by them. These parameters must either be taken from experimental data or be calculated with solid state theory.

As described in section 4.2 for small silver clusters the optical absorption differs significantly from a bulk silver film due to the limited size and thus the influence of the cluster surface. Using Mie's theory [Mie08] the response of a metal cluster to an external electromagnetic field, the so-called cluster plasmon resonance, can be calculated.

The influence of size, shape and embedding medium on the particle plasmon resonance is discussed in section 4.3, followed by a brief description of the Generalized Mie theory, which describes the interaction of aggregated nanoparticles with light.

At the end of this chapter in section 4.4 the experimental setup for the UV/Vis absorption spectroscopy *in-situ* (during cluster deposition) and *ex-situ* (after removing the sample from the UHV chamber) is presented.

4.1 Maxwell's Equations in Matter

Maxwell's equations are the fundamental laws to classical electrodynamics, explaining the behavior of electromagnetic fields in both vacuum and matter. External electric fields can cause a shift of the charges inside a neutral atom, leading to a polarization of the atom. The induced dipole moment $\vec{p}$ is proportional to the electric field: $\vec{p} = \alpha \cdot \vec{E}$. A measure for polarization in condensed matter is the polarization vector

$$\vec{P} = \chi_{\mathrm{el}} \epsilon_0 \vec{E}. \tag{4.1}$$

Here ϵ_0 is the permeability of the free space and χ_{el} denotes the electric susceptibility, a material dependent constant. With the dielectric function $\epsilon = 1 + \chi$ (also known as relative permittivity ϵ_r) the dielectric displacement is defined:

$$\vec{D} = \epsilon_0 \vec{E} + \vec{P} = \epsilon_0 \vec{E} + \chi_{\text{el}} \epsilon_0 \vec{E} = \epsilon_r \epsilon_0 \vec{E} \tag{4.2}$$

Analogously, for the magnetizability M of materials with a permeability $\mu = 1 + \chi_{\text{mag}}$ in a magnetic field B we define:

$$\vec{H} = \frac{1}{\mu_0} \vec{B} + \vec{M} = \frac{\vec{B}}{\mu_0 \mu} = \frac{\vec{B}}{\mu_0 (1 + \chi_{\text{mag}})} \tag{4.3}$$

The above defined fields $\vec{D}$ and $\vec{H}$ also satisfy Maxwell's equations and we obtain:

$$\nabla \cdot \vec{D} = \rho_{\text{f}} \qquad \text{Gauss's Law} \tag{4.4}$$

$$\nabla \times \vec{E} = -\frac{\partial \vec{B}}{\partial t} \qquad \text{Magnetic Analogon} \tag{4.5}$$

$$\nabla \cdot \vec{B} = 0 \qquad \text{Ampére's Circuital Law} \tag{4.6}$$

$$\nabla \times \vec{H} = \vec{J}_{\text{f}} + \frac{\partial}{\partial t} \vec{D} \qquad \text{Faraday's Induction Law} \tag{4.7}$$

The free charge density ρ_{f} and the electric current J_{f} are the sources of the fields. ϵ_0 and μ_0 stand for the permeability and permittivity of the free space. In absence of matter, χ_{el} and χ_{mag} are zero, and we receive Maxwell's equations in vacuum. For the systems considered in this thesis, magnetic effects are not considered since $\mu_{\text{silver}} \approx 1$.

To solve Maxwell's equations in matter, the knowledge of the dielectric function is essential. In general a dielectric function is frequency-dependent and has a real and an imaginary part: $\epsilon = \epsilon_1 + i\epsilon_2$. Real and imaginary part describe the polarization charge density and the optical loss in the material, respectively. Different processes contribute to the dielectric function at different time scales. Oscillating incident fields distort the positions of the electrons and/or the atoms in the crystal lattice and induce dipoles, acting as resetting forces. These harmonic oscillations are described in the following chapters for different contributions.

4.2 Size Dependent Dielectric Function of Silver

4.2.1 Lorentz Oscillator

As a first approach to the dielectric function we consider the Lorentz model, which treats the electrons in each atom like masses on a spring. By applying an external field the electrons move while the nucleus is kept fixed due to its higher mass ($m_p/m_e = 1836$). Thus the electrons can be treated by the classical motion equation as bound electrons excited by an external force analogously to the driven harmonic oscillator:

$$m\frac{d^2\vec{x}}{dt^2} = -m\omega_0\vec{x} + e\vec{E} - m\gamma\frac{d\vec{x}}{dt} \tag{4.8}$$

Here m denotes the electron mass, ω_0 the eigenfrequency of electron oscillations, e the elementary charge, $\vec{E} = \vec{E}_0 e^{-i\omega t}$ the applied time-harmonic electric field with angular frequency ω and γ the damping constant. This differential equation (4.8) is solved by

$$\vec{x}(t) = \frac{e}{m}\frac{1}{\omega_0^2 - \omega^2 - i\gamma\omega}\vec{E}_0 e^{-i\omega t}. \tag{4.9}$$

Assuming a number of oscillators N per unit volume and a dipole $\vec{p} = e\vec{x}$ yields a polarization $\vec{P} = N\vec{p} = Ne\vec{x}$. By inserting equation (4.9) and using equation (4.1) the dielectric function of the Lorentz model can now be defined as

$$\epsilon^{\text{Lorentz}}(\omega) = 1 + \frac{\omega_p^2}{(\omega_0^2 - \omega^2) - i\gamma\omega}. \tag{4.10}$$

Here $\omega_p = e\frac{N}{\epsilon_0 m}$ is the plasma frequency, indicating the point where $\epsilon_1 \approx 0$ in a system with $\omega_0 = 0$ (the dielectric function only depends on free electrons). The real and imaginary part of equation (4.10) are shown in figure 4.1. Analogous to the driven harmonic oscillator there are three cases for electron motion dependent on the frequency ω of the applied field.

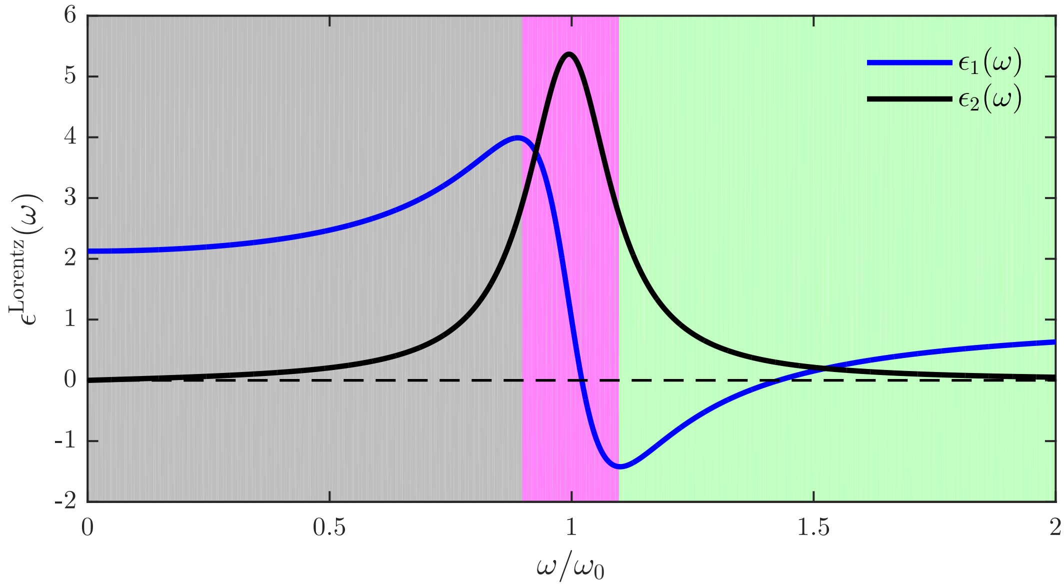

Figure 4.1: Both real and imaginary part of the dielectric function $\epsilon^{\text{Lorentz}}(\omega) = \epsilon_1(\omega) + i\epsilon_2(\omega)$ as a function of ω_0 are shown. See text for discussion of the three cases concerning resonance dependency of the Lorentz oscillator.

For low frequencies (gray area) the electrons move in phase with the applied field. Far away from the resonance frequency ϵ_1 can be considered to be constant. At a certain frequency, the so called resonance frequency, the denominator of equation (4.9) is minimized, leading to a resonance at $\omega = \omega_0$ for small damping constants γ (pink area). The magnitude of the electron oscillations increases (pink area) because in each cycle the driving force gives energy to the system. If there was no damping ($\gamma = 0$), the energy would become infinite. In case of damping, the energy is built up to the point where it is equaled by the dissipation of the losses resulting from damping. This region has a high absorption (high value for ϵ_2). In the third case, above the resonance frequency the dielectric function tends towards the one of vacuum ($\epsilon_1 = 1$, $\epsilon_2 = 0$) because there is no response to the driving field anymore as shown in the green area.

4.2.2 Drude-Sommerfeld Model

In comparison to the bound electrons described by the Lorentz model, electrons in metals near the Fermi level can easily be excited into other states by photons with small energies. Thus, they can be treated as free electrons without any resetting force from the ions. The electrons are moving independently and can collide with an average rate of $\gamma_0 = \tau^{-1}$, where τ describes the electron relaxation time. After every collision the orientation of the electrons is random. To obtain the optical response of a collection of free electrons, which is referred to as the Drude model [Dru00], the resetting force in the Lorentz oscillator (equation (4.8)) is removed:

$$m\frac{d^2x}{dt^2} = eE - m\gamma\frac{dx}{dt} \tag{4.11}$$

The solution (analogous to section 4.2.1) leads to the dielectric function

$$\epsilon^{\text{Drude}}(\omega) = 1 - \frac{\omega_p^2}{\omega(\omega + i\gamma_0)} \approx 1 - \frac{\omega_p^2}{\omega^2} + i\frac{\gamma_0\omega_p^2}{\omega^3}. \tag{4.12}$$

Here $\omega_p = \sqrt{Ne^2/\epsilon_0 m^*}$ is the so-called plasma frequency with N and m^* describing density and effective mass of the conduction electrons. Figure 4.2 shows the frequency dependence of $\epsilon^{\text{Drude}}(\omega)$.

Figure 4.2 distinguishes between two frequency regions. For $\omega > \omega_p$ ϵ^{Drude} is positive (green area) and the corresponding refractive index $n = \sqrt{\epsilon^{\text{Drude}}}$ is a real quantity, whereas n becomes imaginary for $\omega < \omega_p$ (pink area), which entails that electromagnetic waves cannot propagate inside the medium.

For most metals ω_p is in the ultraviolet region, which is why they are shiny in the visible spectrum: the electrons in the metal screen the light ($\omega < \omega_p$) from the metal.

In contrast to figure 4.1 there is no region below the resonance frequency, corresponding to $\omega_0 \rightarrow 0$. Due to the missing resetting forces the maximum energy from the driving field is transferred to the electrons for a static field ($\omega = 0$) by simply accelerating the electrons in

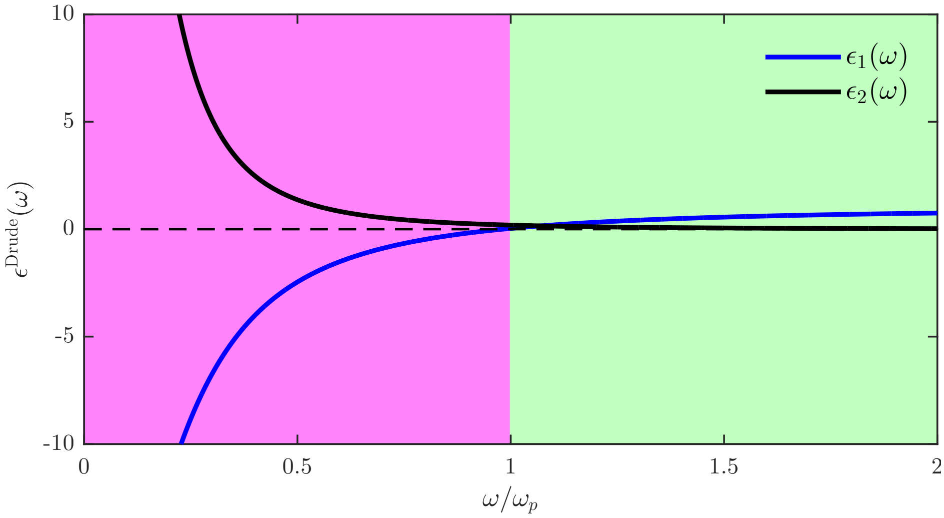

Figure 4.2: $\epsilon^{\mathrm{Drude}}(\omega) = \epsilon_1 + i\epsilon_2$ of a Drude metal as a function of the plasma frequency ω_p. The highlighted regions above and below ω_p are discussed in the text.

one direction. This fact has a significant influence on the optical properties justifying the delimitation from the Lorentz oscillator.

4.2.3 Dielectric Function of Ag Bulk

The Drude model alone does not accurately describe the optical properties of metals. Although it gives precise results in the infrared region, it becomes inaccurate for the visible region. Johnson and Christy measured the dielectric function of copper, silver and gold by transmission and reflection measurements under ultra high vacuum (UHV) conditions in the spectral range of $0.5 - 6.5\,\mathrm{eV}$ [Joh72]. In figure 4.3 the results of Johnson and Christy for silver are compared to the dielectric function $\epsilon^{\mathrm{Drude}}$ (equation (4.12)).

Their measurements show that the Drude model fails for high energies above $3.8\,\mathrm{eV}$, especially for the imaginary part. The additional contributions at high energies are caused by excitations of bound electrons from deeper bands into the conduction band. For noble metals these so-called interband transitions originate from completely filled d bands close to the Fermi energy. Further deviations derive from the fact that the conduction band is non-parabolic for high energies. The interband contributions are calculated from the experimental data and the Drude model as follows:

$$\epsilon(\omega) = \underbrace{1 + \chi^{\mathrm{Drude}}}_{\epsilon^{\mathrm{Drude}}} + \chi^{\mathrm{inter}} \tag{4.13}$$

$$\overset{(4.12)}{=} 1 - \frac{\omega_p^2}{\omega^2 + i\gamma\omega} + \chi^{\mathrm{inter}} \tag{4.14}$$

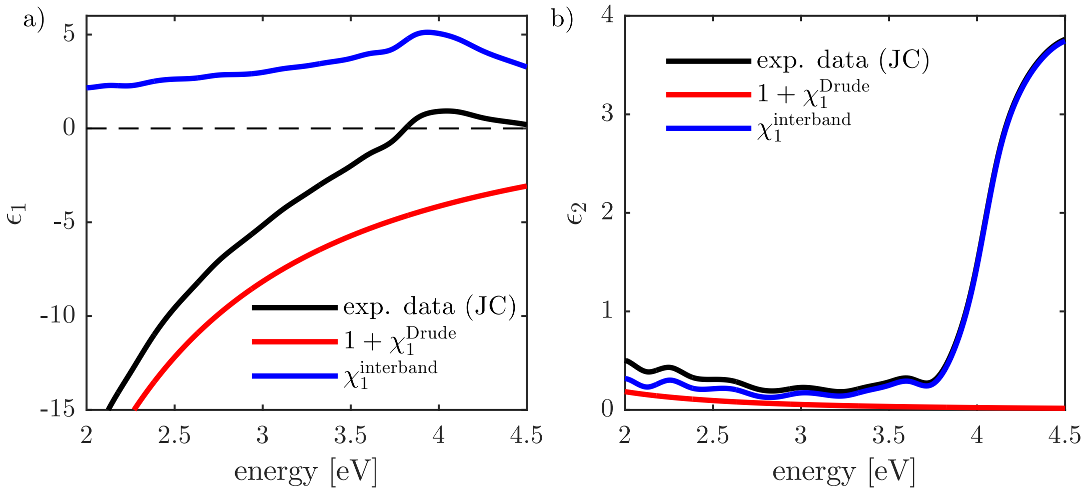

Figure 4.3: The real (a)) and imaginary (b)) part for different dielectric functions: The black line shows the data of Ag bulk measured by Johnson and Christy [Joh72]. In comparison to that, the red line displays the dielectric function calculated using the Drude model (equation (4.12)). As described in the text, both lines deviate from each other at high energies, attributable to the interband transitions from the 4s to 5pd state (blue line, calculated from the difference of measured Ag bulk data to the Drude model). As a consequence the position $\epsilon_1 = 0$ derived from the Drude model at $9.2\,\mathrm{eV}$ shifts to $3.8\,\mathrm{eV}$ due to the contribution of bound charges.

Both real and imaginary part of the interband contribution can be approximated as a real constant of 2.5 for small energies, while they change to a complex frequency dependent function for higher energies.

From the low-frequency limit ($\hbar\omega < 0.1\,\mathrm{eV}$) of the data they were able to calculate the effective masses m^* and relaxation times τ. The so-called Drude parameters for silver are $n = 5.9 \cdot 10^{28}\,\mathrm{m}^{-3}$, $m_{\mathrm{eff}} = m_e$, $\hbar\omega_p = 9.08\,\mathrm{eV}$ and $\hbar\gamma_0 = 0.018\,\mathrm{eV}$ [Kre69]. In comparison, figure 4.3 shows the dielectric function calculated $\epsilon^{\mathrm{Drude}}$ from equation (4.12).

4.2.4 Dielectric Function of Ag Clusters

The dielectric function of small silver clusters differs from the dielectric function of silver bulk. The mean free path $l_\infty = 52\,\mathrm{nm}$ in bulk silver [Ehr62] is restricted by scattering at phonons or lattice defects. Hence, the damping is given by $\gamma_0 = 1/\tau_\infty = \frac{v_F}{l_\infty}$, where $1/\tau_\infty$ stands for the relaxation frequency and $v_F = 1.4 \cdot 10^6\,\mathrm{m/s}$ denotes the Fermi velocity of silver.

Considering clusters with a diameter comparable or smaller than l_∞, additional damping resulting from collisions of the free electrons with the cluster surface needs to be taken into account. This process is known as the *free path effect* and was theoretically predicted in 1939 [Dav39]. First experimental evidence was found in 1958 [Fra58; Ham58a; Ham58b], followed by a quantitative comparison between theory and experiment in 1969 [Kre69]. This results in an additional damping process, which is added to the former damping process, resulting in a reduced effective mean free path and thus an increased damping, which now depends on the cluster radius R:

$$\gamma = \gamma_0 + \gamma_{\text{surface}} = \frac{1}{\tau_\infty} + \frac{1}{\tau_{\text{surface}}} = \frac{v_F}{l_\infty} + A \cdot \frac{v_F}{R} \tag{4.15}$$

The parameter A gives the effectiveness of single electron impact with the cluster surface. For isotropic scattering A has a value of 1. It turns out that the free path effect is not sufficient to describe the behavior of measured cluster resonances. A is found to be dependent on the surface chemistry (i.e. type and strength of chemical interactions at the surface), which influences the electron density as well. Therefore the A parameter is considered to consist of two parts [Per93]:

$$A = A_{\text{size}} + A_{\text{interface}} \tag{4.16}$$

The value of A_{size} was experimentally determined by Hövel for 2 nm Ag clusters in vacuum [Höv95]. For embedded clusters $A_{\text{interface}}$ the so-called chemical interface damping includes details about the cluster/matrix interface [Höv93].

To calculate the dielectric function for small particles one uses the dielectric function of silver bulk, subtracted by the Drude dielectric function. The remaining part yields the interband contribution discussed in section 4.2.2. Afterwards a modified Drude dielectric function with additional damping $\gamma = \gamma_0 + \gamma_{\text{surface}}$ according to equation (4.15) is added:

$$\epsilon^{\text{cluster}}(\omega, R) = \epsilon^{\text{bulk}}(\omega) - \frac{\omega_p^2}{\omega^2 + i\omega\gamma_0} + \frac{\omega_p^2}{\omega^2 + i\omega\left(\gamma_0 + A\frac{v_F}{R}\right)} \tag{4.17}$$

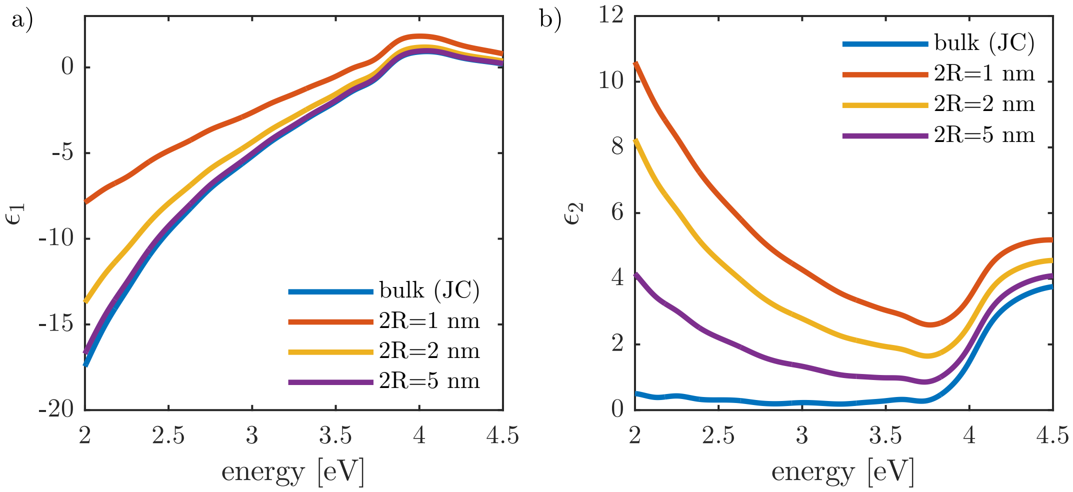

Figure 4.4: The real (a)) and imaginary (b)) parts of the dielectric function of clusters with different diameters from $2R = 1$ nm to $2R = 5$ nm according to equation (4.17)) in comparison to the experimental values for silver bulk from Johnson and Christy [Joh72]. A damping constant of $A = 1$ was chosen.

Figure 4.4 shows both real and imaginary part for Ag clusters with different radii compared to the bulk measurement. The deviation for different cluster radii is based on the $1/R$ dependency (equation (4.15)) of the surface damping constant. According to equation (4.12) ϵ_1 is hardly dependent on γ, while ϵ_2 is strongly influenced.

The next chapter discusses the interaction between small clusters (whose dielectric function was derived above) and light, that can be absorbed or scattered by the cluster. Here also the influence of the A parameter on the cluster plasmon resonance is going to be discussed.

4.3 Absorption From Small Silver Clusters: Plasmon Resonances

4.3.1 Mie Theory

The analytical solution of Maxwell's equations for scattering and absorption from a single isolated sphere of arbitrary size embedded in a linear, isotropic, homogenous medium is nowadays attributed to Gustav Mie [Mie08]. A complete derivation can be found in [Boh98]; only a brief introduction of Mie's solution will be given in the following section.

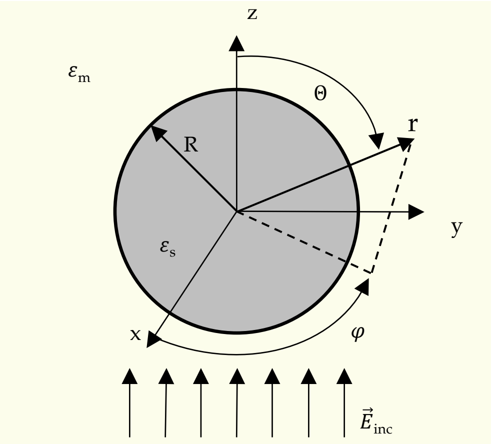

Figure 4.5: Sketch of an incident plane wave being absorbed and scattered at a sphere embedded in a medium with a dielectric function ϵ_m [Qui11].

Due to the spherical geometry spherical vector harmonics are used for the description of scattered and interior fields. As depicted in figure 4.5 the incident plane wave $\vec{E}_{\text{inc}} = E_0 e^{ik_z z}\vec{e}_x$ is chosen to propagate along the positive z-axis. The sphere may have a complex refractive index n and is embedded in a medium with refractive index n_m. The Maxwell relation links the refractive index n with the dielectric function ϵ:

$$\epsilon = \epsilon_1 + i\epsilon_2 \tag{4.18}$$

$$= n^2 \tag{4.19}$$

$$= (\tilde{n} + i\tilde{k}) \tag{4.20}$$

Even though a planar wave does not have spherical symmetry, it is possible to express $\vec{E}_{\text{inc}}$ in terms of spherical vector harmoncis, i.e. vector functions solving the vector equation generated from scalar functions that solve the scalar wave equation

$$\left(\vec{\nabla}^2 + k^2\right)\vec{\psi} = 0. \tag{4.21}$$

Equation (4.21) is solved by separation of the variables describing the desired wave function of the incident field in spherical coordinates:

$$\psi_{emn} = \cos(m\phi) P_n^m(\cos\theta) z_n(kr) \tag{4.22}$$

$$\psi_{omn} = \sin(m\phi) P_n^m(\cos\theta) z_n(kr) \tag{4.23}$$

An even (subscript e) and an odd (subscript o) solution is obtained accounting for the change of the azimuthal angle from ϕ to $-\phi$. $P_n^m(\cos\theta)$ are Legendre polynomials determining the polar angle θ. The last part of the solution $z_n(kr)$ giving the radial dependence stands for any of the four spherical Bessel functions j_n, spherical Neumann functions γ_n or spherical Hankel functions of first or second kind $h_n^{(1)}$ or $h_n^{(2)}$, respectively.

From these spherical harmonics $\psi_{\substack{o\\e}nm}$ a set of linearly independent and orthogonal spherical vector harmonics is calculated

$$\vec{M} = \vec{\nabla} \times (c\psi) \qquad \text{and} \qquad \vec{N} = \frac{\vec{\nabla} \times \vec{M}}{k} \tag{4.24}$$

with $\vec{\nabla} \times \vec{N} = k\vec{M}$. The $\vec{M}$ fields are electric type fields, thus have no radial magnetic field components. Inversely, the $\vec{N}$ fields do not have radial electric compounds and describe the magnetic modes. From equation (4.24) any solution for electromagnetic fields can be calculated. Again, due to the spherical symmetry, these equations are restricted to $m = \pm 1$ eliminating the sum over m. Concluding, incident (*inc*), scattered (*sca*) and the wave inside the cluster (*ins*) can be expressed in terms of the vector spherical harmonics:

$$\vec{E}_{\text{inc}} = E_0 \sum_{n=1}^{\infty} i^n \frac{2n+1}{n(n+1)} \left(\vec{M}^1_{o1n} - i\vec{N}^1_{e1n}\right) \tag{4.25}$$

$$\vec{H}_{\text{inc}} = \frac{-k}{\omega\mu} E_0 \sum_{n=1}^{\infty} i^n \frac{2n+1}{n(n+1)} \left(\vec{M}^1_{e1n} - i\vec{N}^1_{o1n}\right) \tag{4.26}$$

The expression for the field inside the sphere and the scattered field in terms of the incident field is given by:

$$\vec{E}_{\text{ins}} = \sum_{n=1}^{\infty} E_n \left(c_n \vec{M}^1_{o1n} - i d_n \vec{N}^1_{e1n} \right) \qquad \vec{H}_{\text{ins}} = \frac{-k_c}{\omega \mu_c} \sum_{n=1}^{\infty} E_n \left(d_n \vec{M}^1_{e1n} - i c_n \vec{N}^1_{o1n} \right) \tag{4.27}$$

$$\vec{E}_{\text{sca}} = \sum_{n=1}^{\infty} E_n \left(i a_n \vec{N}^3_{e1n} - b_n \vec{M}^3_{o1n} \right) \qquad \vec{H}_{\text{sca}} = \frac{k}{\omega \mu} \sum_{n=1}^{\infty} E_n \left(i b_n \vec{N}^3_{e1n} + a_n \vec{M}^3_{o1n} \right) \tag{4.28}$$

The physical meaning of the sum over n is that the fields are expanded to linearly independent radiating multipoles with order of n. a_n, b_n, c_n and d_n are called Mie coefficients and can be calculated from the boundary conditions at the surface of the sphere. The tangential components of the $\vec{E}$ and $\vec{H}$ field must be continuous at the interface of the sphere:

$$(\vec{E}_{inc} + \vec{E}_{sca} - \vec{E}_{ins}) \times \vec{\hat{e}}_r \Big|_{r=R} = 0 = (\vec{H}_{inc} + \vec{H}_{sca} - \vec{H}_{ins}) \times \vec{\hat{e}}_r \,|_{r=R} \tag{4.29}$$

From this boundary condition it is possible to determine all unknown expansion coefficients a_n, b_n, c_n and d_n. Since we are interested in scattering and absorption, only a_n and b_n are given here. The whole set of coefficients can be found in [Boh98].

$$a_n = \frac{m\psi_n(mx)\psi_n'(x) - \psi_n(x)\psi_n'(mx)}{m\psi_n(mx)\xi_n'(x) - \xi_n(x)\psi_n'(mx)} \tag{4.30}$$

$$b_n = \frac{\psi_n(mx)\psi_n'(x) - m\psi_n(x)\psi_n'(mx)}{\psi_n(mx)\xi_n'(x) - m\xi_n(x)\psi_n'(mx)} \tag{4.31}$$

$\psi_n(x) = x j^1_n(x)$ and $\xi_n(x) = x h^1_n(x)$ are the Riccati-Bessel functions and the prime denotes the derivation with respect to the argument. Further the abbreviations $x = kr$ and $m = N_{\text{s}}/N_{\text{m}}$ for the ratio of the refractive indices of sphere and embedding medium are used. For increasing n the Mie coefficients decrease so that the infinite sums can be evaluated and neglected above a certain threshold. In the end the scattering cross section and the absorption cross section are calculated. A cross section is defined as $\sigma_{\text{sca/abs}} = \frac{P_{\text{sca/abs}}}{I_{\text{inc}}}$, defined by the scattered or absorbed power, normalized to the incident intensity I_{inc}. With the extinction cross section [Boh98]

$$\sigma_{\text{ext}} = \sigma_{\text{sca}} + \sigma_{\text{abs}} \tag{4.32}$$

the cross sections are calculated [Boh98]:

$$\sigma_{\text{sca}} = \frac{2\pi}{k^2} \sum_{n=1}^{\infty} (2n+1) \left(|a_n|^2 + |b_n|^2 \right) \tag{4.33}$$

$$\sigma_{\text{ext}} = \frac{2\pi}{k^2} \sum_{n=1}^{\infty} (2n+1) \Re \left(a_n + b_n \right) \tag{4.34}$$

4.3.2 Small Spherical Particles

Scattering of electromagnetic radiation by particles with a diameter $2R$ much smaller than the wavelength of the radiation λ is called Rayleigh scattering. Precisely, for silver cluster the condition is $2R < 15\,\mathrm{nm}$. The case of Rayleigh scattering simplifies the results derived by Mie's theory since the spherical Bessel functions, written in power series expression, can be canceled after the first terms. For $|m|x \ll 1$ equation (4.34) now reads

$$\begin{aligned}
\sigma_{\text{ext}} &= 4\pi R^2 x \Im\left(\frac{m^2-1}{m^2+2}\right) && (4.35)\\
&= 4\pi R^3 k \Im\left(\frac{n_{\text{s}}^2-n_{\text{e}}^2}{n_{\text{s}}^2+2n_{\text{e}}^2}\right) && (4.36)\\
&\overset{n^2=\epsilon}{=} 4\pi R^3 k \Im\left(\frac{\epsilon_{\text{s}}-\epsilon_{\text{m}}}{\epsilon_{\text{s}}+2\epsilon_{\text{m}}}\right) && (4.37)\\
&= 4\pi R^3 k \frac{\epsilon_2 \epsilon_{\text{m}}}{(2\epsilon_{\text{m}}+\epsilon_1)+\epsilon_2^2} && (4.38)\\
&= 9\frac{\omega}{c}\epsilon_m^{3/2} V_0 \frac{\epsilon_2(\omega)}{(\epsilon_1(\omega)+2\epsilon_m)^2+\epsilon_2(\omega)^2}. && (4.39)
\end{aligned}$$

Note that the dielectric function $\epsilon_{\text{s}} = \epsilon_1 + i\epsilon_2$ of the sphere was split up into its real and imaginary part. k was replaced by $\frac{n\omega}{c}$, c denotes the vacuum velocity of light and $V_0 = 4/3\pi R^3$ gives the volume of the cluster.

The same result for the absorption of small spherical particles can be obtained with the so-called electrostatic approximation, which can be calculated using simple electrostatics assuming molecular dipoles in the particle and a surface charge density at the surface. This yields for $2R \ll \lambda$ a simple connection between the extinction cross section and the molecular polarizability and consequently the same result as equation (4.39). For details see [Boh98].

4.3.3 Plasmon Resonance

For a cluster with given size and dielectric function (see equation (4.17)) equation (4.39) has a resonance for $\omega = \omega^*$, if

$$\epsilon_1(\omega^*) = -2\epsilon_m, \tag{4.40}$$

in case $\epsilon_2(\omega)$ is not too large. Moreover, ϵ_m should be real or should have only a small imaginary part, otherwise the electromagnetic wave would be damped and the assumption of a plane wave in Mie theory would not be valid anymore.

The frequency at which resonance occurs is called plasmon frequency. The electric field causes polarization charges at the cluster surface as shown in figure 4.6. The conduction

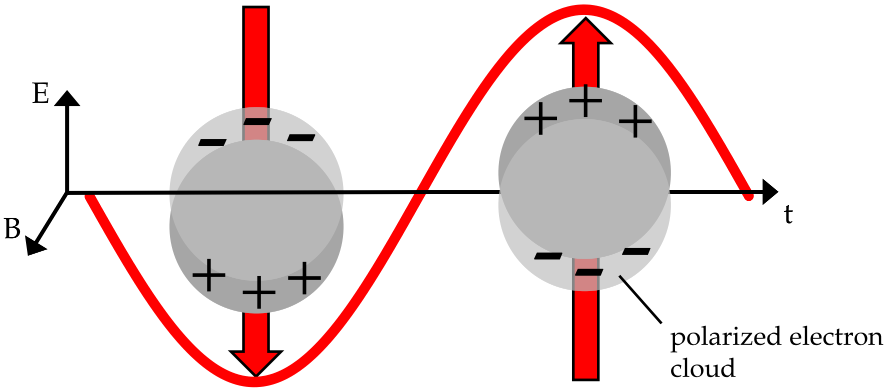

Figure 4.6: Excitation of particle plasmons through polarization of a metallic nanoparticle.

electrons oscillate with respect to positive background, being restored by the surface polarization. The restoring forces then determine the eigenfrequency of the system.

Influence of ϵ_m and chemical interface damping

For the following considerations a cluster size of 2R=2 nm will be used. On the basis of figure 4.7 position of shape of the cluster plasmon resonance (equation (4.40)) will be discussed. Figure 4.7a) illustrates that the resonance condition is fulfilled depending on ϵ_m.

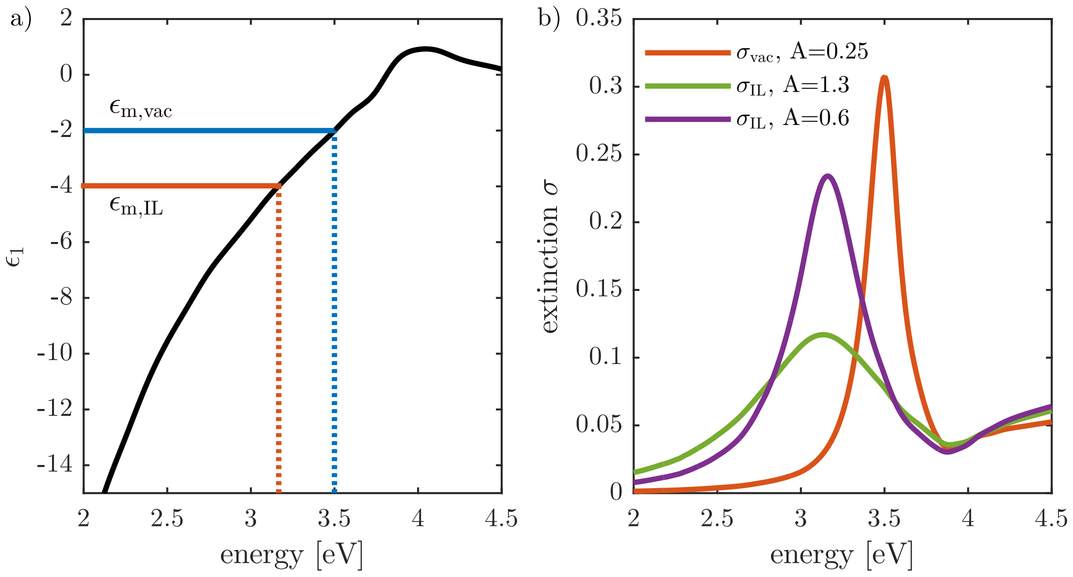

Figure 4.7: Influence of the dielectric function of the embedding medium ϵ_m on position and shape of the cluster plasmon. a) shows the energetic dependence $\epsilon_1(E)$ at the resonance condition $\epsilon_1 = -2\epsilon_m$ for vacuum ($\epsilon_m = 1$, blue) and C_4MIM PF_6 ($\epsilon_m = n^2 = 2.022$, red). Here the dielectric function for a cluster with 2 nm radius (black) is considered (compare figure 4.4). b) shows the resulting extinction spectra for both embedding media exhibiting maxima as shown in a) at E = 3.5 eV and E = 3.17 eV for vacuum and IL, respectively.

For a cluster in vacuum ($\epsilon_m = 1$) the resonance condition (4.40) is met for $\epsilon_1 \approx -2$, while the resonance for a cluster embedded in the ionic liquid C_4MIM PF_6 (refractive index $n = 1.422$

at 400 nm, $\epsilon_m = n^2$) yields $\epsilon_1 \approx -3.98$. Because ϵ_1, which is the real part of the dielectric function of the 2 nm cluster, in figure 4.4a) is a monotonously increasing function the energetic position of the plasmon resonance shifts to lower energies with increasing ϵ_m. For the above mentioned examples, vacuum and ionic liquid, using the resonance condition $\epsilon_1(\omega) = -2\epsilon_m$, we obtain resonances at E $\approx$ 3.5 eV for vacuum and at E $\approx$ 3.17 eV for C_4MIM PF_6 as indicated by the dotted lines. Note, that for the calculation of ϵ_1 (equation (4.17)) an A parameter of 1 was chosen, but since ϵ_1 is only weakly dependent on the damping γ for $\frac{A}{2R} < 1\,\text{nm}^{-1}$ (see figure 4.4) and therefore on A, the choice of the A parameter is not important at this point.

After having discussed the dependence of the peak position on the embedding medium, figure 4.7b) now shows the corresponding plasmon spectra calculated with equation 4.39. The maximum of the cluster plasmon resonance is shifted from 3.5 eV to 3.17 eV for σ_{vac} and σ_{IL}. As it can be understood from figure 4.7b) the A parameter introduced in section 4.2.4 has significant influence on the cluster plasmon resonance shape. Since influences from embedding media can be excluded in vacuum, an A parameter of 0.25 was chosen for the calculation of σ_{vac}. This result was obtained from measurements of a free cluster beam in THECLA [Höv95]. The A parameters of 0.6 and 1.3 are typical values obtained in the measurements of clusters in ionic liquids as discussed in section 5.1.1. For higher values of the A parameter the resonance is broadened, resulting in a higher full width at half maximum (FWHM). In the case shown in figure 4.7b) the FWHM of σ_{IL} increases from 0.49 eV to 0.96 eV, if the A parameter is increased from 0.6 to 1.3. The FWHM is defined as the double width between the peak $\hbar\omega^*$ and the low energy flank $\hbar\omega_{1/2}$ at half of the intensity of the maximum: $\hbar\Gamma = 2 \cdot (\hbar\omega^* - \hbar\omega_{1/2})$. The high energy flank is not used because it is influenced by interband transitions (cf. section 4.2.3). Using the approximation $\gamma_0 \ll \omega_p$, the FWHM becomes

$$\Gamma(R) \approx \Gamma_0 + A \cdot \frac{2\omega_p^2/\omega_1^3}{\left|\left(\left.\frac{d\epsilon_1}{d\omega}\right|_{\omega^*}\right)\right|} \cdot \frac{v_F}{R}. \tag{4.41}$$

Γ_0 denotes the FWHM for the plasmon resonance using $\epsilon(\omega)$ of the bulk metal.

Influence of Cluster Radius

The influence of the cluster radius on the cluster plasmon resonance is presented in figure 4.8a) for clusters with diameters between 1 nm and 50 nm. An A parameter of $A = 1$ and $n = 1.75$ have been chosen (see section 5.1.1 for the reason of choosing this value). The spectra have been calculated using Mie's theory in consideration of the damping effects caused by the cluster surface. The used code is implemented in python [Lei16], freely available and has been validated in the framework of A. Kononov's master thesis [Kon17]. All extinction spectra are normalized to the cross section $A = \pi R^2$. For cluster radii smaller than

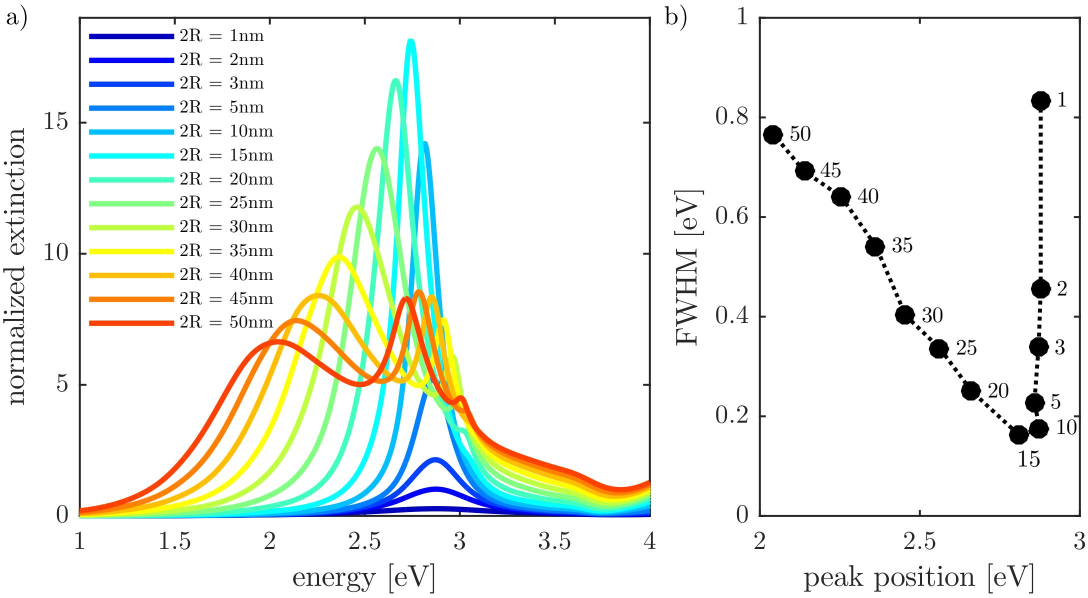

Figure 4.8: a) Extinction spectra for cluster with different radii, $A = 1$ and $n = 1.75$. For clusters with a diameter larger than 10 nm multipoles of Mie's theory cannot be neglected anymore, thus the resonance structure splits up and shifts to longer wavelengths with increasing cluster size. b) shows the relation between FWHM and peak position of the resonance structure, depending on the cluster size. The numbers indicate the corresponding cluster diameter in nm.

5 nm the cluster plasmon resonance looks similar to the spectra calculated using dipole approximation. For clusters larger than 5 nm (cf. section 4.3.2) the dipole approximation is not valid anymore because the Mie coefficients for higher order multipoles (4.31) cannot be neglected. In general, for larger particles the resonance splits into an increasing number of resonances. The peak structures are broadened and shift to longer wavelengths. In figure 4.8b) the full width half maximum (FWHM) $\hbar\Gamma$ is plotted against the peak position. This kind of representation reminds of the letter C and was introduced by Berg *et al.* as "C curve" [Ber91].

The clusters investigated in this thesis have a diameter of (2 ± 0.6) nm (cf. section 3.1) and are therefore small enough to be treated in dipole approximation (equation (4.39)). The corresponding plasmon resonances together with the corresponding part of the C curve are shown in figure 4.9. Due to the relation $\sigma_{\text{ext}} \propto R^3$ the extinction increases with increasing cluster radius. The peak position does not shift in the considered range between 0.7 and 1.3 nm. Therefore it is legitimate to use a cluster with a diameter of 2 nm to describe the plasmon resonances of clusters produced with a size distribution of $R = (1 \pm 0.3)$ nm in THECLA.

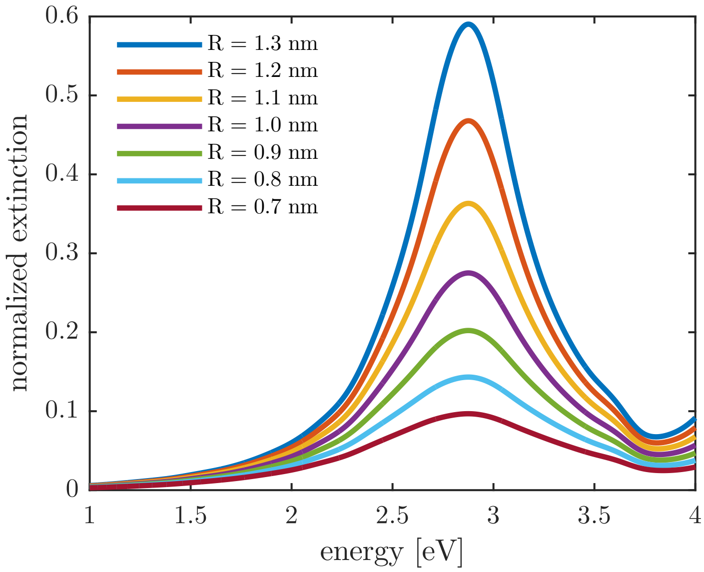

Figure 4.9: Extinction spectra for the cluster sizes produced in THECLA ($(2 \pm 0.6)\,\mathrm{nm}$). Since the peak position does not shift in this size distribution a mean diameter of 2 nm can be assumed for cluster plasmon resonance calculations for clusters produced in THECLA.

4.3.4 Generalized Mie Theory

If clusters are approaching (coalescing or aggregating, see figure 2.1), they are coupling electromagnetically. There is a breakdown of the single-particle approximation, if clusters in a sample come close together. However, Mie's theory, which describes the absorption from single spheres, can quite easily be extended in the so-called Generalized Mie Theory (GMT). For a theoretical calculation, an explicit knowledge of the sample topology including all interparticle distances is essential. A possible geometry is shown in figure 4.10.

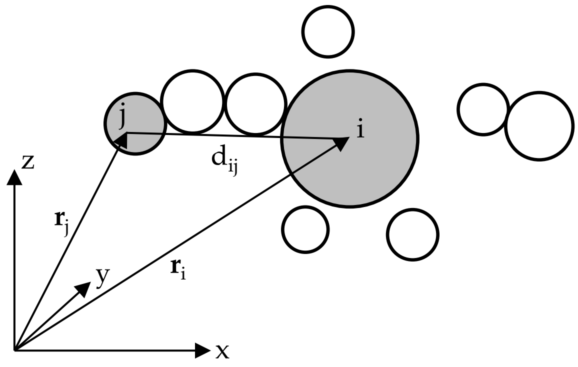

Figure 4.10: Aggregate of spherical particles [Qui11].

Due to neighboring spheres the symmetry of the problem is reduced, which means that also vector harmonics with $m \neq 1$ (equations (4.22) and (4.23)) contribute to the field expansions. The spherical wave functions describe the fields around each sphere, independently satisfying the boundary conditions at the sphere interfaces.

By linearly superimposing all incident and scattered fields the electromagnetic fields $\vec{E}$ and $\vec{H}$ outside the aggregate can be calculated:

$$\vec{E} = \vec{E}_{\text{inc}} + \sum_{j=1}^{N} \vec{E}_{\text{sca}}(j) \tag{4.42}$$

$$\vec{H} = \vec{H}_{\text{inc}} + \sum_{j=1}^{N} \vec{H}_{\text{sca}}(j) \tag{4.43}$$

Details on the GMT are given in Gérardy and Ausloos [Gér82]. Usually the equations obtained from GMT are solved numerically. In this thesis the Fortran 90 implementation *py_gmm* by Pellegrini *et al.* is used [Pel07]. This code is able to model far- as well as local-field properties of arbitrarily formed cluster aggregates for any incident field polarizations and was validated here by comparing the calculated spectra to those given by Quinten [Qui11].

The effect of electromagnetic coupling between clusters will be discussed for some exemplary geometries. At first a dimer consisting of two Ag clusters with a diameter of 2 nm is considered. The dielectric function of Ag clusters according to equation (4.17) was used with $A = 1$. A refractive index of $n = 1.75$ (see section 5.1.1 for details on choosing this value) has been used. Up to 25 multipoles are included in the calculations in order to reach convergence.

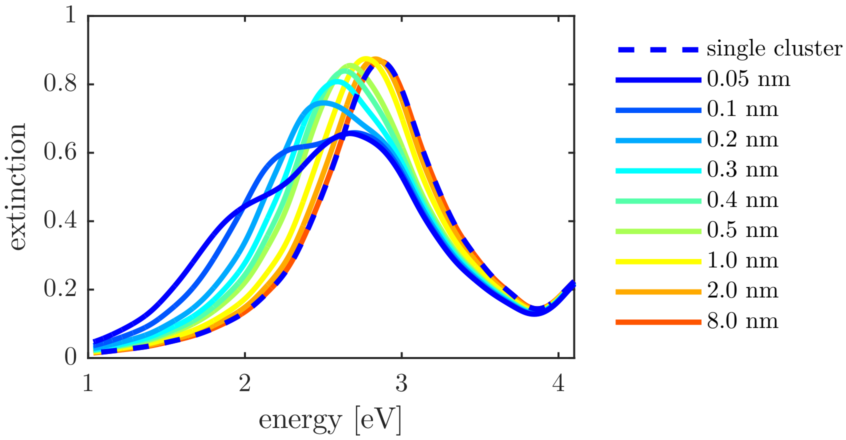

Figure 4.11: Influence of the interparticle distance d_{ij} on simulated extinction spectra of an Ag dimer ($2R = 2\,\text{nm}$, $A = 1$, $n = 1.75$) compared to the single particle spectrum (dashed line).

Figure 4.11 shows the resulting spectra calculated using the *py_gmm* code for different interparticle distances compared to a single 2 nm Ag cluster (dashed line). For decreasing distance an increasing redshift is clearly visible. As the particles approach, the structure becomes broadened and multipolar resonances appear at higher wavelengths resulting from the electromagnetical coupling of the particles in the aggregate. The peak splitting decreases with decreasing interparticle distance d_{ij}. The interband transition region remains unaffected. For $d_{ij} \geq 4 \cdot 2R$ the distance between the particles is too large and the interaction between the particles does not affect the optical extinction, which in this case is similar to the extinction of a single cluster.

In a next step the interparticle distance is set to 0.05 nm and linear chain arrangements of clusters are investigated, which are the expected form for aggregation in liquids [Sme05]. Figure 4.12 shows the influence of the chain length on the extinction spectrum. The other parameters are the same used for the investigation of the influence on the interparticle distance. The longer the chain is, the larger is the redshift. These effect is expected to saturate for long chains [Qui93], which can be seen in figure 4.12 for $N > 5$.

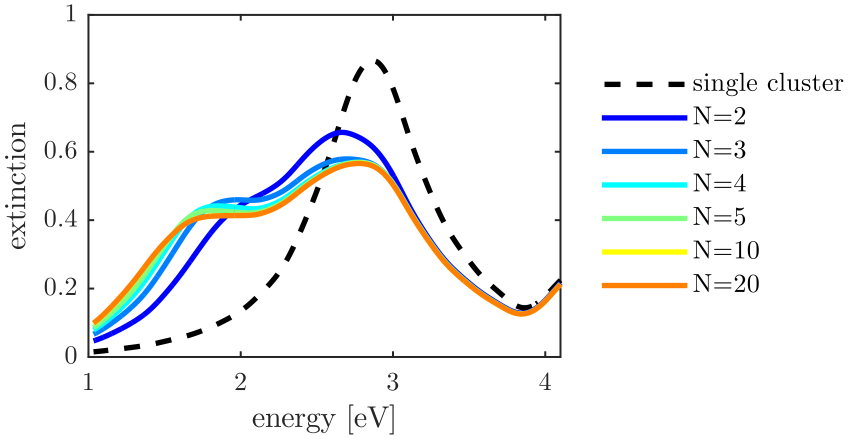

Figure 4.12: Influence of the chain length on simulated extinction spectra compared to the single particle spectrum (dashed line). The linear chains consist of N 2 nm Ag clusters with an interparticle distance of 0.05 nm.

Figure 4.13 shows the extinction spectra for other aggregate structures inspired by [Qui93] consisting of up to $N = 5$ clusters. The parameters for the calculations remain the same. In sake of clarity the spectra are shifted arbitrarily. For aggregated clusters the single resonance splits up and the main peak shifts to lower energies as seen for previously discussed calculations. The split can be explained by the model representation of coupled oscillators, since the resonances are present in the single particle and they are electromagnetically coupled. For silver clusters additional resonances at higher energies are suppressed due to the onset of interband transitions. The largest splitting occurs for chain-like aggregates (pink lines), while densely packed aggregates (light blue lines) show the smallest peak splitting. The results of this calculations are in agreement with [Qui93].

The results obtained by GMT calculations suggest the idea of using measured spectra in order to determine explicitly the topology of the aggregate. However, for a sample consisting of several aggregated clusters resulting spectrum is broadened since the spectra of the various extinction cross sections are summed up with the weights w_i defining their distribution in the sample [Gal99]:

$$\sigma_{\text{ext, aggregate}} = \sum_i w_i \sigma_{\text{ext}}(i) \tag{4.44}$$

Thus, a simple assignment of peaks in the spectrum to a specific form of aggregate is impossible. The presence of separated single particles results in contributions at short wavelengths. Peaks at longer wavelengths can on the one hand originate from the splitting due

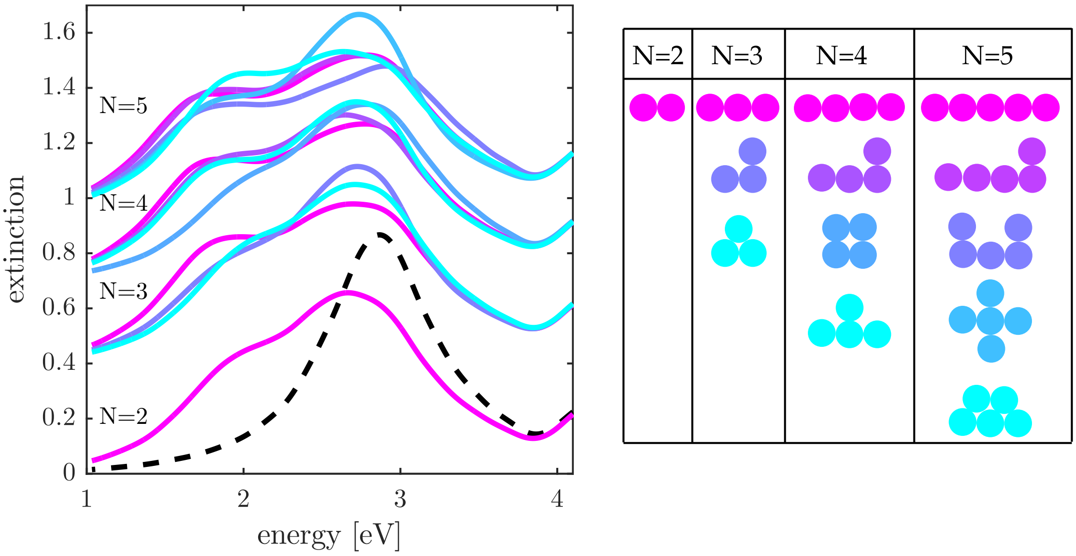

Figure 4.13: Extinction spectra for different planar aggregates consisting of N 2 nm Ag clusters calculated with the *py_gmm* code. For comparison the extinction spectrum of a single 2 nm Ag cluster (dashed black line) is also shown. The spectra are plotted with an offset for reasons of clarity.

to chain-like aggregates or on the other hand by multipole excitation in large (diameter $\approx 20\,\mathrm{nm}$ and above, see figure 4.8) clusters.

Therefore, only qualitative conclusions about the size and the topology of the aggregate should be drawn from the extinction spectra.

4.4 Experimental Implementation

4.4.1 Extinction Cross Section

Experimentally the extinction cross section $\sigma_{\text{ext}} = \sigma_{\text{abs}} + \sigma_{\text{sca}}$ cannot be measured at a single cluster. Instead of that one is always dealing with a sample with thickness d and cluster density n_{cluster}. In case the clusters are spatially separated ($R_{\text{NN}} > 5R$) within the sample, Lambert-Beer's law gives

$$I(x) = I_0 \exp(-n_{\text{cluster}} \cdot \sigma_{\text{ext}} \cdot d). \tag{4.45}$$

In spectroscopy a common measurand is the extinction, which can be calculated from the transmission $\frac{I}{I_0}$

$$\text{extinction} \equiv -\lg \frac{I}{I_0}. \tag{4.46}$$

Usually, $I_0 = I(0)$ is determined by a reference measurement (empty cuvette or pure ionic liquid, if clusters embedded in an ionic liquid are investigated). $I = I(d)$ denotes the intensity behind the sample. For the extinction an expression is obtained, that is proportional to σ_{ext}:

$$\text{extinction} = \frac{1}{\ln_{10}} n_{\text{cluster}} \cdot d \cdot \sigma_{\text{ext}} \tag{4.47}$$

The scaling factor depends on the cluster density and the sample thickness, which has to be considered, when measurements of a sample in a cuvette and in the mixer are compared to each other. Since equation (4.47) is valid for samples with $R_{\text{NN}} > 5R$, it requires a low filling factor $f = \frac{V_{\text{cluster}}}{V_{\text{sample}}} < 5 \cdot 10^{-2}$.

4.4.2 Optical Setup

All optical experiments were carried out with an Avantes AvaLight-DH-S-BAL light source, consisting of a deep ultra violet deuterium bulb and a balanced halogen bulb. The spectral range of the lamp is $\lambda = 190 - 2500\,\text{nm}$. The light is guided through fiber optic cables and focused at the sample by lenses. After having passed the sample, the light is collected by a second lens onto the entrance of a second fiber optic cable, that is connected with an Avantes AvaSpec-2048x14 spectrometer (spectral range $\lambda = 200 - 1100\,\text{nm}$, resolution: $\Delta\lambda = 1.4\,\text{nm}$). The spectrometer consists of a 2048x14 pixels high UV sensitive CCD image sensor and a $16\,\text{bit}$ AD converter, expressing the electrical output of the sensor as the number of counts per mJ of incident radiation and per ms integration time.

All measured intensities need to be corrected by the intensity of the dark counts. These are the counts detected by the spectrometer with switched off light source. Before the extinction of a cluster sample can be measured, a reference measurement of a pure IL is taken. The extinction is then be measured as follows:

$$\begin{aligned} \text{extinction} &= -\lg(\frac{I}{I_0}) \qquad (4.48) \\ &= -\lg\left(\frac{I_{\text{cluster}} - I_{\text{dark}}}{I_{\text{ref}} - I_{\text{dark}}}\right) \qquad (4.49) \end{aligned}$$

In-situ UV/Vis Spectroscopy

As already mentioned in section 3.3, fused silica windows at both sides of the mixer enable UV/vis transmission measurements during cluster deposition with an optical path length of $6\,\text{cm}$. A reference measurement (pure IL) is recorded before the deposition starts. The integration time for all *in-situ* measurements is chosen much larger ($30\,\text{s}$) than the rotation frequency of the roller, which is about one rotation per second. To make sure no interfering light is collected in the spectrometer, all optical measurements are performed in a darkened room.

Ex-situ UV/Vis Spectroscopy

After finishing the cluster deposition, the cluster source needs to be shut down (slow reduction of electric current that heats the tantalum foil in the cluster source and turn off of the argon pressure). To ensure no more clusters are hitting the surface of the roller a shutter is moved into the cluster beam (see figure 3.4). During the shut down process, that usually takes several minutes, the optical measurements are continued to control height and shape of the cluster plasmon. For a fast sample removal after deposition a UHV gate valve is used to separate the experimental chamber from the cryogenic stage. After removing the clusters dissolved in the ionic liquid from the tub, the sample is filled into a cuvette (macro cuvette: V=3 ml, micro cuvette V=70 μl), either made from silica glass or PMMA. Both cuvettes have an optical path length of 10 mm and are transparent above $\lambda = 200$ nm. Pure ionic liquid was placed in a glass container inside the experimental chamber during deposition, underlying the same degas conditions as the ionic liquid used for cluster deposition, serving as a reference for the *ex-situ* extinction measurements.

The cuvettes are placed in an AVANTES cuvette holder to ensure reproducibility of the measurements at a fixed position. The cuvette holder has two collimating lenses with an adjustable focus for maximum light throughput. An aluminum cover is available to suppress influences from diffuse light.

4.4.3 UV/Vis Spectrum of Ionic Liquids

Although the spectrometer has a spectral range of $\lambda = 190 - 2500$ nm (which corresponds to energies between 1.13 and 6.2 eV), UV/Vis spectra discussed in this thesis will only contain data up to a certain energy. The reason for this is the limited transmission of ionic liquids in the UV range. Figure 4.14 shows the raw counts for C_4MIM PF_6 in a quartz glass cuvette (blue line). The cuvette itself is transparent down to 200 nm, while C_4MIM PF_6 cuts off below 240 nm, which is consistent with the spectral shape reported by Billard *et al.* and Paul *et al.* [Bil03; Pau05].

Although the mixer is equipped with quartz glass windows as well, the optical adjustment, in particular the correct focus of the weak UV light for *in-situ* measurements in the mixer (red line), is error-prone. This results in a shift of the cutoff in the UV range to 323 nm. For the *in-situ* measurements themselves this is not a problem at all since the measured spectra are divided by the reference measurement of the pure IL according to equation (4.49). However, all optical spectra will only be plotted up to $\frac{1240}{323}$ eV$= 3.8$ eV since data below this cutoff wavelength do not contain any information. For reason of comparability also spectra measured in a cuvette will be shown in this limited energy range.

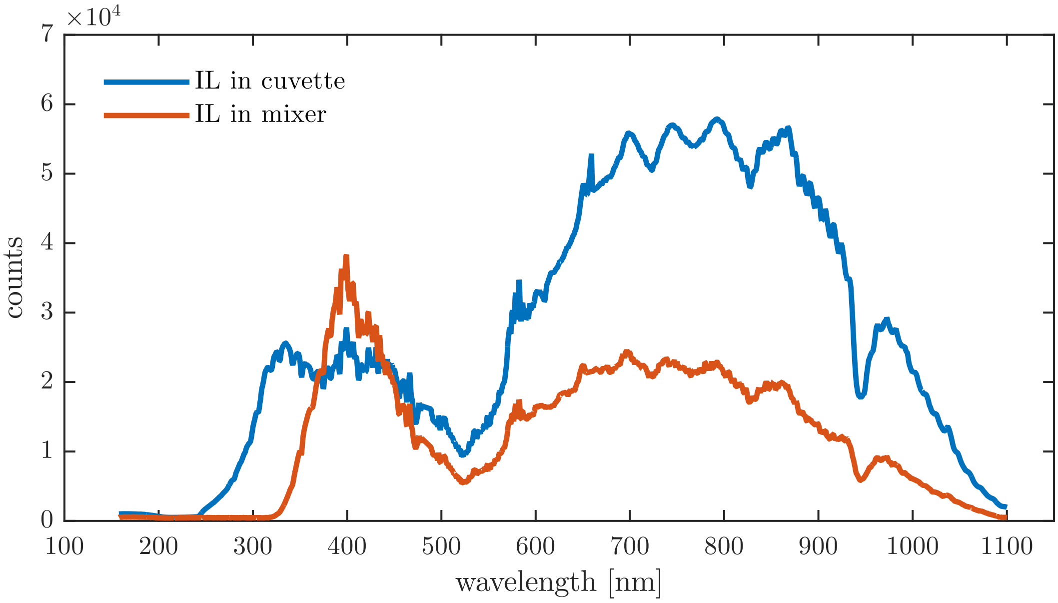

Figure 4.14: Raw counts of pure C_4MIM PF_6 in a quartz glass cuvette (blue line) and in the mixer (red line).

Depending on their composition (i.e. the combination of cation and anion) ionic liquids absorb below a certain wavelength. Amongst others, sufficient transmission is a major criterion for the choice of an appropriate IL. The silver cluster plasmon resonance position is expected to be around 400 nm (see section 4.3.3), so the IL needs to be transparent at that wavelength to obtain enough signal, which is ensured for C_4MIM PF_6. The transmission of the other investigated ionic liquids is discussed in section 5.3.

Chapter 5

Ionic Liquid–Cluster Interaction: Results of Optical Measurements

Previous experiments [Eng14] have revealed contradictory results concerning cluster plasmon resonance shape, color of the resulting IL-cluster mixture and sample stability. Even aggregation during cluster deposition and the formation of macroscopic cluster aggregates at the bottom of the tub have been observed. These effects have been assigned to different batches of IL. However, during cluster deposition several parameters such as cluster deposition rate, ionic liquid temperature and its water content can be tuned also influencing cluster plasmon resonance position and shape as well as sample stability. It is shown how the experimental parameters have to be tuned to obtain highly concentrated samples with separated Ag clusters.

Section 5.1 presents the *in-situ* spectra recorded during cluster deposition. From position and shape of the *in-situ* recorded cluster plasmon resonance conclusions on the cluster-environment interaction can be drawn by comparing the experimental results to the spectra obtained using Mie's theory introduced in chapter 4.3.1 for several shapes of aggregates.

In a next step (section 5.2) sample the longterm stability is investigated using *ex-situ* UV/Vis absorption spectroscopy and corresponding calculations using the Generalized Mie theory (see section 4.3.4). Storage temperature and thus viscosity is found to have a large effect on the sample stability.

Although literature reports that C_4MIM PF_6 is the most appropriate ionic liquid for cluster stabilization [Ric11], the first results of cluster deposition in different imidazolium-based ionic liquids is presented in section 5.3.

5.1 Characterization During Cluster Deposition

5.1.1 Data Treatment and Evaluation

This chapter gives an overview of typical data treatment of *in-situ* UV/Vis absorption spectra recorded during cluster deposition and their evaluation. After the ionic liquid has been dried under vacuum conditions at 80 °C to degas water impurities for 24 hours, it is filled into the tub of the mixer. A reference spectrum is taken while the mixer is in rotation. The cluster deposition onto the ionic liquid at the surface of the mixer has been described in section 3.3. Once the clusters are mixed into the ionic liquid in the tub, their plasmon is detected during the continuous *in-situ* UV/Vis absorption measurements. The corresponding extinction is calculated using equation (4.49). Separated clusters can be assumed because electromagnetic coupling starts for a cluster coverage ≥ 0.1 cluster monolayers at a surface, which corresponds to a film thickness of 0.12 nm [Hof12]. Since the frequency of the mixer is 1 Hz and the used deposition rates are ≤ 0.065 nm/s, the deposited amount during one roller rotation is far below this value.

Figure 5.1a) shows an example of those *in-situ* measurements recorded during the first 8.5 minutes of cluster deposition. Although a new UV/Vis absorption spectrum is recorded every 30 s, for reasons of clarity only selected spectra are presented. The cluster deposition rate used in this experiment was 0.3 Å/s. The entire deposition took 17 minutes. According to equation (3.13) this corresponds to a total amount of 233.29 µg, which results in an Ag concentration of 15.55 µg/ml.

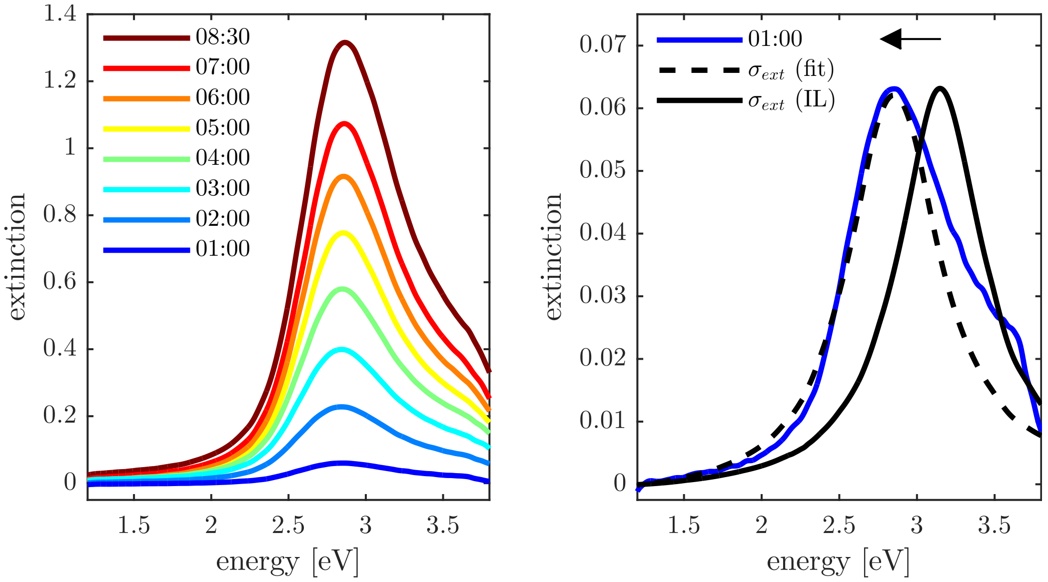

Figure 5.1: a) Cluster plasmon extinction spectra during deposition. With increasing amount of cluster material the extinction increases. The legend denotes the duration of the deposition in *MM:SS*. b) The parameters for the theoretical spectrum are aligned to match the data (dashed line). The solid black line represents the plasmon expected for a cluster embedded in a medium with the refractive index $n = 1.418$ of C_4MIM PF_6.

During cluster deposition the overall extinction increases due to the increasing amount of cluster material inside the sample. The cluster deposition rate was constant during deposition, which is reflected in the equidistant increase of the peak heights.

The measurement of the refractive index of C_4MIM PF_6 with an Abbe refractometer yields $n_{\mathrm{IL}} = 1.418$ at 400 nm. Inserting this value into equation (4.4), the theoretical extinction cross section of 2 nm Ag clusters in C_4MIM PF_6 can be calculated. The corresponding spectrum is given by the black solid line in figure 5.1b). It has a resonance maximum at 3.16 eV.

However, the previously discussed *ex-situ* measurements, here represented by the spectrum taken after one minute (blue spectrum), showing a resonance maximum at $2.85\,$eV, which is contrary to the expected peak position originating from the measured refractive index. Assuming a cluster diameter of $2\,$nm, equation (4.4) requires $n = 1.75$ to obtain the measured resonance maximum at $2.85\,$eV as indicated by the black dashed line in figure 5.1b). An A parameter of 0.82 was chosen to match the theoretical spectrum to the data. Note that the parameters in equation (4.39) were set in a way that the left flank is described by the theoretical spectrum since the right flank may be superimposed by interband transitions. For reasons of comparability the same A parameter of 0.82 was used to calculate the black solid spectrum in figure 5.1b).

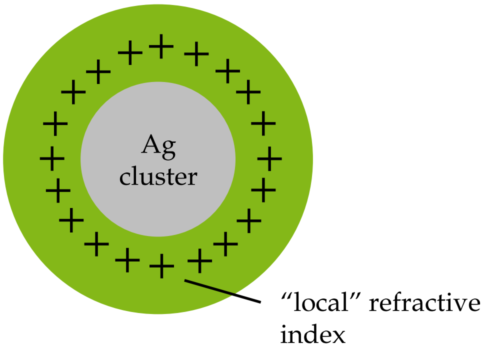

Figure 5.2: Schematic representation of the interaction between cluster and ionic liquid. The formation of a cation layer around the cluster influences the "local" refractive index.

Obviously the IL interacts with the embedded Ag clusters in a way that the "local" refractive index of the IL changes from $n = 1.418$ to $n = 1.75$, which leads to a plasmon peak shift to lower energies as indicated by the arrow in figure 5.1b). This is schematically shown in figure 5.2, supporting the model of a protective ionic layer around the clusters, which is a fundamental part of the stabilizing mechanism of ILs as introduced in section 2.2. The formation of a bilayer structure was for example confirmed in XPS studies [Cre08]. As the cations and anions have different chemical nature, they interact distinctly different with the clusters. Therefore the cluster surface is mainly surrounded by one sort of ions and a shell of counter ions [Kra11], resulting in an alteration of the local refractive index and eventually in a shift of the plasmon resonance. In a general sense, however, the details of the interface between cluster and ionic liquid modify the energetic position and width of the cluster plasmon resonance, which can be employed for "surface analysis by cluster plasmon spectroscopy" [Kre97].

5.1.2 Influence of Deposition Rate

During a large number of cluster depositions in ionic liquids different energetic positions for the maximum of the cluster plasmon resonance have been observed. Also cluster plasmon resonance shifts during deposition or changes of the FWHM occurred, caused by different interactions between cluster and ionic liquid (cf. section 4.3.3) or - in the latter case - by interaction of the clusters (cf. section 4.3.4) due to electromagnetic coupling.

Initially this behavior has been assigned to different batches of ionic liquids [Eng14] or slightly different conditions during the degassing process before cluster deposition, since it has been shown that for samples produced by sputtering remaining water impurities have significant influence on sample stability [Van12].

However, two comparative experiments using the same batch of IL, that have been treated identically during the degassing process, still revealed different spectra during deposition. The only parameter that differed in the experiments was the cluster deposition rate. The UV/Vis absorption spectra of these comparison experiments are shown in figure 5.3. The left figures show the development of the cluster plasmon, while in the right figure the spectra are normalized to equal the maximum.

Sample *DO59* is produced with a low cluster deposition rate of $0.075\,\text{Å/s}$ for 34 minutes, while a cluster deposition rate of $0.325\,\text{Å/s}$ for 16 minutes is used for *DO60*. The colors from blue to red show the development of the cluster plasmon resonance during deposition with increasing deposition time. For both experiments the normalized spectra show a shift of the peak position to higher energies during deposition, which is larger for sample *DO59* ($2.69\,\text{eV}$ to $2.85\,\text{eV}$) than for sample *DO60* ($2.78\,\text{eV}$ to $2.80\,\text{eV}$). Besides the shifted peak position both samples also have different FWHM. The FWHM of sample *DO59* increases during deposition from $0.52\,\text{eV}$ to $0.77\,\text{eV}$, while it stays almost constant for sample *DO59* ($0.62\,\text{eV}$ to $0.63\,\text{eV}$).

When the deposition is finished (after 34 and 15 minutes, respectively), the cluster source needs to be shut down, which takes approximately 15 to 20 minutes. After that the sample can be removed from the UHV chamber to perform further measurements (see section 4.4.2). During the shut down process of the cluster source the shutter is closed in order to ensure no more clusters are hitting the mixer. It is kept rotating during the shutdown and UV/Vis measurements are continued in order to control the cluster plasmon. The red spectrum marks the extinction 10 minutes after the deposition is stopped. The extinction increases for both samples, which means that the mixing process continues after deposition since not all clusters deposited on the thin ionic liquid film on the mixer surface are immediately mixed into the volume in the tub during a few rotations. The timescale of 10 minutes, until the mixing process is finished, is independent of the cluster deposition rate for all experiments performed with C_4MIM PF_6. This value is in accordance with measurements performed by Z. Batsoev [Bat14] (see section 3.3), that revealed that at the optimal rotation frequency of $1\,\text{Hz}$ it takes 10 minutes to mix the ink, that was spread on the mixer surface, into the volume. The extinction increase after deposition is larger for the higher deposition rate, meaning that a larger amount of clusters is mixed into the volume. For sample *DO59* the extinction increases from 0.57 to 0.58, while it increases for sample *DO60* from 1.8 to 2.0.

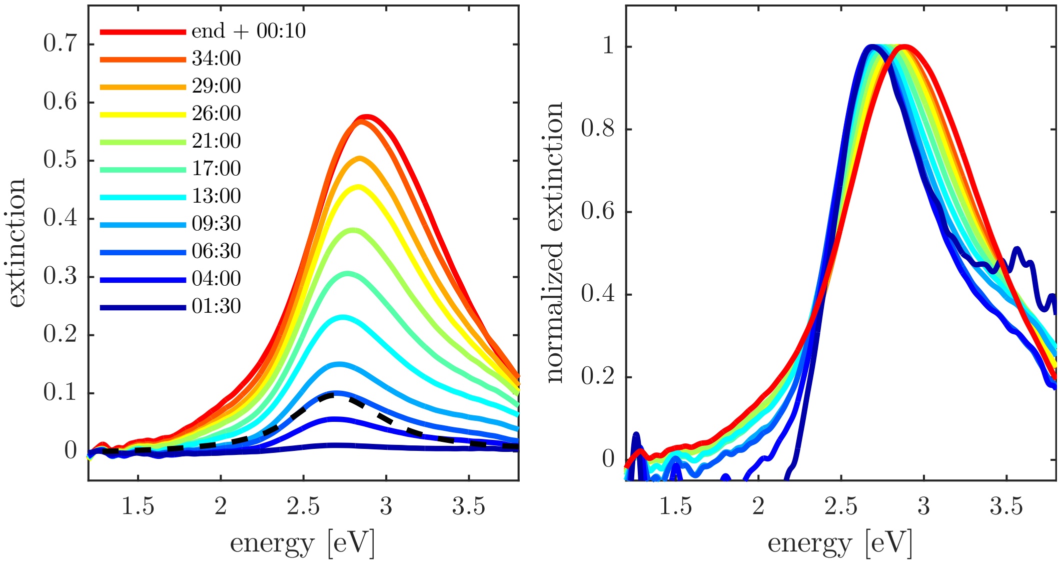

(a) Deposition of sample DO59. The deposition took 34 minutes with a cluster deposition rate of 0.075 Å/s. Parameters for theoretical spectrum (dashed line): $A = 0.75$ and $n = 1.95$.

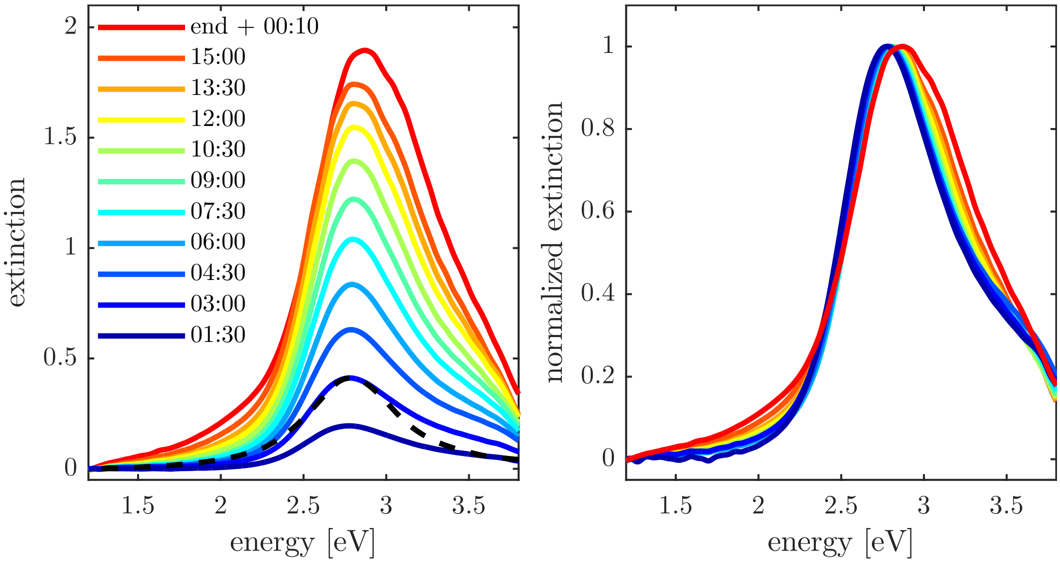

(b) Deposition of sample DO60. The deposition took 16 minutes with a cluster deposition rate of 0.325 Å/s. Parameters for theoretical spectrum (dashed line): $A = 0.75$ and $n = 1.84$.

Figure 5.3: Effect of the deposition rate on cluster plasmon resonance peak position and shape with otherwise identical deposition conditions.

A series of experiments has been carried out to investigate the influence of the cluster deposition rate on the resulting cluster plasmon resonance cluster deposition rate. Figure 5.4 shows the dependence of the peak position at the beginning of the deposition on the cluster deposition rate (black crosses). There is a recognizable correlation to peak positions at higher energies for higher cluster deposition rates. If there was no change of the local structure of the refractive index, the peak position for 2 nm Ag clusters in C_4MIM PF_6 would be expected to be at 3.16 eV (equation (4.39)), marked by the red line.

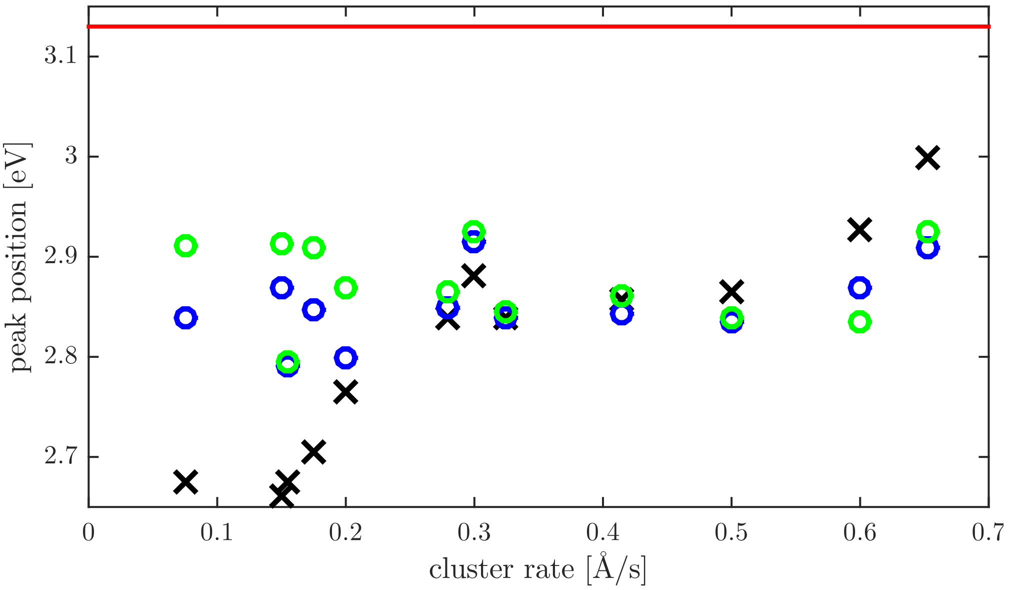

Figure 5.4: Dependence of the peak position at the beginning of the deposition (black) on the cluster deposition rate. The blue circles give the peak position at the time when 100 μg clusters have been deposited into the IL, while the green dots represent the position of the cluster plasmon at its final position after the mixing process in the mixer is completed. The red line indicates the peak position 3.16 eV expected for a cluster embedded in C_4MIM PF_6 without any interactions.

The trend in figure 5.4 indicates that the lower the cluster deposition rate is (meaning that less clusters per time are hitting the thin ionic liquid film on the surface of the mixer), the larger is the difference between the refractive index of pure ionic liquid and "local" refractive index. The peak position of the cluster plasmon does not necessarily stay constant (as shown in figure 5.1) during the entire deposition. This behavior is visualized by the blue circles in figure 5.4. They mark the cluster plasmon position at the end of the deposition for the corresponding cluster deposition rate. At this point it is important to emphasize that the conclusions drawn from the cluster plasmon peak position on the local refractive index are only valid as long as the sample only contains those separated clusters. As soon as changes concerning cluster plasmon shape or position (for example caused by electromagnetic coupling seen in section 4.3.4) appear in the spectra, they cannot be described using the theoretical spectrum upscaled by multiplication with a scaling factor. Hence separated 2 nm clusters cannot necessarily be presumed anymore. Nevertheless, the peak shift during deposition is discussed in the following. For cluster deposition rates between 0.3 Å/s and 0.5 Å/s the peak shift is the smallest. For smaller rates the peak shift is larger. Interestingly, a peak shift to lower energies is observed for cluster deposition cluster deposition rates above 0.5 Å/s.

The green circles mark the cluster plasmon position after cluster source shutdown, when the sample can be removed from the UHV chamber. As indicated in figure 5.4 this peak shift is very large for several deposition rates compared to the peak position at the beginning of the deposition. After the mixing process is completed the cluster plasmon peak positions are between 2.79 eV and 2.93 eV, independent on the used cluster deposition rate.

Besides the shift of the resonance maximum also different FWHM have been observed as already indicated in figure 5.3. Figure 5.5 shows the dependence of the FWHM of the cluster plasmon on the deposition rate. The black crosses indicate the FWHM immediately after the deposition was started. In contrast to figure 5.4 no clear trend can be observed. For deposition rates between 0.075 Å/s and 0.5 Å/s the FWHM is between 0.55 eV and 0.75 eV, while it increases for higher cluster deposition rates to 1.04 eV. Generally, a larger FWHM is related with a sample in which the clusters already started to couple electromagnetically.

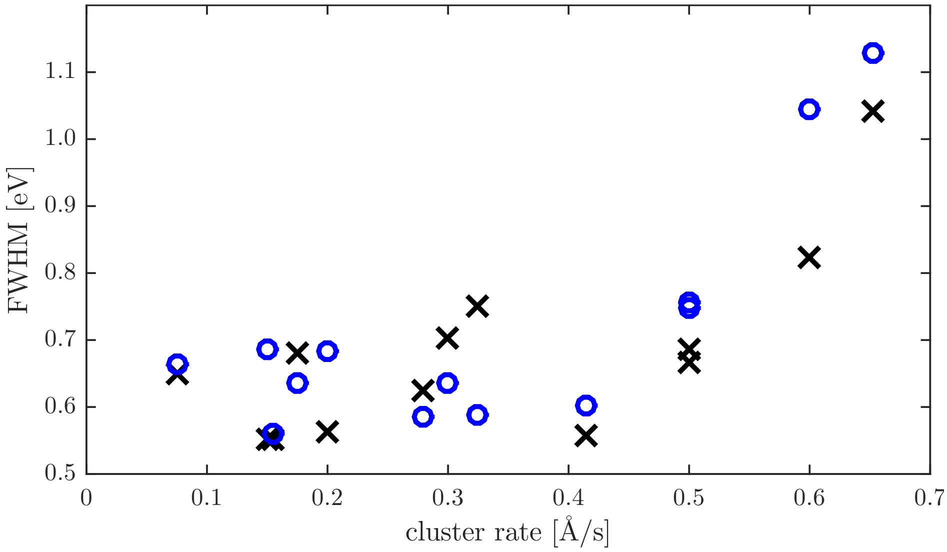

Figure 5.5: Dependence of the FWHM on the cluster deposition rate. The black crosses indicate the FWHM of the cluster plasmon immediately after the deposition is started. The blue circles give the FWHM at the time when 100 µg clusters have been deposited into the IL.

The blue cycles mark the FWHM at the time when 100 µg of clusters have been deposited into the ionic liquid. Hence 100 µg is an arbitrarily chosen number, but a fixed amount (calculated with equation (3.13)) of material needs to be chosen to compare the experiments to each other. For a deposition rate of 0.075 Å/s it takes 30 minutes deposition time to deposit 100 µg clusters into the IL, while it only takes roughly 4 minutes to reach to same amount of cluster material for deposition rates of 0.65 Å/s. In some experiments the FWHM decreases during the experiment, but for cluster deposition rates larger as 0.5 Å/s an increase of the FWHM is observed. Obviously such large cluster deposition rates are too high and the mixer is not able to mix the clusters deposited onto its surface fast enough to keep them separated in the volume. Therefore a cluster deposition rate below 0.5 Å/s should be chosen to ensure the mixture of the separated clusters.

5.1.3 Influence of Deposition Temperature

In a control experiment the influence of temperature during deposition is investigated under identical experimental conditions used in the experiment shown in figure 5.1. Again a cluster deposition rate of 0.3 Å/s was used. The deposition time was 17 minutes. During deposition the IL is heated to 80 °C, which lowers the viscosity of the IL by a factor of ten [Har05] (compare to figure 5.15).

The *in-situ* spectra are shown in figure 5.6 in comparison to the experiment performed at room temperature (dashed lines), that was already introduced in section 5.1.1. In the heated ionic liquid the cluster resonance maximum shifts significantly to 3.1 eV, while the room temperature ionic liquid sample shows a peak position at 2.9 eV. The deviations at low energies (1.4 eV - 2 eV) are caused by a mechanical drift in the optical setup (see chapter 3.3, initial mixer drive), that has higher impact at low extinctions.

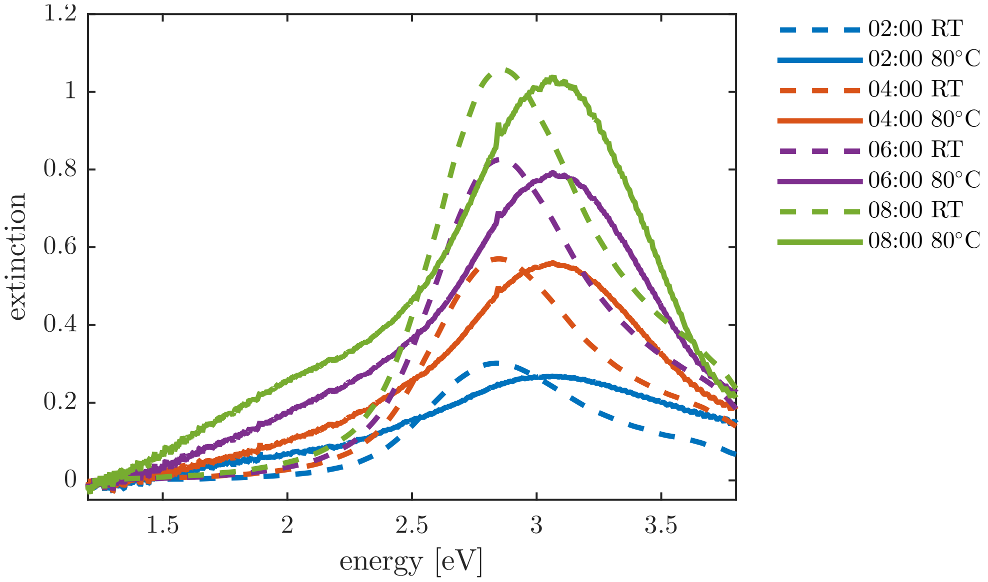

Figure 5.6: Cluster deposition into a heated ionic liquid (solid lines) compared to a deposition performed at room temperature (dashed lines). Except for the temperature both experiments were underlying the same conditions.

Again, a theoretical spectrum to describe the data, is calculated. The parameters were set to $2R = 2\,\text{nm}$, $A = 1.01$ and $n = 1.48$. The Abbe refractometer also allows to control the temperature of the measured liquid; by heating C_4MIM PF_6 from 20 °C to 80 °C the refractive index decreases from 1.418 to 1.404. However, this shift of $\Delta n_{\text{Abbe}} = 0.014$ due to the increased temperature is too small to explain the large shift of $\Delta n_{\text{exp}} = 0.27$ seen in the experimental results. Concluding, also temperature has an influence on the structure of the ionic protective layer, which seems to be perturbed at higher temperatures. This can also be seen in the larger FWHM (1.03 eV compared to 0.82 eV for the room temperature experiment).

Since the value of the local refractive index of 1.48 is closer to the refractive index 1.404 of pure heated ionic liquid, this is a hint on the reduced interaction between the compounds of the ionic liquids and the clusters. This result was integrated into the publication concerning the first results for the deposition of clusters into RTIL [Eng16]. Similar behavior has been seen in studies of the potential dependence of the differential capacitance/potential curves of imidazolium-based ionic liquids at a carbon cathode. The ions were arranged in a double layer that diminishes as temperature increases [Loc08].

Up to now only a few temperature-dependent studies concerning nanoparticles in ionic liquids are available. The group of Hatakeyama *et al.* carried out small angle X-ray scattering (SAXS) studies of sputtered Au nanoparticles [Hat10]. They observed drastic temperature-dependent effects on the nanoparticle formation caused by altered diffusive velocities resulting from the changes in the viscosity. Therefore heat treatment indirectly enables the control of nanoparticle size [Sug15]. However, influences on the refractive index of an IL have not been reported up to now. The topic of temperature dependence on sample structure and stability is in detail discussed in section 5.2.2.

5.1.4 Maximum Disposable Amount of Clusters

In the ideal case the sample contains as much separated clusters as possible. Separated particles can be assumed as long as the cluster plasmon does not change its shape. This can be verified by multiplying the first recorded spectrum with a factor; if spectra taken later during deposition are congruent with the multiplied spectrum, the clusters in the sample can be assumed as separated. The experiments discussed in the previous sections have been finished containing approximately 10 µg/ml separated clusters. However, there is an upper limit for the maximum amount of clusters that can be deposited separately into 15 ml ionic liquid. If this amount is exceeded, the clusters aggregate already during deposition.

Figure 5.7 shows the *in-situ* spectra of a experiment *DO54*, that was performed with a cluster deposition rate of 0.5 Å/s for 34 minutes, resulting in a cluster concentration of 83.7 µg/ml. The optical adjustment was not ideal and causes the high noise in the spectra with a high extinction. Also the dip at about 2.25 eV is an experimental artifact forming for long deposition time. During deposition the FWHM of the cluster plasmon increases.

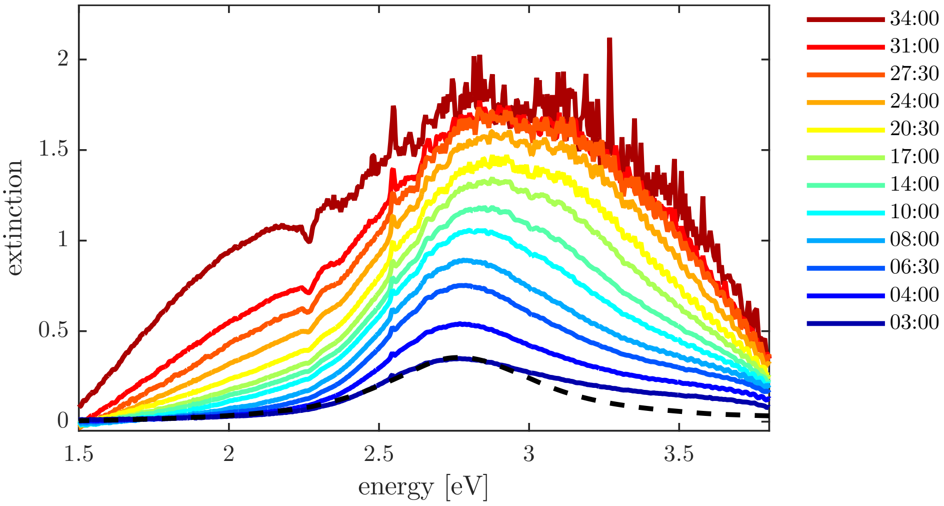

Figure 5.7: Aggregation of sample *DO54* during deposition. After deposition it contains 83.7 µg/ml. The legend denotes the duration of the deposition in *MM:SS*

Separated clusters can be assumed for the first 8 minutes of deposition. According to equation (3.13) after 8 minutes 11.8 µg/ml Ag clusters have been deposited into the IL. This value is in accordance with the concentrations produced in the previous experiments.

The left flank begins to flatten as more clusters are deposited into the IL, resulting in a larger FWHM. An increased extinction at energies below 2.5 eV is observed together with the development of a second point of inflection. After 30 minutes of deposition there is a second peak approximately at 2.2 eV. Comparing these spectra to the ones calculated for different forms of aggregates introduced in section 4.3.4, this shape is typical for linear chains of clusters as shown in figure 4.12. The broadening of the initial single cluster resonance after 8 minutes can be explained by the mentioned superimposition of the spectra of already aggregated and still separated clusters in the sample. As the cluster deposition continues, the features at low energies found in the linear chain spectra become even more pronounced. Simultaneously the extinction of the single cluster resonance at approximately 2.80 eV increases up to 27.5 minutes (orange spectrum) deposition time. Afterwards only the extinction at lower energies continues to increase, meaning that the ratio of separated clusters in the sample decreases.

Note that the GMT calculations in section 4.3.4 have been performed using $A = 1$ and $n = 1.75$, while for the description of sample *DO54* $A = 0.7$ and $n = 1.86$ are chosen (dashed black line in figure 5.7). Therefore only qualitative comparisons are possible.

After deposition the sample is removed from the UVH chamber. It does not show the typical yellow color found for samples containing separated clusters, but sample *DO54* has turned dark gray due to the high amount of aggregated clusters.

5.1.5 Conclusion

A large number of cluster depositions has been performed in order to characterize the samples *in-situ* and to investigate the influence of the cluster deposition rate on position and shape of the cluster plasmon resonance. For all discussed results the ionic liquid C_4MIM PF_6 was used. It turns out that there is a trend for peak positions at higher energies for higher cluster deposition rates. Depending on the cluster deposition rate the peak position can shift during deposition.

The presented experiments reveal an ideal deposition rate between 0.2 Å/s and 0.4 Å/s. For these rates the cluster plasmon resonance has a maximum at $\approx$ 2.86 eV. The maximum is actually expected to be at 3.16 eV for non-interacting 2 nm Ag clusters in C_4MIM PF_6. Thus, an interaction between clusters and and ionic liquid can be observed in the *in-situ* measurements. An alteration of the local refractive index surrounding the cluster, which is due to a stabilizing cation layer around the clusters, seems probable.

Higher deposition rates result in an increase FWHM of the cluster plasmon, which can be explained by aggregating clusters. The reason might be that the mixer cannot move fast enough to avoid cluster-cluster interaction already at the mixer surface. Lower deposition rates are essentially possible for the production of samples containing separated clusters, however it lasts a long time (up to 30 minutes) to obtain high concentrated samples. In principle THECLA provides a stable cluster beam up to one hour, but during those long deposition times aggregation of the clusters inside the tub cannot be excluded. This will in detail be discussed in section 5.2.4.

It takes approximately 10 minutes until the clusters deposited onto the thin ionic liquid film of the mixer surface are completely mixed. Besides an increase of extinction, which is due to the increasing amount of clusters being mixed into the volume, also a further peak shift even after the deposition was finished is observed. After those 10 minutes the cluster plasmon peak is between $2.79\,\mathrm{eV}$ and $2.93\,\mathrm{eV}$, independent of the cluster deposition rate, but due to rate dependent aggregation separated clusters can only be obtained using cluster deposition rates between $0.2\,\mathrm{\AA/s}$ and $0.4\,\mathrm{\AA/s}$.

However, it is difficult to directly obtain an explanation the observed phenomena since the peak position can be influenced by opposed processes. On the one hand it is possible that different cluster deposition rates lead to different interactions with the embedded clusters, on the other hand it would be conceivable that THECLA produces different cluster sizes at different cluster deposition rates. But as already discussed in section 4.3.3, tremendous differences in the cluster size would be necessary to see the measured differences in the cluster plasmon resonance positions. Furthermore, experiments with pressures up to 10^{-3} mbar in the measurement chamber of THECLA revealed that the optical spectra of the free beam do not change compared to those performed with lower pressure [Höv95]. Clusters smaller than 1 nm or silver atoms would be scattered off the cluster beam by impacts with surrounding gas molecules. Since the measured optical spectra do not change for different pressures in the measurement chamber, the presence of a significant amount of very small clusters or silver atoms inside the cluster beam can be excluded.

It could be shown, that using an appropriate cluster deposition rate enables to produce a sample containing separated Ag clusters with a concentration up to $\approx 10\,\mu\mathrm{g/ml}$. Above this threshold the clusters already aggregate during deposition.

5.2 Sample Stability

Besides sample production also sample stability is of crucial importance for further characterization. For both synthesis and physical deposition processes literature reports longterm stable samples. However, as mentioned in the introduction (see section 2.3) for those production methods the processes of nanoparticle formation and aggregation are superimposed [Van11]. Thus samples are referred to stable as long as there is a kinetic equilibrium between nanoparticle formation and aggregation. These processes cancel out each other, resulting in apparently stable samples with no changes in the UV/Vis absorption spectra.

Our approach of using preformed, separated clusters avoids the difficulty of defining a "stable" sample since no nanoparticle formation process is taking place. Every detected change in the sample can be assigned to a cluster-cluster interaction and thus the beginning of the aggregation process.

There are several ways to assess the stability of clusters in ionic liquids. The easiest and most intuitive way is to visually observe the sample color and possible sedimentation. Immediately after deposition the sample shows an intense yellow color due to the cluster plasmon resonance, while aggregated samples become light gray and turbid.

Another common approach is to use transmission electron microscopy (TEM) images to gain information about size, size distribution and structure of cluster aggregates. However, for TEM grid preparation the solution phase clusters are applied onto carbon-coated grids. The solvent is evaporated afterwards, which is unfeasible for ionic liquids due to their nonexistent volatility. To produce TEM samples with ILs as solvents, the IL/cluster mixture has to be diluted with methanol, which is evaporated after grid preparation. This process may falsify the TEM results due to uncontrollable aggregation processes [Das10; Sch07], therefore no TEM images have been studied during this thesis.

However, *in-situ* and *ex-situ* UV/Vis absorption spectroscopy can give valid information as discussed in the following section. Experiments revealed that storing the sample at lower temperatures can dramatically increase sample stability due to the strong dependence of ionic liquid viscosity on the temperature. In a next step the influence of water (e.g. due to the contact of the sample with the ambient air) on the sample stability will be investigated.

5.2.1 Aggregation at Room Temperature

To study the sample stability in detail 133 µg of Ag clusters were deposited into 15 ml ionic liquid. The deposition took 15 minutes with a deposition rate of 0.2 Å/s. The corresponding spectra of *DO46* recorded *in-situ* are shown in figure 5.8. The black dashed lines again indicate the spectrum for separated 2 nm Ag clusters. The parameters $n = 1.9$ and $A = 0.75$ were chosen to fit the spectrum (dashed black lines) as described in section 5.1.1.

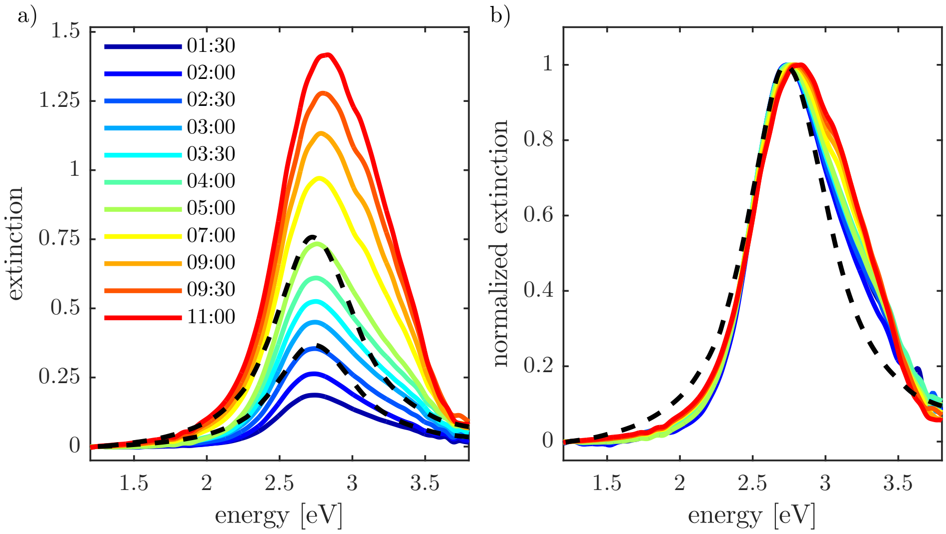

Figure 5.8: a) Spectra taken during deposition of sample *DO46*. The time is specified in *MM:SS*. In b) the spectra are normalized equal to the maximum extinction.

After deposition and shutdown of the cluster source a plate valve is closed to separate the measurement chamber from the cryo pumping stage. The measurement chamber can be vented in order to remove the sample from the UHV chamber. The sample changed its color from transparent into a strong yellow. The change of the color is caused by the strong Ag cluster plasmon that emerged during deposition. For the *ex-situ* UV/Vis absorption measurement the sample is filled into a silica glass cuvette with 1 cm path length. Pure ionic liquid, which also has been placed in the UVH chamber during deposition to underlie the same degassing process, is filled in another cuvette and used as a reference. For the UV/Vis absorption measurements a cuvette holder with adjustable lenses is used. The extinction is again calculated using equation (4.49) and the *ex-situ* UV/Vis spectra recorded up to 24 hours after deposition are shown in figure 5.9.

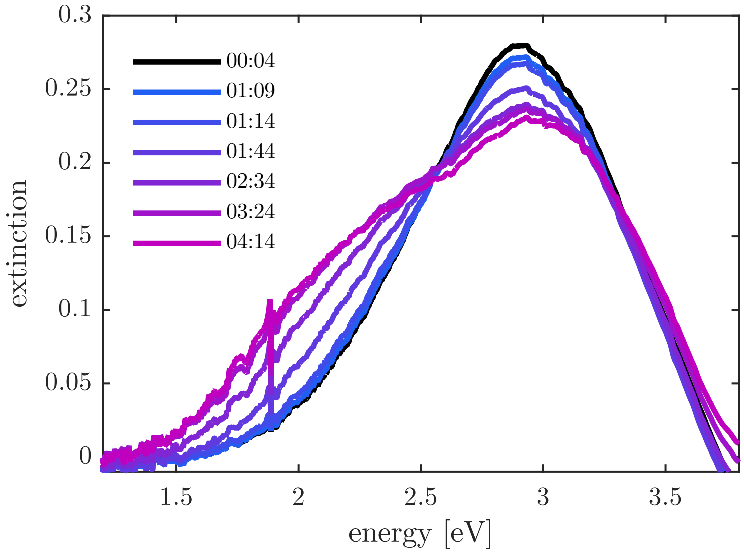

Figure 5.9: *Ex-situ* spectra of the sample *DO46* recorded up to 24 hours after deposition in a 1 cm cuvette. The timestamps indicate the time in *HH:MM* after deposition.

Note that the extinction spectra of *in-situ* and *ex-situ* measurements differ roughly by a factor of 6, which is due to the different optical path length d (6 cm in the mixer and 1 cm in the cuvette) and is taken into account in equation (4.47). In the course of time the maximum extinction decreases within 4 hours, while simultaneously the extinction at lower energies increases. At first the extinction at 2.9 eV decreases, while the FWHM remains constant. After approx. 90 minutes the entire peaks appear broadened with an increased extinction below 2.5 eV. This behavior recalls the spectra obtained by the Generalized Mie Theory based calculations of cluster aggregates (section 4.3.4), which will be in detail discussed in the following. After 24 hours no plasmon is identifiable anymore, which is confirmed by the visual impression: the color of the sample has turned into transparent gray. This state will be denoted as an aggregated sample throughout the following chapter.

5.2.2 Temperature-Dependent Aggregation

For further sample characterization (e.g. transfer of the samples to a synchrotron) it is inevitable to produce long-term stable samples. In this thesis the samples are cooled down in order to decrease the viscosity of the ionic liquid, which is expected to slow down or suppress the Brownian motion inside the sample.

Temperature-Dependent UV/Vis Absorption Spectra

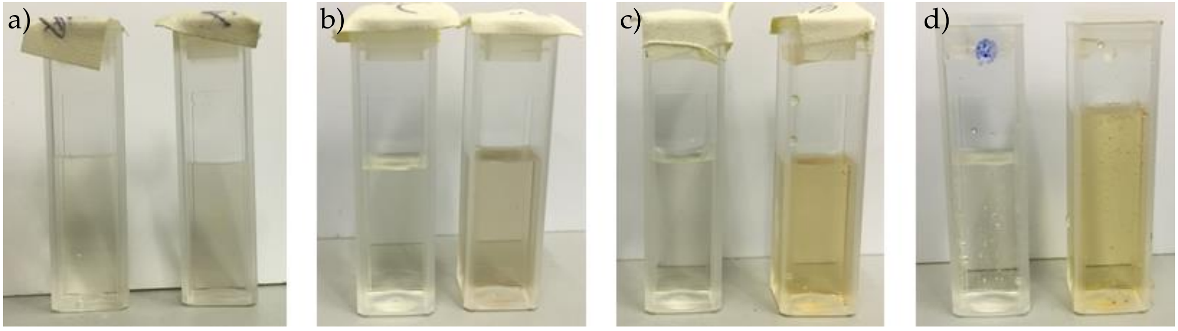

Figure 5.10: Visual impression of the *DO46* samples stored at a) at room temperature, b) in a fridge at 280 K, c) in a freezer at 250 K and d) in liquid nitrogen at 80 K, always compared to a cuvette with empty IL (left side in each picture). Each picture was taken 24 hours after deposition.

To investigate the dependence of the storage temperature on the sample stability the sample *DO46* is split up into four cuvettes. They are stored at different temperatures: at room temperature (293 K), in a refrigerator (280 K), a freezer (250 K) and in liquid nitrogen (80 K). Figure 5.10 shows pictures of the samples stored at different temperatures, all taken 24 hours after deposition in comparison to a cuvette with pure ionic liquid. A temperature-dependent development is clearly visible. As already mentioned above, the sample stored at room temperature is not yellow anymore. If any, a slightly gray color can be surmised. However, no macroscopic sediment can be found at the bottom of the cuvette. The colder the storage temperature is, the more intense yellow color of the samples can be observed. The color of the sample stored in liquid nitrogen looks as intense as the one immediately after deposition. However, quantized measurements are necessary to support this optical impression.

To perform UV/Vis absorption measurements, the samples need to be warmed to room temperature. This is particularly necessary for measurements of samples frozen in the fridge and in liquid nitrogen to enable light transmission through the cuvette. Therefore the cuvettes are blown on with nitrogen through the aluminum lightshield of the sample holder in order to avoid fogging or the formation of condensed water at the surfaces of the cuvettes.

Figure 5.11 summarizes the aggregation process for all four considered storage temperatures. Note, that the spectra taken for different temperatures have different timestamps because the aggregation process is significantly slowed down for cold storage temperatures as expected from the visual impression of the stored cuvettes. Therefore it was possible to perform UV/Vis measurements up to three months after deposition.

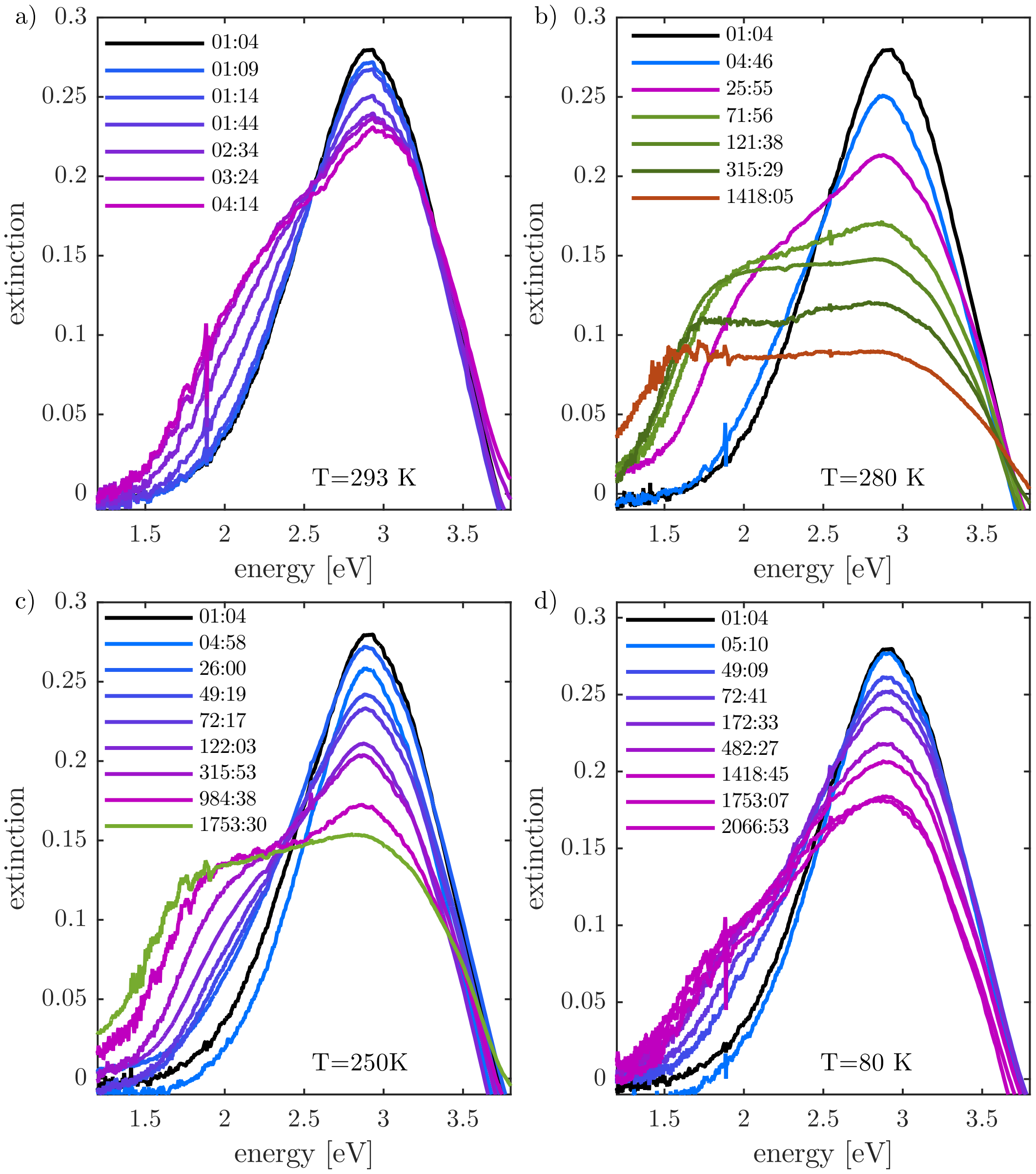

Figure 5.11: Influence of storage temperature on the aggregation of sample *DO46*, each compared to the measurement immediately after deposition (black line). The sample was stored a) at room temperature, b) in a refrigerator, c) in a freezer and d) in liquid nitrogen. All legend entries denote the time (*HH:MM*) that has passed after the sample deposition has been stopped. See text for the meaning of the colors of the spectra.

As already discussed for a sample stored at room temperature also shown in figure 5.11a) the maximum extinction decreases fast on a timescale of barely an hour from 0.28 to 0.25. After 90 minutes the plasmon starts to change its shape, becoming significantly broadened with an increased extinction below 2.5 eV. By altering the storage temperature the time scales of the plasmon decay become longer.

Figure 5.11b) shows the spectra of the storage in a refrigerator at 280K. Here the sample aggregation is remarkably decelerated and can be observed on a timescale of several weeks. For example the decrease from an extinction of 0.28 down to 0.25 is detected after almost five hours, which is a factor of five slower than found in the room temperature measurement. After almost 26 hours the maximum extinction has decreased to 0.2, together with an increased extinction at lower energies ($< 2.5\,\mathrm{eV}$). The spectrum now shows a second point of inflection at 1.9 eV. In the course of the aggregation process the maximum extinction further decreases within 20 days until no plasmon peak can be detected anymore. However, the extinction is 0.075 in the complete energetic range from 1.5 to 3 eV.

For the storage in the freezer (figure 5.11c)) the same change of the cluster plasmon resonance shape is observed. However, the last measurement taken 1753 hours after deposition looks similar to the spectrum of the storage in the refrigerator taken 172 hours after deposition. This different time scale again shows the delay of aggregation. Further states of aggregation (like the entire decrease of extinction down to 0.075) was not observed on the considered time scale for sample storage in the freezer.

The aggregation process for sample storage in liquid nitrogen is even more delayed. However, the aggregation shown in figure 5.11d) is likely caused by the the necessary warming before each measurement, which takes 15 to 20 minutes for each measurement. When summing up the time the sample was exposed to room temperature to warm it up every time before measurement is approximately of the magnitude compared to the room temperature spectra (several hours). A control experiment showed that by keeping the sample stored in liquid nitrogen it completely stops any changes of the cluster plasmon resonance even on timescales of several months (not shown here). This effect of aggregation during warming also occurs for the measurement of the sample stored in a freezer. Although this warming up time is much shorter compared to the time needed to warm up the liquid nitrogen sample, this effect needs to be taken into account when evaluating the timescale of aggregation.

Considering the position of maximum extinction, one recognizes a small shift from 2.9 eV to 2.85 eV after 48 hours or 984 hours for storage in the refrigerator and the freezer, respectively. A shift to smaller energies has also been seen in the calculations performed for Ag dimers and chains, but it is much larger in the calculations (cf. section 4.3.4). It must be kept in mind, that the experimental results always average over a large sample volume. As the aggregation occurs slowly, there are always separated and aggregated clusters and averaging leads to a weakening of the peak shift.

Figure 5.12 shows the decrease of the maximum cluster plasmon extinction. $\Delta\,extinction$ gives the difference between the maximum extinction of the considered sample and the initial extinction of 0.28 given by the black curve in figure 5.11 recorded immediately after deposition. Note that the abscissa is logarithmic since the time scale of the cold samples is much longer than the room temperature time scale. Except for the last data point of the room temperature sample a linear correlation can be seen for the room temperature and the refrigerator sample. As already discussed, the time scale of the freezer and liquid nitrogen cooled samples have to be handled with caution since the aggregation speed is overestimated due to the warming before each measurement. This becomes also visible in figure 5.12. The gradient between the first two data points is much lower than for the data points taken at a later time.

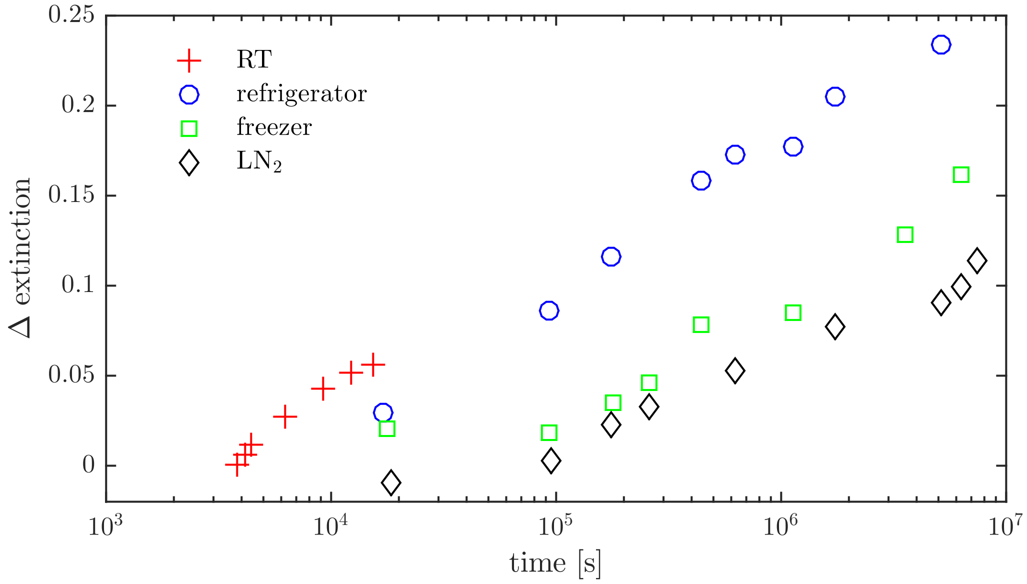

Figure 5.12: Visualization of the decrease of the maximum extinction depending on the time passed after cluster production. Δ *extinction* denotes the difference between the initial extinction 0.28 and the actual decreased extinction.

Analysis of the Aggregation Kinetics

Based on figure 5.11 different phases of aggregation can be defined. These definitions are somewhat arbitrary, but enable to further compare those states of aggregation for the different storage temperatures. Five phases are defined based on the spectra recorded for the refrigerator (figure 5.11b)). The black color always indicates the first spectrum at room temperature after removing the sample from the UHV chamber. In the following, this will be denoted as *phase 1*. In *phase 2* (blue) the plasmon shape is similar to *phase 1*, but the maximum extinction decreases. The spectra of *phase 3* (violet) show a second point of inflection at lower energies between 1.5 and 2 eV. The maximum extinction continues to drop, resulting in a very broad peak between 1.5 and 3 eV in *phase 4* (green). In the last phase (*phase 5*, red) the overall extinction decreases until no plasmon is detectable anymore. The first four phases are compared to each other in figure 5.13 together with the times needed until each phase occurs for the storage temperatures room temperature (solid lines), refrigerator (dashed lines) and freezer (dotted lines).

In the room temperature spectra only the development of the first three phases as well as the last can be seen; after 24 hours *phase 4* was not measured. Lowering the storage temperature delays the occurrence of the next phases. In order to gain information about the aggregation dynamics the Arrhenius equation is used, which describes the temperature dependence of reaction rates:

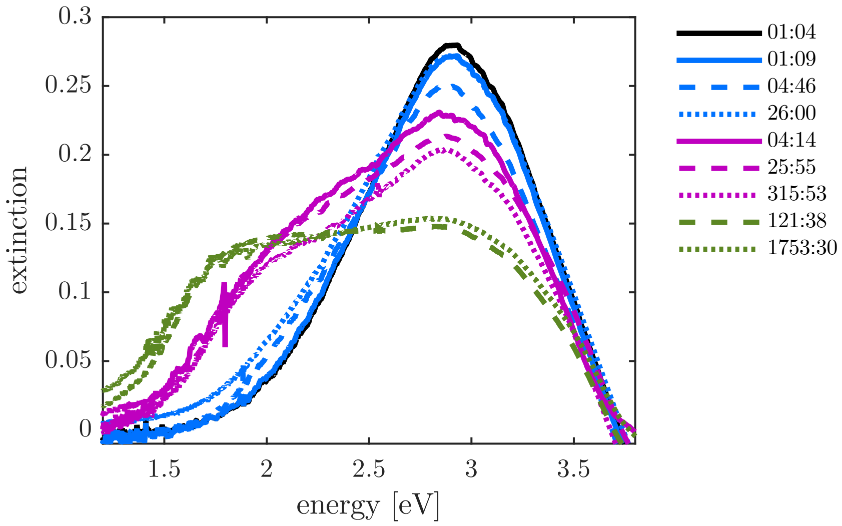

Figure 5.13: Comparison between the first four phases of aggregation for different storage temperatures (solid lines: RT, dashed lines: refrigerator, dotted line: freezer). All legend entries denote the time (*HH:MM*) that has passed after sample production.

$$k = A \cdot \exp\left(-\frac{E_A}{k_B T}\right) \tag{5.1}$$

Here k denotes the rate constant, A a pre-exponential factor, E_A the activation energy, k_B the Boltzmann constant and T the absolute temperature in Kelvin.

Taking the natural logarithm, equation (5.1) yields:

$$\ln(k) = \ln(A) - \frac{E_A}{k_B} \cdot \frac{1}{T} \tag{5.2}$$

$$\ln(t) = \text{const.} + \frac{E_A}{k_B} \cdot \frac{1}{T} \tag{5.3}$$

From equation (5.3) it follows that a plot of $\ln(t)$ versus T^{-1} gives a straight line from which the activation energy can be calculated.

Figure 5.14 shows the Arrhenius plot for the phases 2 and 3 using the data shown in figure 5.13. Note that the temperature scale is interrupted to display the data taken for liquid nitrogen. The data points recorded for the storage in the freezer and in liquid nitrogen are excluded from the Arrhenius fit since aggregation is likely caused by the defrosting that is necessary for UV/Vis measurements as discussed above. Thus for the calculation of the activation energies only gradient of the data points from the room temperature and the fridge measurement is calculated, revealing activation energies of $E_A = 0.773\,\mathrm{eV}$ and $E_A = 0.985\,\mathrm{eV}$ for the phases 2 and 3, respectively.

Although the ions of the ionic liquid are known to form an electric double layer around the clusters (which also was seen in the alteration of the cluster plasmon peak position in section 5.1.1), it is not possible to describe the experimental observations with a model of *interaction limited coagulation* [Eas05], at least for the storage at low temperatures and thus

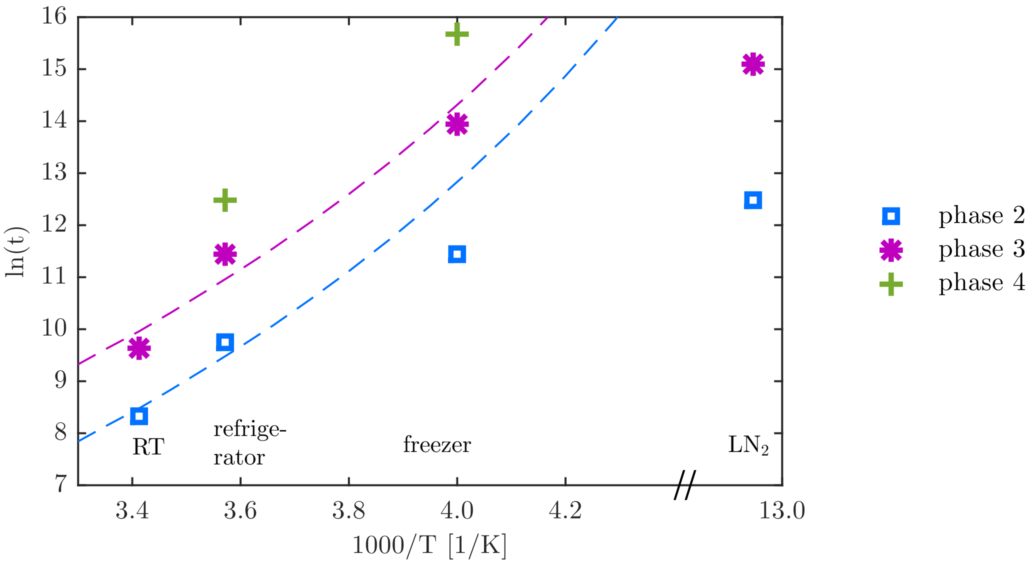

Figure 5.14: Temperature-dependent aggregation kinetics, which can be described using a simple model for rapid diffusion limited coagulation taking into account the temperature dependence of the viscosity of C_4MIM PF6 (see below).

with a highly viscous IL. An alternative model is the *diffusion limited coagulation* [Eas05], which will be described in the following.

The strong temperature dependence of the viscosity of C_4MIM PF_6 is shown in figure 5.15 using the data from Harris [Har05].

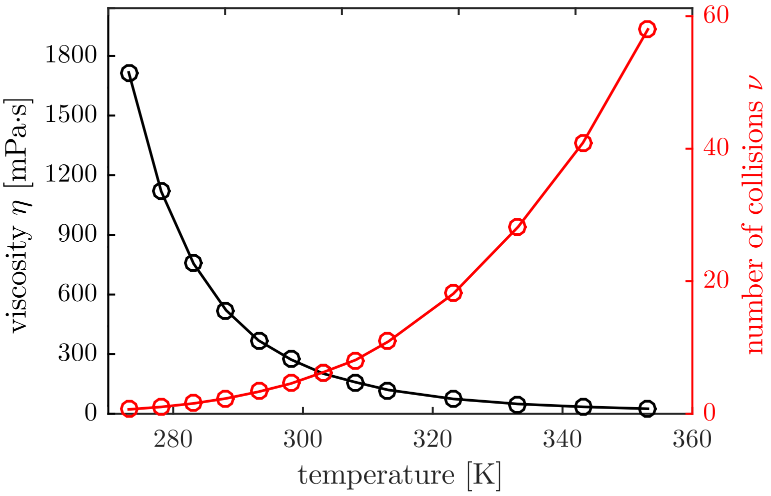

Figure 5.15: Temperature dependence of the viscosity η of C_4MIM PF_6 measured by Harris *et al.* using a falling-body viscometer [Har05] and the related decrease of the number of collisions ν, that a cluster experiences during a time unit according to equation (5.6) for 2 nm clusters.

No value for the viscosity has been measured for lower temperatures than 273 K because of a phase transition into a glassy state (see discussion below). However, the data can be extrapolated using a Vogel-Fulcher-Tammann equation

$$\eta(T) = A \cdot \exp(B/(T - T_0)), \tag{5.4}$$

where $A = 0.06923\,\mathrm{mPa{\cdot}s}$, $B = 1127\,\mathrm{K}$ and $T_0 = 161.8\,\mathrm{K}$ are temperature-independent constants [Har05]. The diffusion coefficient of a particle with radius r is related to the viscosity via the Stokes-Einstein equation

$$D(T) = \frac{k_B \cdot T}{6 \cdot \pi \cdot \eta(T) \cdot r}. \tag{5.5}$$

Due to the relatively high viscosity of C_4MIM PF_6 the diffusion coefficients calculated for clusters with a diameter of 2 nm are very low compared to the values obtained for common solvents with viscosities similar to water [Cri12]. A model of rapid coagulation introduced by Kraynov [Kra11], in which every collision of two nanoparticles immediately results in coagulation and hence in agglomeration, is assumed. Applying the Einstein-Smoluchwski formalism to this model yields the number of collisions ν for one cluster per time unit [Lyk05]:

$$\nu(T) = \frac{k_B \cdot T}{\pi \cdot \eta(T) \cdot r^3} \cdot \phi \tag{5.6}$$

Here ϕ describes the volume fraction of clusters in the IL and can be estimated for the samples investigated in this thesis with a concentration of approx. $10\,\mu\mathrm{g/ml}$:

$$\phi = \frac{V_{\text{cluster}}}{V_{\text{IL}}} \approx \frac{10\,\mu\mathrm{g}/10.49\,\mathrm{g/ml}}{\mathrm{ml}} = 9.5 \cdot 10^{-7} \tag{5.7}$$

Using this model and assuming a temperature independent coagulation probability p as the only free fit parameter, the experimental data can be described with $p_{\text{phase2}} = 1/\left(1.6 \cdot 10^4\right)$ and $p_{\text{phase3}} = 1/\left(7 \cdot 10^4\right)$ as shown in figure 5.14 (dashed lines). Due to the comparably small temperature range the assumption of a temperature independent coagulation probability p is reasonable.

Thus by decreasing the temperature from 293 K to 273 K, according to equation (5.6) the number of collisions ν can be decreased by a factor of approximately 5, which is in accordance with the time delay found for the different phases in figure 5.13. Therefore a clear improvement concerning sample stability is expected for samples that are stored at lower temperatures because the thermal movement of the clusters in the sample is significantly suppressed. Furthermore, those considerations impressively show the advantage of using highly viscous ionic liquids like C_4MIM PF_6 in comparison to commonly used organic solvents, such as tetrahydrofuran (THF). At room temperature THF has a viscosity of $\eta_{\text{THF}} = 0.46\,\mathrm{mPa{\cdot}s}$, which is 800 times smaller than the viscosity of C_4MIM PF_6. The number of cluster collisions is thus decreased analogously.

The aggregation can completely be stopped by storing of the sample in liquid nitrogen. This can be explained by the phase transition behavior of ionic liquids. If the temperature is below the melting point, the ionic liquid is in a solid or quasi-solid (i.e. amorphous glassy state) [Cim09; Tri06]. The phase transition behavior depends on the kind of ionic liquid. Freadlake *et al.* determined the phase transition temperatures of several ionic liquids using differential scanning calorimetry. The heat capacity was measured while cooling the sample from 403 K to 153 K, followed by heating it from 153 C to 403 K at a rate of 10 K/min. They found different behaviors depending on the composition of cation and anion. For C_4MIM PF_6 the liquid is subcooled to a glassy state below $T_g = 197$ K. Upon heating, crystallization occurs at $T_c = 236$ K, followed by melting at $T_m = 284$ K [Fre04]. This behavior is well-known for polymers and other amorphous materials [Wid87; Sup01]. In the glassy state the viscosity is very high [Deb01], which suppresses the Brownian movement according to equation (5.6).

There are only a few studies available investigating the influence of temperature on nanoparticle formation and stabilization in ionic liquids. Hatakeyama *et al.* found a drastic influence of temperature on the resulting size of sputter deposited Au nanoparticles onto C_4MIM BF_4, which also is explained by different diffusive velocities [Hat10]. They found an increase from a small distribution of particles with a diameter of 1 nm produced at room temperature to a broad distribution with a mean of approx. 3.5 nm at 80 °C. However, no longterm measurements concerning sample stability have been performed after the SAXS measurements were finished. Kameyama *et al.* found that a post heat treatment (90 °C) of Au nanoparticles in C_4MIM PF_6 produced by sputtering results in an increase of the particle size [Kam10]. However, further heating (150 °C) results in aggregation of the sample verified by UV/Vis absorption spectroscopy.

In this thesis the reverse effect, i.e. sample stabilization by decreasing the ionic liquid temperature, has been investigated. Besides the different time scales of the aggregation process for different storage temperatures a very important conclusion is that prepared samples of clusters in ionic liquid can be stored in liquid nitrogen for months without risking aggregation of the sample. This allows the production of several longterm stabilized samples, e.g. for a transfer to a synchrotron (see chapter 7) for further characterization and ensures that separated clusters can be measured.

5.2.3 Influence of the Water Content on Sample Stability

Since the early days of ionic liquid research water impurities have always been a big issue. It was found that the amount of absorbed water depends on the anion in the IL [Sed00] as shown in figure 5.16 measured by coulometric Karl-Fischer titration. The solubility of water in ILs decreases with increasing alkyl chain length and the PF_6 anion dissolves less water than BF_4. C_nMIM PF_6 ILs are immiscible with water [Koe05] and form a biphasic system. Therefore they are often referred to as hydrophobic, however actually they are hygroscopic since they absorb moisture from the surrounding air through hydrogen bonding [He15] (see figure 5.16b)). Although C_4MIM PF_6 contains the lowest amount of water absorbed from the air, an absorption of 1% w/w is significant and consequently the question rises whether the absorption of moisture from the ambient air could be responsible for the destabilization of dispersed clusters. This could be a possible explanation of the comparatively fast aggregation of the samples stored at room temperature as discussed in the previous chapter. On the one hand the ionic liquid nanostructure and its properties are directly altered [Sed00], while on the other hand water can penetrate the IL double layer, which leads to an interaction between the water molecules and the clusters themselves [Oli09; Rub08].

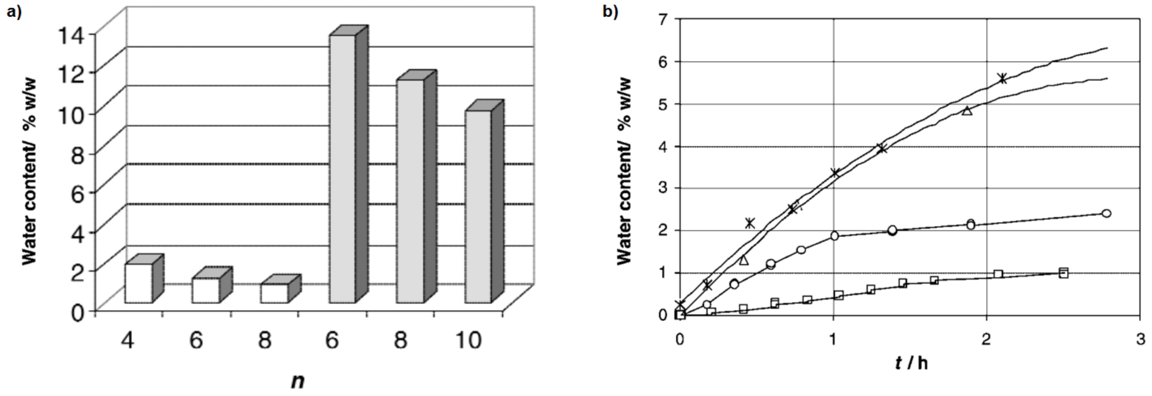

Figure 5.16: a) shows the saturated water content for C_nMIM PF_6 (white) and C_nMIM BF_4 depending on the alkyl chain length. b) shows the hygroscopic behavior of imidazolium based ionic liquids. The water content strongly depends on the anion. The following legend is used: C_8MIM NO_3 (Δ), C_8MIM Cl ($*$), C_4MIM BF_4 ($\bigcirc$), C_4MIM PF_6 ($\square$) [Sed00].

Experiments of gold nanoparticles produced by sputter deposition [Van11] showed a dramatic dependence of the water content of the sample on sample stability. Samples with a higher water content did not only aggregate much faster (as seen in the decrease of the extinction in the UV/Vis absorption spectra), also a shift of the plasmon position to higher wavelengths (518 nm to 585 nm) was observed [Van12].

In order to check how the presence of water influences the sample stability, a control experiment *DO58* was performed varying the water content at the surface of the sample. The cuvettes used for the temperature-dependent measurements discussed in figure 5.11 were sealed with a cap, but not kept under protective gas atmosphere.

The sample *DO58* was produced as usual (degassed for 72 hours under vacuum conditions) with a deposition rate of 0.28 Å/s for 570 s deposition time, resulting in an Ag concentration of 7.87 µg/ml.

After deposition three cuvettes were filled, each one containing 3.5 ml of the prepared cluster sample: the first is stored unsealed at room temperature, the second cuvette is sealed by wrapping the cap with parafilm to exclude the absorption of moisture from the air. 0.5 ml water was filled on top of the ionic liquid into the third cuvette. It is shaken afterwards to increase the water content inside the sample. However, during storage the direct environment of the IL interface is in contact with the water. All cuvettes were stored at room temperature.

Here absorption spectra were recorded one and three hours after deposition and are compared to the absorption spectrum taken immediately after deposition in figure 5.17. All spectra recorded after one and three hours show the typical behavior as observed before: the intensity of the cluster plasmon decreases, while it simultaneously becomes broader with contributions at larger wavelengths. After one hour the maximum extinction decreases

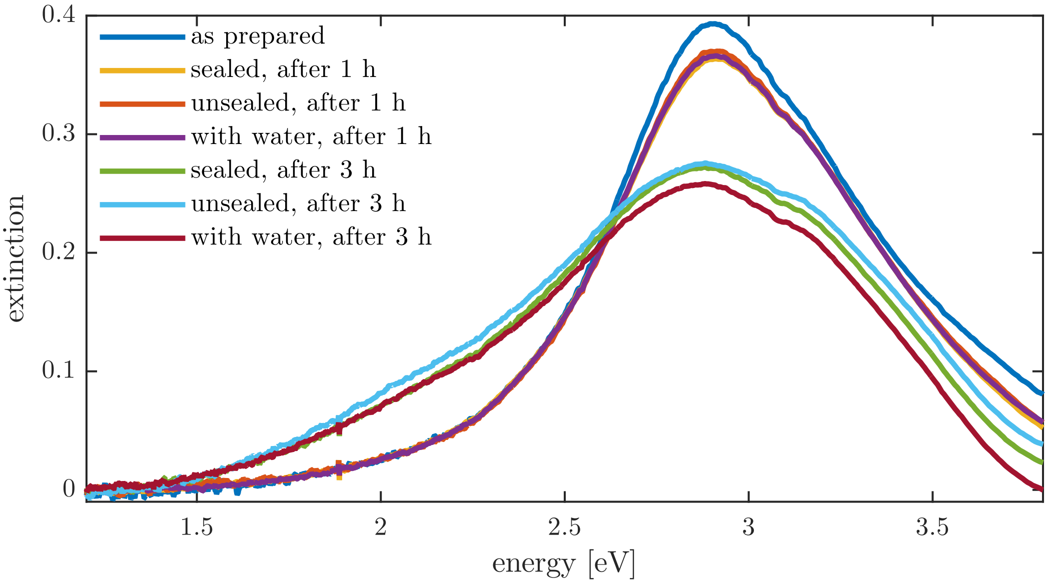

Figure 5.17: Influence of the water content in the direct environment on the sample stability (*DO58*).

from 0.39 to 0.36, while the FWHM slightly increases from 0.66 eV to 0.69 eV. Similar behavior was found in phase 2 discussed in chapter 5.2. After three hours the spectrum of the sample that is protected the most against increasing water content (green line), is the narrowest (FWHM of 1.08 eV). The other spectra are slightly broader (FWHM of 1.15 eV) and the extinction of the IL-water mix (dark red line) is slightly smaller compared to the other samples (0.25, while the two other spectra have a maximum extinction of 0.27). This could possibly be a sign for progressed aggregation, however, all spectra taken three hours after deposition can be assigned to the transition between the phases 2 and 3 of aggregation.

Summing up, this control experiment showed that a variation of the water content in the environment of the sample does not distinctively affect its aggregation behavior. Peak position and shape do not differ for the three samples stored under different conditions. The results found for sputter deposited gold nanoparticles [Van12] could not be reproduced for preformed silver clusters. One possible explanation could be that preformed, embedded clusters are better protected from penetrating water molecules.

5.2.4 Aggregtion Inside THECLA

All previously discussed experiments investigating the cluster aggregation have been performed after taking the sample out of the UHV chamber in a silica glass or PMMA cuvette. Therefore the samples have necessarily been in contact with the ambient air. Although section 5.2.3 did not reveal a measurable effect of different water containing interfaces on sample stability, comparative experiments were performed, in which the sample aggregation is observed under vacuum conditions inside THECLA in order to avoid any exposure of the sample to the ambient air. The deposition of both samples (*DO59* and *DO60*) has already been introduced in figure 5.3, while discussing the impact of different deposition rates on the *in-situ* spectra. After deposition the samples are kept inside the rotating mixer in the vacuum chamber and the UV/Vis absorption measurement is continued. Since the extinction is calculated according to (4.49) using the reference spectrum taken before the deposition was started, this longterm measurement is very sensitive on mechanical drifts of the optical setup explaining systematical deviations.

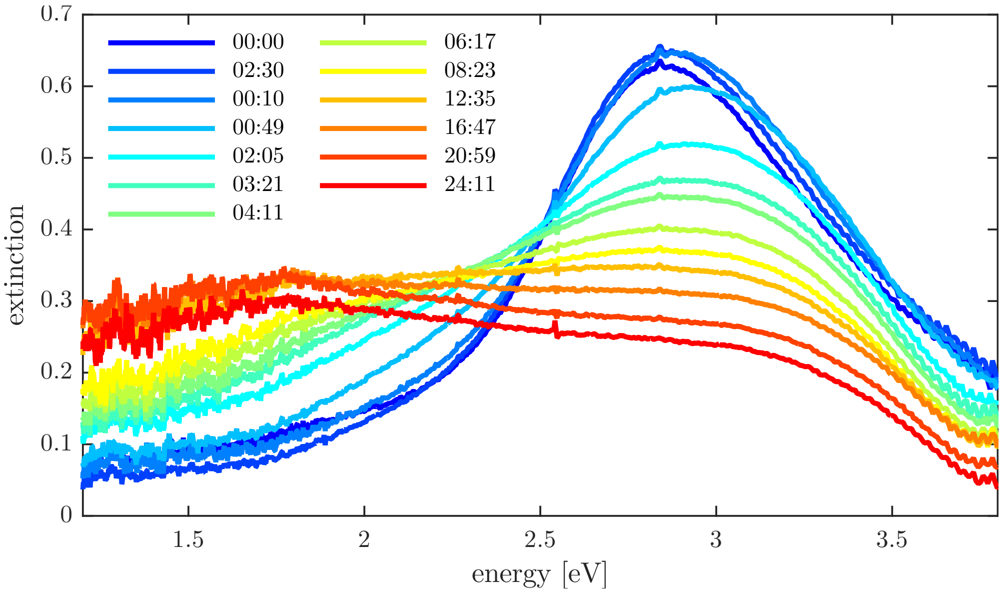

(a) Aggregation of sample DO59. The deposition took 34 minutes with a cluster deposition rate of 0.075 Å/s.

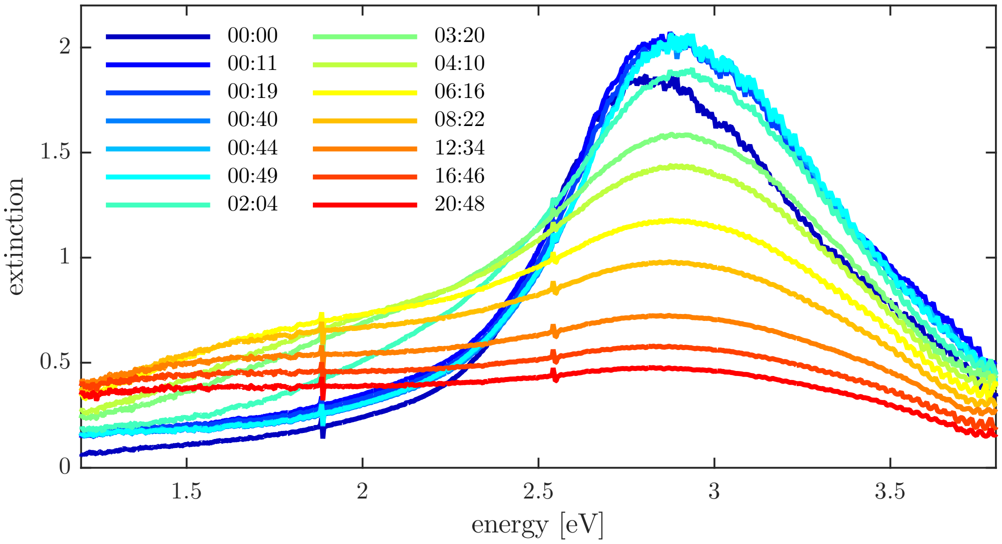

(b) Aggregation of sample DO60. The deposition took 16 minutes with a cluster deposition rate of 0.325 Å/s.

Figure 5.18: Aggregation of two samples produced with different cluster deposition rates. The aggregation took place inside THECLA at a pressure of $8.9 \cdot 10^{-8}$ mbar in order to exclude exposure to the ambient air.

The cluster source is shut down and the argon flow is stopped. Turbo molecular pump and cryo pumping stage ensure a partial pressure in the measurement chamber of $8.9 \cdot 10^{-8}$ mbar. Figure 5.18 shows the development of the cluster plasmon up to almost 24 hours after deposition for both investigated samples *DO59* and *DO60*. The times given in the legend of figure 5.18 denote the time in (*HH:MM*) after the deposition was finished. Note that the extinctions measured in the mixer are higher than those in the 1 cm cuvettes due to the longer optical path length (6 cm in mixer). To compare the results with the *ex-situ* measurements performed before, the extinction has to be divided by six.

In the spectra of both samples a shift of the maximum plasmon extinction and an increase of the extinction can be seen as already discussed in section 5.1.2. For sample *DO59* an increase of the extinction (0.63 to 0.65) is observed within the first 150 s after deposition, followed by a peak shift from 2.84 eV to 2.91 eV within 10 minutes, while the maximum extinction remains constant. During the next 40 minutes a further shift to 2.94 eV together with a beginning decrease of the maximum extinction is observed.

For the sample *DO60* almost the same shift is observed from 2.79 eV to 2.93 eV, however in this case a simultaneous rise of the extinction from 1.81 to 2.05 is much larger. The sample stays stable up to 49 minutes after followed by a decrease of extinction as seen for the sample *DO59*. Simultaneously to the increasing extinction the cluster plasmon resonance shifts from 2.7 eV to 2.8 eV within the first 50 minutes. Within those 38 minutes (from 00:11 to 00:49) the maximum extinction does not decrease. After this time the sample aggregation behavior resembles the observation in figure 5.11b): The maximum extinction decreases steadily together with an increasing extinction at energies between 1.5 and 2 eV.

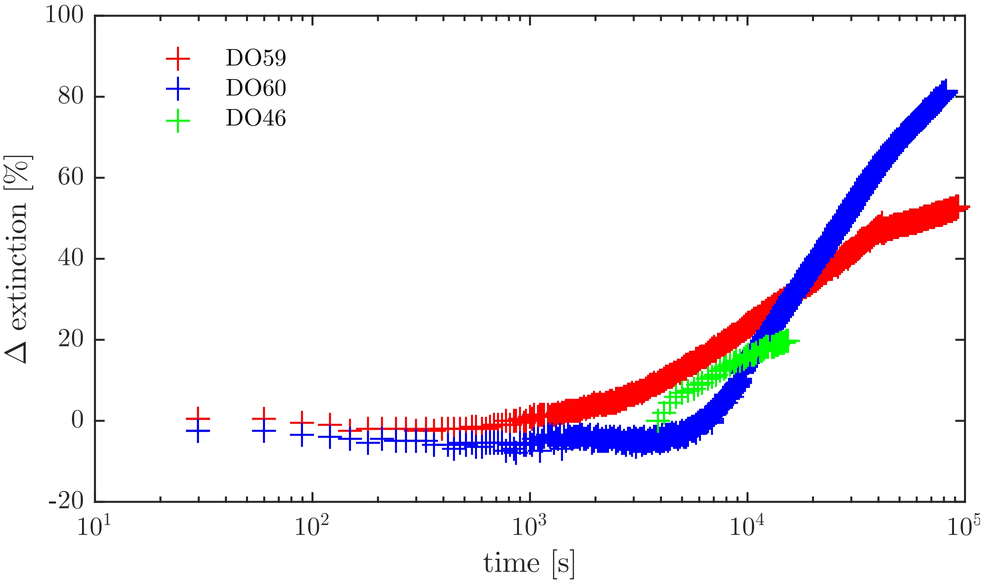

Figure 5.19: Visualization of the relative decrease of the maximum extinction depending on the time passed after cluster production. Δ extinction denotes the difference between the initial extinction and the actual decreased extinction. The data taken *ex-situ* for the aggregation of sample *DO46* are shown for comparison.

The decay of the maximum cluster plasmon extinction is shown in figure 5.19 analogously to figure 5.12. However, since both experiments differ in maximum extinction, the extinction decay Δ *extinction* is expressed in percentage of the initial extinction. The data of sample *DO46* stored in a cuvette at room temperature are also given. The negative values of Δ *extinction* are caused by the increasing extinction after deposition.

The results obtained for sample *DO59* are comparable to those observed for sample *DO46*, whereas sample *DO60* is significantly more stable. As soon as the extinction starts to decrease (approx. 5000 seconds after deposition) the sample aggregates faster than the other two samples.

However, during these experiments the mixer was not stopped. It could be possible that mixing may somehow slow down the aggregation process because the sample is continuously moved, which could affect the particle diffusion. But since the Δ *extinction* of *DO59* and *DO46* do not differ too much from each other, influences of both mixing and the exposure to ambient air, which anyway is necessary for further sample characterization, do not seem to affect the sample aggregation.

5.3 Influence of Cation and Anion on Deposited Silver Clusters

All results presented in chapter 5.1 were obtained from experiments using $C_4MIM\ PF_6$. The *in-situ* experiments revealed that an optimal cluster deposition rate is between 0.2 Å/s and 0.4 Å/s. As already mentioned in section 2.2.4 ionic liquids containing different anions and cation with different alkyl chain lengths have been investigated in literature concerning the stabilization of nanoparticles. However, in this thesis only imidazolium based ionic liquids are investigated due to their proposed ability of long-time stabilization [Ric11].

Figure 5.20 shows transmission data taken for different ionic liquids investigated in this thesis. All samples have been measured with an empty quartz glass cuvette as a reference. Slight changes in the optimal focus of the fiber cable cause deviations of the transmission ($T > 100\%$).

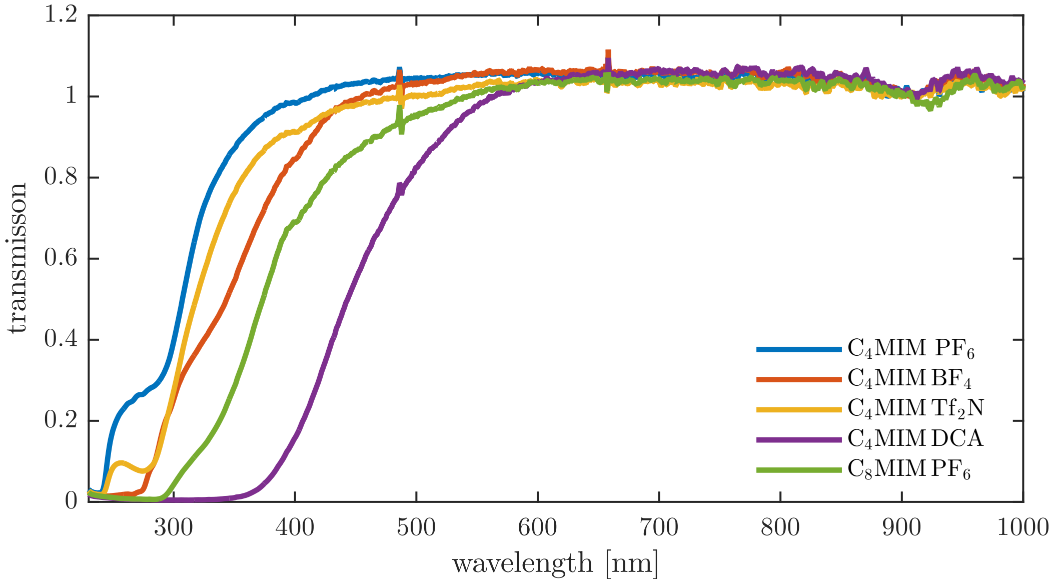

Figure 5.20: Transmission of different anions and cations investigated in this thesis. Slight changes in the optimal focus of the fiber cable cause deviations of the transmission ($T > 100\%$). Data partly taken in cooperation with I. Barke and K. H. Meiwes-Broer, Universität Rostock.

The different refractive indices $n = \sqrt{\epsilon}$ given in table 2.1 cause a shift of the cutoff wavelength, which becomes obvious considering the oscillator model (see figure 4.1). Thus the cutoff of the C_4MIM based ionic liquids shifts in the same sequence to smaller wavelengths than the refractive index shifts to lower values: $PF_6 < BF_4 < Tf_2N <$ DCA. Except for C_8MIM PF_6 and C_4MIM DCA all considered ILs have 100% transmission at the cluster plasmon wavelength of $\approx 400\,$nm. Since the different ionic liquids have different absorption cutoffs at small wavelengths the energetic cutoff is chosen for the cluster plasmon spectra appropriately in the corresponding figures.

To ensure data comparability the experiments with different ionic liquids have been performed using the same cluster deposition rate of $0.3\,$Å/s. All ionic liquids have been degassed the same way (24 hours at 80 °C under vacuum conditions). For all experiments at first the *in-situ* spectra during cluster deposition are presented, followed by the *ex-situ* spectra recorded after sample removal from the UHV chamber.

However, here only the results of first experiments on cluster depositions into different ionic liquids will be presented. A systematic analysis also concerning sample stability at different temperatures is still pending.

5.3.1 C_4MIM Tf_2N

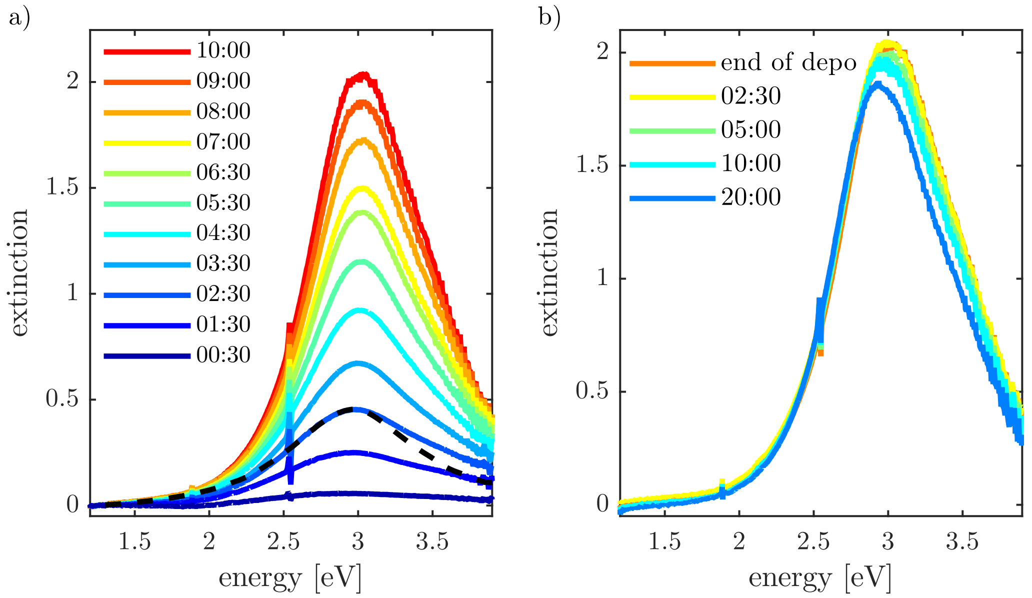

Figure 5.21: a) Deposition of 2 nm Ag clusters in C_4MIM Tf_2N. b) Spectra taken after deposition during cluster source shutdown. The time is given in *MM:SS* after deposition.

Figure 5.21a) shows the spectra taken during the deposition of 2 nm Ag clusters in C_4MIM Tf_2N. The expected cluster plasmon peak position for 2 nm Ag clusters in C_4MIM Tf_2N (n=1.44) is 3.15 eV analogously the consideration presented in figure 4.7. However, as also observed for C_4MIM PF_6 the cluster plasmon resonance for clusters in C_4MIM Tf_2N is at lower energies (2.93 eV) and shifts to 3.02 eV during deposition. The FWHM decreases from

1.1 eV to 0.79 eV. The black dashed line shows the theoretical spectrum with $A = 1.35$ and $n = 1.35$.

After the deposition is finished, the source is shut down and the UV/Vis absorption measurements is continued (figure 5.21b)). In contrast to the depositions performed using C_4MIM PF_6 no further increase of the extinction can be observed, meaning that all deposited clusters are already mixed into the volume during deposition. This behavior can be explained by the reduced viscosity of C_4MIM Tf_2N (0.056 Pa·s compared to 0.354 Pa·s). However, within 20 minutes of source shutdown the extinction decreases remarkably from 2.02 to 1.85 and the peak shifts to 2.95 eV, indicating the sample is not stable. This presumption is confirmed in the *ex-situ* measurements in the cuvette. The results are presented in figure 5.22. Note that the red and green spectra that show the measurements performed in the cuvette, are multiplied by a factor 6 to compare them with the last spectrum recored inside the tub. By transferring the sample from the tub into the cuvette the maximum extinction is significantly decreased and broadened, after 24 hours of storage at room temperature result in a completely aggregated sample.

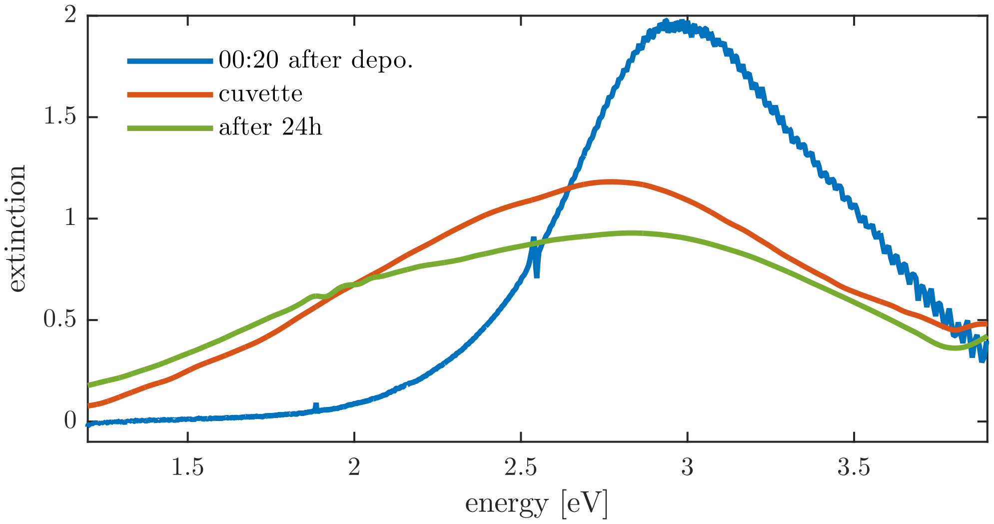

Figure 5.22: Aggregation at room temperature in C_4MIM Tf_2N. The *ex-situ* spectra (green and red) are multiplied by a factor 6 for comparison with the last recorded *in-situ* spectrum.

5.3.2 C_4MIM BF_4

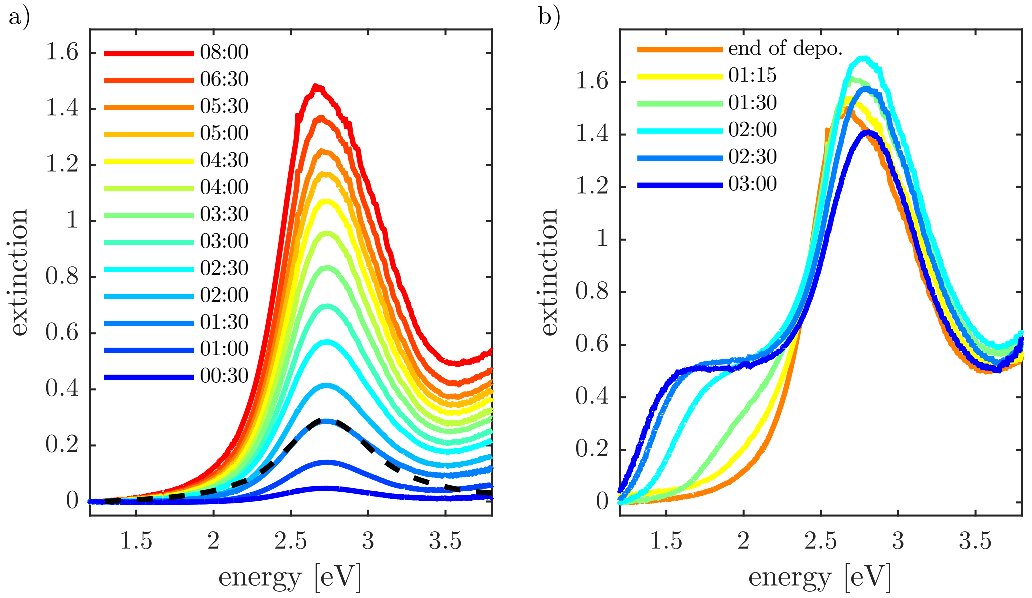

Figure 5.23: a) Deposition of 2 nm Ag clusters in C_4MIM BF_4. The time is given in *MM:SS*. b) Spectra taken after deposition during cluster source shutdown. Here the legend denotes the time in *HH:MM* after the end of deposition.

Figure 5.23a) shows the spectra taken during the deposition of 2 nm Ag clusters in C_4MIM BF_4. Its refractive index (n=1.434) is comparable to the one of C_4MIM PF_6, though the viscosity is also reduced (0.094 Pa·s). The expected peak position for 2 nm Ag clusters in C_4MIM BF_4 is 3.155 eV. However, the recorded spectra show a cluster plasmon resonance at 2.73 eV, which shifts to even lower energies (2.65 eV) during deposition. The peak is comparably narrow with a FWHM of 0.63 eV, that decreases to 0.55 eV. The parameters for the theoretical spectrum (black dashed line) are $A = 0.8$ and $n = 1.9$.

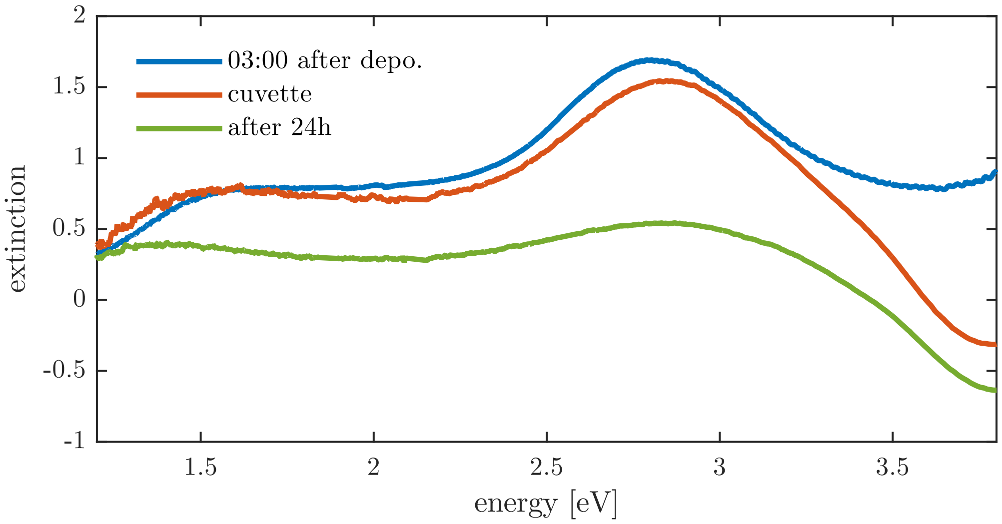

Figure 5.24: Aggregation at room temperature in C_4MIM BF_4. The *ex-situ* spectra (red and green) are multiplied by a factor 6 for comparison with the last recorded *in-situ* spectrum.

The stability of this sample has been investigated inside THECLA, analogous to the description in section 5.2.4. After 90 minutes the FWHM of the cluster plasmon is broadened, followed by the development of a pronounced shoulder at 1.5 eV after 2 hours. The intensity of this feature is constant between 2:30 and 3 hours, while simultaneously the intensity of the single particle resonance decreases. This peak splitting again suggests the formation of chain-like arrangements.

Figure 5.24 shows the *ex-situ* spectra after sample removal from the UHV chamber. Again the spectra are multiplied by a factor of 6 for comparison with the *in-situ* spectrum (blue). Peak position and shape are identical for the last *in-situ* data and the first in the cuvette over the entire energy range, except for deviations above 3.2 eV, which can be explained by discrepancies from the reference and the spikes at 1.9 eV and 2.2 eV caused by artifacts of the UV/Vis lamp. After 24 hours the sample is aggregated.

From this experiment it can be concluded that deposited 2 nm Ag clusters deposited in C_4MIM BF_4 behave similar to those deposited into C_4MIM PF_6, although both ILs differ slightly in viscosity.

5.3.3 C_8MIM PF_6

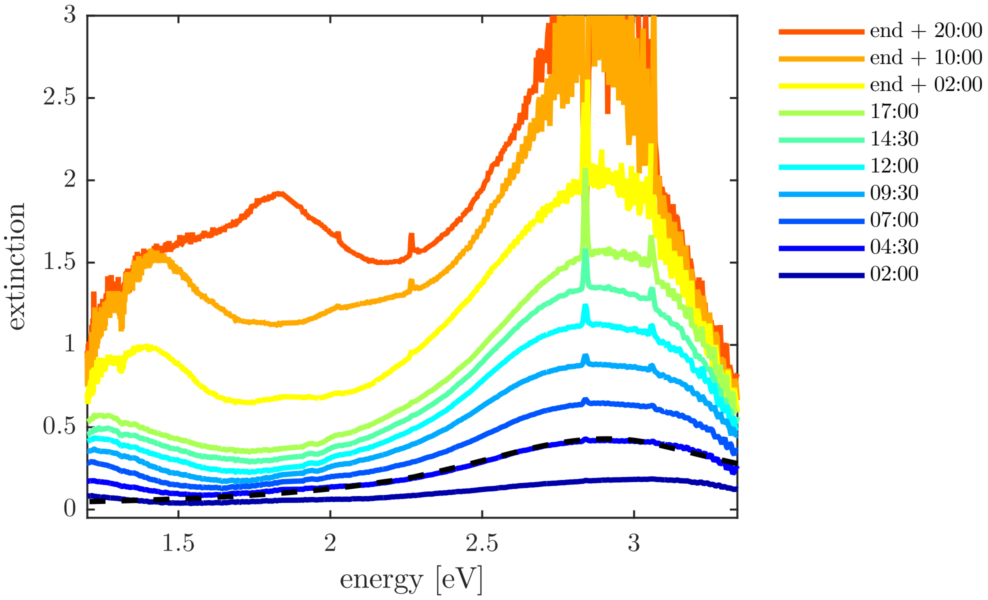

Figure 5.25: Deposition of 2 nm Ag clusters in C_8MIM PF_6. The spectra were taken during deposition and up to 20 minutes after deposition. The time is given in *MM:SS*.

According to the transmission measurements shown in figure 5.20 C_8MIM PF_6 has a similar cutoff wavelength, but a lower transmission at 400 nm compared to C_6MIM PF_6. Therefore the *in-situ* spectra in figure 5.25 are comparably noisy at high extinctions.

The spectra are very broad with high extinctions at low energies. The cluster plasmon resonance peak is expected to be at 3.16 eV, while it is at 2.73 eV during deposition. In contrast to the previous experiments the cluster plasmon changes significantly after the end of the deposition process. Not only the maximum extinction, but also the shape of the spectra change. Within 20 minutes the maximum extinction increases from 1.5 after deposition to ≈ 3. This behavior can be explained by the increase viscosity of an ionic liquid with increasing alkyl chain length. $\eta_{\mathrm{C_8\,MIM\,PF_6}}$ is twice as high as $\eta_{\mathrm{C_8\,MIM\,PF_6}}$ (cf. table 2.1). A larger viscosity inhibits the mixing process and thus a large amount of clusters is still at the surface of the mixer and has not successfully been mixed during deposition. The high extinction at low energies and the development of the second peak at 1.8 eV are indicators for aggregation already during deposition, probably at the mixer surface.

After the sample is removed from THECLA and filled into a cuvette, the extinction is significantly reduced as shown in figure 5.26 compared to the "last usable" *in-situ* spectrum. Again, after 24 hours it is completely aggregated.

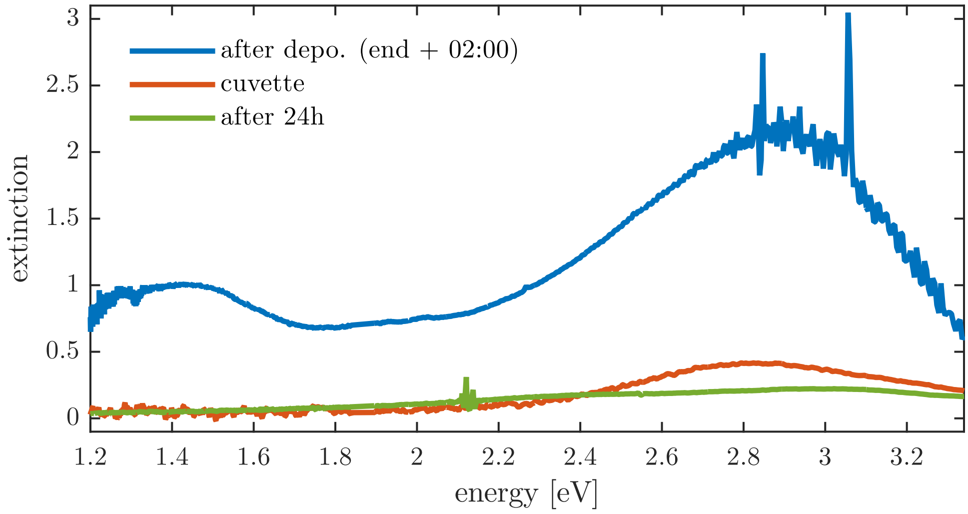

Figure 5.26: Aggregation at room temperature in C_8MIM PF_6. The *ex-situ* spectra (red and green) are multiplied by a factor 6 for comparison with the last recorded *in-situ* spectrum.

5.3.4 C_4MIM DCA

Figure 5.27a) shows the spectra taken during the deposition of 2 nm Ag clusters in C_4MIM DCA. According to table 2.1 C_4MIM Tf_2N has the lowest viscosity of all investigated ionic liquids. In comparison to all other investigated ionic liquids C_4MIM DCA cuts already off below 380 nm. Therefore the resulting spectra seem to have a steeper right flank.

Due to the comparably high refractive index of 1.5085 the cluster plasmon is expected to be at 3.08 eV. The *in-situ* measurements reveal a peak shift from 2.84 eV to 2.74 eV and a small FWHM of 0.58 eV. After deposition the extinction decreases from 0.99 to 0.8 within 30 minutes during cluster source shutdown.

The low viscosity of C_4MIM DCA suggests an unstable sample, which already is apparent in the decrease of extinction during cluster source shutdown. After taking the sample out of the UHV chamber and filling it into a cuvette, almost no plasmon is detectable in the *ex-situ*

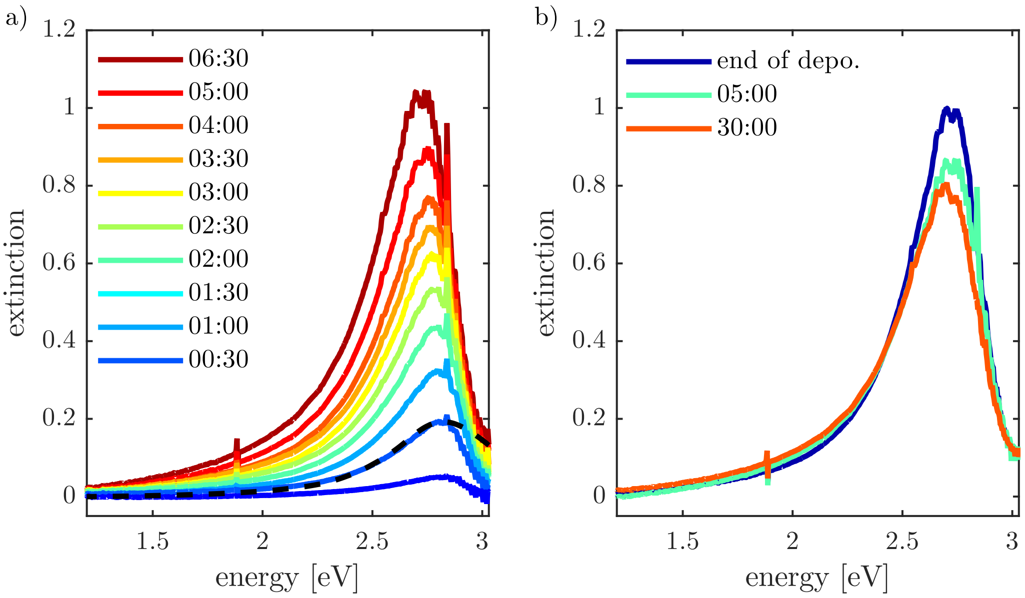

Figure 5.27: Deposition of 2 nm Ag clusters in C_4MIM DCA. The spectra were taken during deposition and up to 30 minutes after deposition. The time is given in *MM:SS*.

UV/Vis absorption measurement, which is shown in figure 5.28. Since the optical alignment of the cuvette holder is better than in the *in-situ* measurements the energy range can be extended to 3.5 eV. The maximum extinction decreased to 0.03, which is far below the expected extinction of 0.17. The peak has shifted to 3.29 eV. These changes and the significant decrease of the cluster plasmon extinction suggest a high instability of the sample.

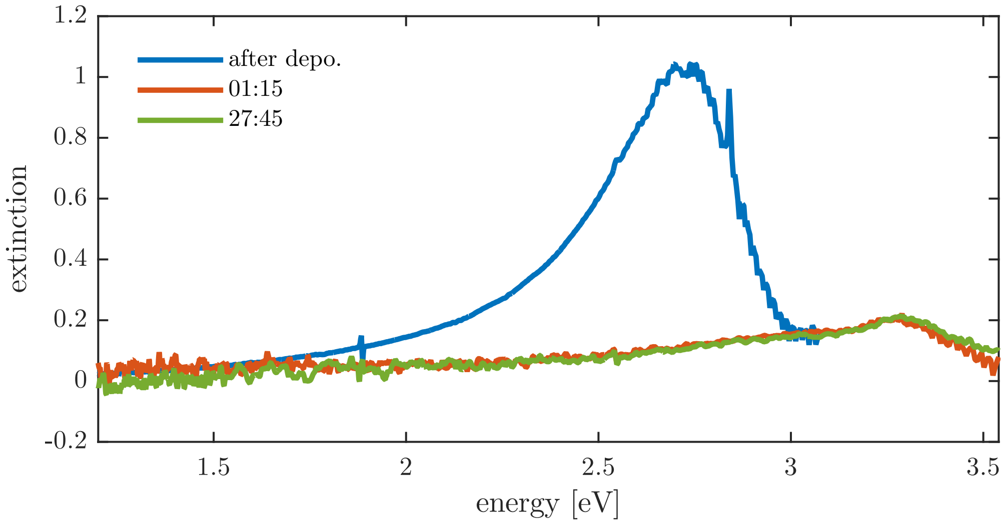

Figure 5.28: *Ex-situ* UV/Vis measurement of Ag clusters deposited into C_4MIM DCA. Almost no cluster plasmon is detectable anymore immediately after deposition.

5.3.5 Discussion

Sputtering experiments performed by Vanecht *et al.* [Van12] revealed significant differences in the stability of gold nanoparticles in C_4MIM PF_6, C_4MIM BF_4, C_4MIM Tf_2N and C_4MIM DCA. They differentiate between a phase of equilibrium between the formation of new particles and the aggregation of nanoparticles, with results in a constant peak height and a shift of the plasmon band, and a phase in which the particles aggregation exceeds the formation rate of new nanoparticles, which leads to a decrease of the extinction. The latter phase starts 2 hours, 12 hours, 2 days and 5 days after sputtering for C_4MIM DCA, C_4MIM Tf_2N, C_4MIM BF_4 and C_4MIM PF_6, respectively. The coagulation rate is inversely proportional to the viscosity of the ionic liquid.

However, these timescales cannot directly be compared to the results of this thesis because there is no formation of new particles for samples prepared with preformed clusters.

The *in-situ* measurements showed that the viscosity of the ionic liquid directly influences the mixing process. The extinction of samples with low viscosities smaller than $\eta_{\mathrm{C_4MIM\,PF_6}}$ does not increase after the deposition is finished, while for C_8MIM PF_6 the viscosity seems to be too large for appropriate mixing. The clusters aggregate at the mixer surface. Further, the extinction of the main peak decreases roughly by a factor of 2 after deposition.

To conclude, the performed experiments confirm the results found by Richter *et al.* and Vanecht *et al.* . C_4MIM PF_6 is the most suitable ionic liquid for stable sample production. Clusters deposited into C_4MIM BF_4 shows similar aggregation behavior than C_4MIM PF_6 (formation of chain-like arrangements on similar time-scales). The sample produced using C_4MIM Tf_2N is also quite stable, while C_4MIM DCA after removing it from the UHV chamber as well as the previously discussed C_8MIM PF_6 are unstable.

The experimental results show that viscosity is not the only parameter regulating sample stability during deposition. Even though the viscosity of C_4MIM BF_4 is 3.7 times smaller than the viscosity of C_4MIM PF_6, they show similar behavior during deposition.

Chapter 6

X-Ray Absorption Spectroscopy: Theory and Experimental Implementation

The results of UV/Vis spectroscopy provides an insight into the interaction of silver clusters with ionic liquids, but it is not possible to differentiate between geometric shapes of the aggregates. In particular, it is not possible to differentiate between agglomeration and coalescence. The structural information of clusters is hardly to gain due to missing long-range order and diluted sample density. X-ray absorption spectroscopy (XAS) is a suitable tool to encode the local environment, including both atomic and electronic structure of the sample, for either solid or liquid samples by investigating the X-ray absorption of core-level electrons.

This chapter starts with a brief review about the electronic structure of atoms in order to understand the processes of photoabsorption and photoemission. Afterwards X-ray absorption and the resulting changes in the absorption coefficient of the material under investigation are presented. The next section introduces the used setup at beamline P64 (DESY, Hamburg). Details on the fluorescence detection of the emitted photons and consequences for data evaluation are discussed afterwards.

6.1 Electronic Configuration

According to Bohr's postulation every atom has discrete energy levels. Due to the spherical symmetry of an atom in quantum mechanics the state of each electron is described as a spherical wave function that solves the Schrödinger equation. Four quantum numbers are required to describe a state of an electron in an atom completely: the principal quantum number $n = 1, 2, 3, ...$, the azimuthal angular quantum number $l = 0, 1, ...n-1$, the magnetic quantum number $m_l = -l, -l+1, ..., l$ and the spin quantum number $m_s = -s, -(s-1), ..., s$ ($s = \frac{1}{2}$ for electrons). The angular momentum l and the spin s couple to the total angular momentum $j = |s + l| = |l - s|, |l - s| + 1, ..., l + s$ [Gri04].

Atomic levels with the same principal quantum number n are grouped into so-called shells. The Pauli exclusion principle requires that the electrons – since they are fermions – may never be in the same quantum state. Therefore each electron in an atom must vary at least in one quantum number. From that condition it follows that each shell can hold up to $2n^2$ electrons. There are different conventions related to the designations of the different shells. The energetic levels are grouped into "transition groups" according to their quantum number $n = 1, 2, 3, ...$ as K, L, M,..., with each group having a subindex: *1* ($j = 1/2, l = 0$), *2* ($j = 1/2, l = 1$), *3* ($j = 3/2, l = 1$) and so on. In chemistry the orbitals are denoted according to their quantum numbers n and l, where s, p, d and f stand for $l = 0, 1, 2, 3$, respectively. The electronic configuration, corresponding names and notation of possible electron transitions between different (sub-)shells are schematically shown in figure 6.1 for a copper atom (electronic configuration [Ar] $3d^{10}$ $4s^1$). The electron transitions are named the final shell. A Greek letter denotes the difference Δn to the initial shell (Δn=1: α, Δn=2: β,...). To differentiate between the spectral lines of one shell, a numeric value is used.

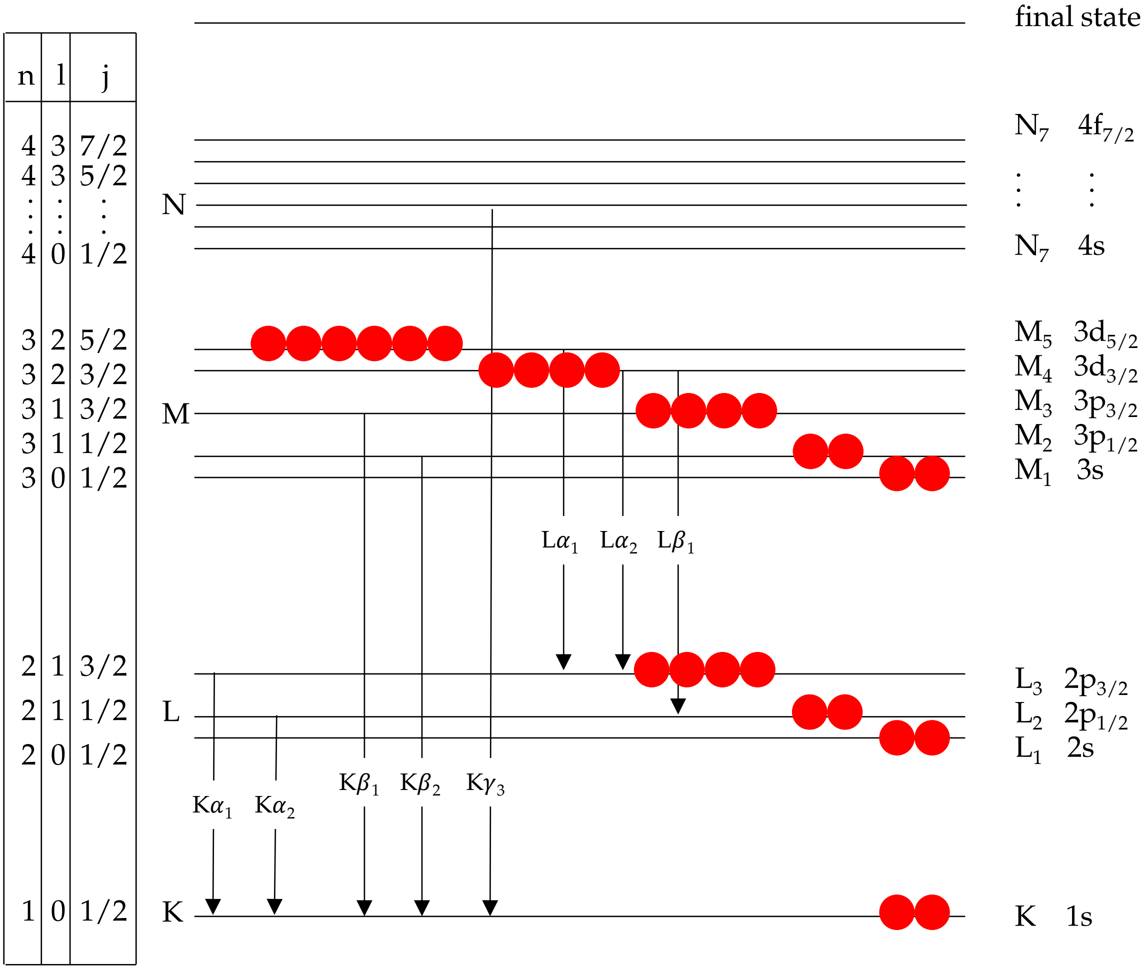

Figure 6.1: Notation of energetic levels and possible electron transitions, exemplarily shown for copper [Att99].

6.2 X-ray Absorption and Emission

The quantity measured in XAS is the absorption coefficient μ, giving the probability for an X-ray being absorbed in matter as a function of the incident energy. Lambert-Beer's law describes the attenuation of light that travels through a sample of thickness d. It relates the incident X-ray intensity I_0 and the intensity $I(d)$ behind the sample:

$$I(d) = I_0 \exp(-d\mu) \tag{6.1}$$

The absorption coefficient is defined as $\mu = \frac{\rho_m N_A}{M} \cdot \sigma$, thus being proportional to the absorption cross section σ. ρ_m is the mass density, N_A Avogadro's number and M the molar mass [New08; Bun10]. Further, an empirical relation for the relation between the absorption coefficient, the incident energy E and the atomic number Z can be given: $\mu \propto \frac{\rho Z^4}{AE^3}$, where A denotes the atomic mass and ρ the sample density [Als11]

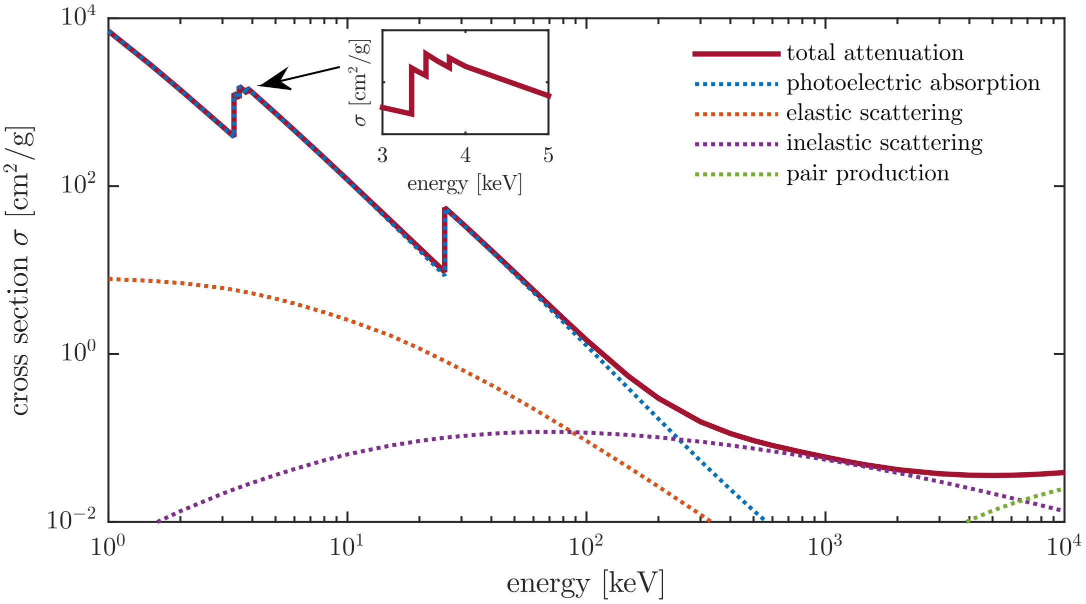

Figure 6.2: Energy dependent cross section σ of silver. The total attenuation (solid red line) is dominated by photo absorption (dotted blue line), while the cross section of (in-)elastic scattering is about two orders of magnitude less and pair production is negligible for energies considered in XAS. In addition to the strong energy dependence sharp rises in σ between 3 and 4 keV (see inset) as well as at 25.5 keV are visible that correspond to the core-level binding energies of the silver atom. Data were taken from [Ber10].

Figure 6.2 shows the cross section $\sigma = \mu/\rho$ for silver in the energy range of 1-10^4 keV. The cross section is dominated by contributions from the photoelectric effect (blue line); contributions from elastic (orange line) and inelastic (purple line) scattering are two orders of magnitude smaller and contributions from the production of electron-positron pairs at energies above 1.022 MeV (green line) can be neglected in the energy range of XAFS, that is usually defined as 0.1-100 keV [Bun10]. The cross section shows sudden jumps (so-called *absorption edges*) for certain energies that are characteristic for the atoms in the material. Those energies correspond to the core-level binding energies (see figure 6.1).

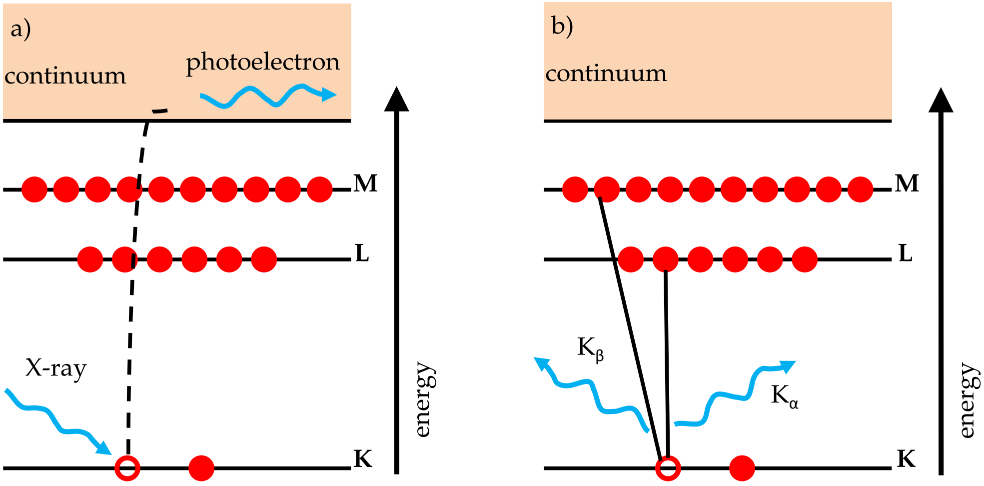

Figure 6.3: a) shows a sketch of the photoelectric effect. The incoming X-ray photon is absorbed and the core-electron is promoted out of the atom, creating a vacancy in the corresponding core-level. This effect leads to the rise of the absorption edge in the absorption coefficient μ. b) shows one possibility of decay of the excited state of the atom by fluorescence. The probability of X-ray emission is directly proportional to the absorption probability [New08].

If the energy of the incident photon is larger than the binding energy of the core level as is the case in figure 6.3a), it can ionize the atom, consequently creating the sharp increase of the absorption coefficient. The absorption edges are named after the core electron that is excited. For K edge a $1s$ electron is excited, while the L edge is created by the excitation of a $2s$ or $2p$ electron. Figure 6.2 shows the silver K edge at 25.514 keV and the L_1, L_2 and L_3 edges at 3.806 keV, 3.524 keV and 3.351 keV, respectively (cf. figure 6.1). Since absorption edges are unique for each element, XAS is an element-specific technique.

After the photon has been absorbed, the atom is in an excited state with a core hole, which is a vacancy in the energy level of the excited core electron, and a photo electron with an energy $\hbar\omega' = \hbar\omega - E_0$. The subsequent decay of this excited state takes typically place within several femtoseconds, for example with fluorescence as sketched in figure 6.3b). Here the core-hole is filled with electrons from energetically higher core-levels. The remaining energy is released in form of a photon with well-defined energy (for example K_α for electrons from the L level filling a K core-hole or K_β filling a K core-hole from the M level). By definition, the absorption coefficient is proportional to the amount of absorbed radiation and thus proportional to the number of by absorption excited states [Jen12].

Another possibility for the decay of the excited state is the non-radiative Auger effect. The released energy is transferred to another electron, which is ejected from the atom with a kinetic energy corresponding to the difference between the energy of the initial transition and the binding energy of the shell from which the Auger electron is ejected [Küp85]. Fluorescence is the dominating effect in the hard X-ray regime ($E > 2$ keV) [Pus14]. Details on the detection of fluorescence can be found in section 6.4.2.

The core-hole lifetime is defined by the total de-excitation probability per unit time. The larger the atomic number Z and the deeper the core-hole is, the larger is the number of upper levels, from which the core-hole can be filled. Consequently, this corresponds to a shorter core-hole lifetime, which is typically 10^{-15} to 10^{-16} seconds. The core-hole lifetime is correlated with an energy width of the excited state due to the time-energy uncertainty relation $\Delta E \cdot \Delta t \geq \frac{\hbar}{2}$. Thus the core-hole lifetime contributs to the resolution of X-ray absorption spectra [Bun10].

A complete XAS spectrum is obtained by tuning the energy of the incident photons from just below the edge up to $1000\,\mathrm{eV}$ above the edge. As shown in figure 6.4 it can be divided into two sections. The region directly behind the absorption edge (up to $50\,\mathrm{eV}$ as a general rule) is called **X**-ray **A**bsorption **N**ear **E**dge **S**tructure (XANES), while the region above the XANES is called **E**xtended **X**-ray **A**bsorption **F**ine **S**tructure (EXAFS). The term XAS summarizes these spectroscopy techniques, both being based on the energy dependent absorption coefficient, but different in mathematical description, experimental details and information content.

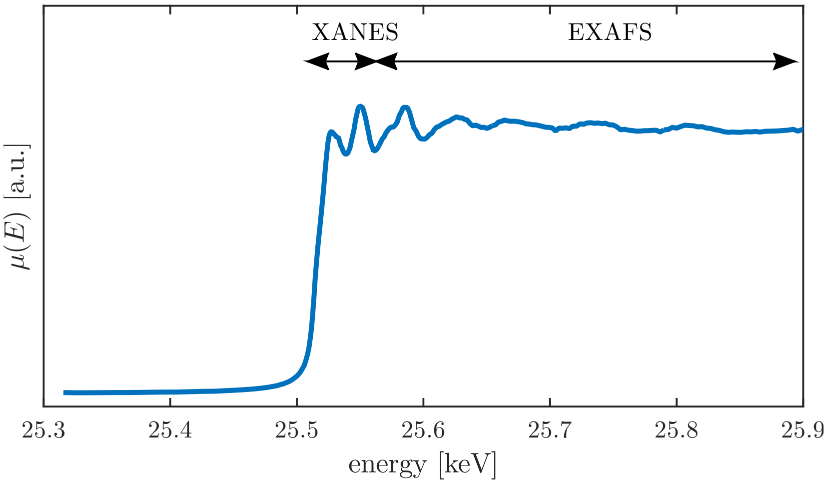

Figure 6.4: Experimental K edge XAFS spectrum of a $100\,\mathrm{nm}$ Ag foil. The total spectrum can be divided into the near edge region ("XANES") and the extended region ("EXAFS"). The transition between both regions is somewhat arbitrary.

Photoelectrons ejected via the absorption of X-ray photons with an incoming energy in the XANES region do not have enough energy to be promoted into the continuum; therefore this region is dominated by electronic transitions between inner shells and unoccupied states; both yield information on atomic levels and the chemical state (for example oxidation or sulfidation) of the sample. The oscillations in the EXAFS region, the so-called fine structure of the absorption coefficient, are caused by the scattering of the photoelectron wave from the atoms surrounding the absorbing atom, creating interference between the outgoing and back-scattered waves. As the energy of the incoming photons is increased, the wavelength of the corresponding electron is decreased, resulting in constructive or destructive interferences depending on the interatomic distances. By fitting the oscillations provided in the EXAFS region, structural information like the interatomic distances from the periodicity of the oscillations as well as coordination numbers and identity of the neighbor atoms can be obtained from the EXAFS oscillations. The EXAFS can be described mathematically by the so-called EXAFS equation that will be introduced in the following section.

6.3 X-ray Absorption in Condensed Matter: The EXAFS Equation

X-ray absorption requires the transition between two quantum states. A photon is only absorbed, if there is an available free final state for the photoelectron. The description in this chapter substantially follows the approach given by Bunker [Bun10]. In the following, $\langle i|$ denotes the initial state with an X-ray and a bound core-level electron, while in the final state $|f\rangle$ there is no X-ray, but a core-hole and a photoelectron. The absorption coefficient is then described with Fermi's Golden Rule

$$\mu(E) \propto |\langle f|H_\mathrm{I}|i\rangle|^2 \ \rho(E_F). \tag{6.2}$$

The Hamiltonian H_I describes the interaction between X-ray and sample, that leads to the transition between initial and final state and $\rho(E_F)$ is the density of the final states. The initial state is not affected by neighboring atoms since it is too tightly bound. However, the final state is split up into a part $|f_0\rangle$, that considers the bare atom, and a part $|\Delta f\rangle$ taking into account the neighboring atoms:

$$|f\rangle = |f_0\rangle + |\Delta f\rangle \tag{6.3}$$

With this, equation (6.2) can be rewritten to

$$\mu(E) \propto |\langle i|H_\mathrm{I}|f_0\rangle|^2 \left(1 + \langle i|H_\mathrm{I}|f\rangle \frac{\langle f_0|H_\mathrm{I}|i\rangle^*}{|\langle i|H_\mathrm{I}|f_0\rangle|^2} + c.c. + \mathcal{O}(\Delta f^2)\right) \tag{6.4}$$

$$\mu(E) = \mu_0(E)\left(1 + \chi(E)\right). \tag{6.5}$$

$\mu_0 = |\langle i|H_\mathrm{I}|f_0\rangle|^2$ is assigned as the bare atom absorption, only depending on the absorbing atom as if it had no neighbors. Thus, the term $\chi(E) \propto |\langle i|H_\mathrm{I}|\Delta f\rangle|^2$ describes the fine structure of the absorption coefficient $\mu(E)$. Therefore, the fine structure is proportional to the perturbation of the final state $\mu(E) \propto |\langle i|H_\mathrm{I}|\Delta f\rangle|^2$ by the atomistic environment of the absorbing atom.

The EXAFS signal consists of the sum of all contributions originating from backscattering of the photoelectron wave at the different neighbor atoms, which contribute to the perturbation of the final state. The individual contributions are called scattering paths. Scattering paths originating from the same type of atom with the same distance to the absorber make the same contribution, whereby they are grouped in so-called coordination shells (see figure 6.5a)). The **degeneracy** of a scattering path depends on the number n of atoms in a coordination shell (e.g. $n_1 = 12$ for an fcc structure).

Until now only the process of single scattering of the photoelectron wave and subsequent interference at the absorbing atom has been discussed; as shown in figure 6.5b) also multiple scattering processes are possible, that have significant contribution to the fine structure.

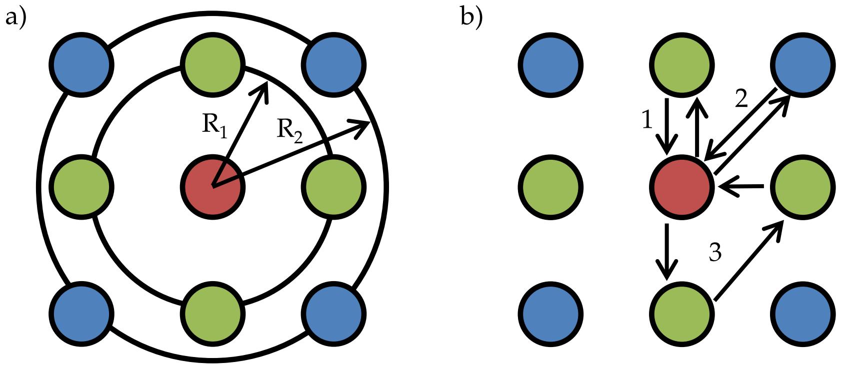

Figure 6.5: a) First (green) and second (blue) coordination shell around the absorbing atom (red). b) Sketch of single scattering paths (1 and 2) and a multiple scattering path (3) [Kon88].

Equation (6.6) gives a quantitative parametrization of the EXAFS spectrum, the so-called **EXAFS equation** that consists of the contribution of all possible scattering paths:

$$\chi(k) = S_0^2 \sum_i n_i \frac{f_{\text{eff},i}(k)}{kR_i^2} \cdot e^{-2k^2\sigma_i^2} \cdot e^{-2R_i/\lambda} \cdot \sin(2kR_i + \delta_i(k)). \tag{6.6}$$

It was initially developed by Sayers, Stern and Lytle [Ste75] for single scattering and was extended afterwards to also consider multiple scattering effects. Here energy and photoelectron wavenumber are related by

$$k = \sqrt{\frac{2m_e}{\hbar^2}(E - E_0)}, \tag{6.7}$$

where m_e is the electron mass, E the energy of the absorbed photon and E_0 the binding energy of the corresponding core-level electron.

In the following a qualitative description of the different terms of equation (6.6) affecting the fine structure will be given. Details on the formal derivation using equation (6.5) can be found in [Kon88; Teo86].

The term f_{eff} is the effective scattering amplitude. f_{eff} depends on the type of atom and on the wavenumber k; the scattering probability is higher at high k for an atom with many electrons. For single scattering this quantity is the atomic form factor of X-ray diffraction. The photoelectron wave is spherically; thus its scattering probability drops with $1/R^2$. A factor $1/k$ is added in order to get a dimensionless expression.

Since the photoelectron was ejected from the absorbing atom, leaving a core-hole behind, the remaining electrons feel more positive charge from the nucleus, which results in an adjustment of the orbitals to this change. The remaining $n-1$ electrons now can relax into a new final state Φ_f^{n-1}. This so-called incomplete overlap is modeled by an element-dependent **amplitude reduction factor** $S_0^2 = \left|\left\langle \Phi_f^{n-1} | \Phi_i^{n-1} \right\rangle\right|^2$ with values between 0.7 and 1.0.

Even in a highly ordered crystal the atoms are never actually on their lattice positions due to **thermal and static disorder**, which distributes atoms around their nominal positions with the mean square radial displacement $\sigma_{i,j}^2 = \langle r_{i,j} - \overline{r_{i,j}} \rangle^2 > 0$. Fluctuations of the atomic positions result in slightly modified path length within a coordination shell and thus influence the interference pattern, which can be seen in a decrease of the EXAFS signal. This behaves somehow like the crystallographic Debye-Waller factor and is taken into account by a factor of $e^{-2k^2\sigma^2}$.

Besides being backscattered and returning to the absorber, the photoelectron may scatter inelastically, excite a valence band electron or a phonon, resulting in a reduction of the energy of the photoelectron and thus its wavelength and the interference. The longer the photoelectron travels, the more likely are these processes. Consequently, this effect is proportional to R_j. Due to its finite lifetime the core-hole already can be filled up before the backscattered photoelectron returns to the absorber. Due to this state modification the overlap between initial and final state (that is used in Fermi's Golden Rule) is different and there is no contribution to the fine structure coefficient. Both effects are considered by replacing the photoelectron spherical wave with a damped spherical wave $e^{-2R/\lambda}$ with the **mean free path** of the electron λ.

The last term of the EXAFS equation describes the EXAFS oscillation. As already discussed the phase depends on the path length R. The **phase shift** $\delta(k)$, which occur due to the electronic potential between the positive nucleus and the negatively charged electron.

Since an EXAFS spectrum samples over a large number of absorbers, the distribution of scattering atoms around an absorber does not necessarily have to be identical. This is for example the case for small metal nanoparticles [Cla00]. However, equation (6.6) is actually only valid for bulk structures, assuming that the pair distribution function is Gaussian. This limitation is overcome in the **cumulant expansion**, in which the distances in a coordination shell are described by a probability distribution $P(r_j)$ [Bun83]. This approach results in the introduction of factors $e^{\frac{(2ik)^n}{n!}C_n}$ with the nth cumulant C_n. For the EXAFS analysis of clusters the third cumulant is helpful, describing the asymmetry of the distribution:

$$C_3 = \left\langle (r - \bar{r})^3 \right\rangle \tag{6.8}$$

The EXAFS signal consists of a sum of k dependent sine oscillations. By Fourier transformation a representation in real space can be achieved, which is related to interatomic distances. For single scattering events the distance between absorbing atom and scattering atom is equivalent to half of the path length. Multiple scattering events, however, give contributions in real space that cannot directly be attributed to those distances. Due to the phase shift $\delta_i(k)$ in equation (6.6) the maxima in real space do not exactly match the true distances R_j, but are shifted by about -0.5 Å.

6.4 Experimental Setup for EXAFS Measurements

6.4.1 Beamline P64

All EXAFS measurements have been carried out at beamline P64 of the synchrotron light source PETRA III (DESY, Hamburg). Synchrotron radiation is highly brillant with a broad spectrum and has its origin in the deflection of relativistic charged particles in a magnetic field, occurring in either dipole magnets or so-called insertion devices (undulators and wigglers), which are alternatingly arranged dipole magnets [Als11], producing highly intense radiation.

One octant of the original storage ring PETRA (circumference 2.3 km) has been modified to the third generation light source PETRA III operating at an energy of 6 GeV [Wec04; PET17]. Originally, PETRA III had 14 so-called beamlines, which are tangential straight paths to the storage ring circumference, where the synchrotron radiation travels to experimental end stations. Beamline P64 is a time resolved and bio X-ray absorption spectroscopy beamline. It was built within the framework of the Petra III extension, that was started in February 2014 in order to setup ten additional beamlines [Wel12; DES12].

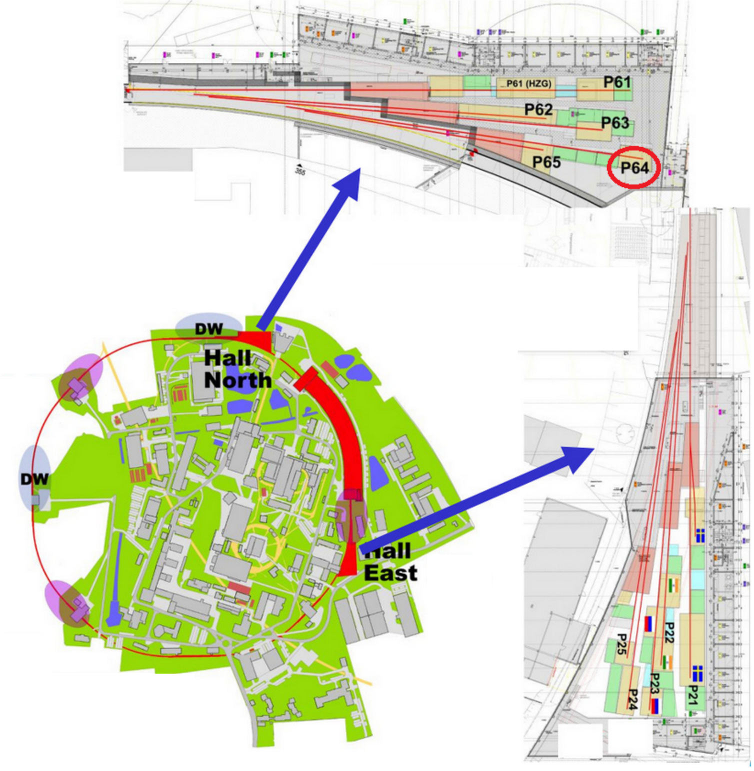

Figure 6.6: Sketch of PETRA III storage ring and north and east hall of PETRA III extension, where beamline P64 is located [Wel12; Mar16].

An undulator with 60 periods of 32.9 mm produces a photon flux of 10^{13} photons/s at the sample at 8.9 keV. The photon energy is tuned by a liquid N_2 cooled double crystal monochromator exploiting Si(111) or Si(311) reflection and simultaneous variation of the undulator gap, offering a total energy range of 4.5-70 keV with a resolution of $\Delta E/E = 1.4 \cdot 10^{-4}$ and $5 \cdot 10^{-5}$, respectively [Wel12]. The beam is focused by two mirrors (depending on the energy range coated with Si, Pt or Rh) to a beamsize between $2\,\mathrm{mm} \times 1\,\mathrm{mm}$ and $150\,\mu\mathrm{m} \times 50\,\mu\mathrm{m}$ (horizontal × vertical direction) [Wel12].

6.4.2 Fluorescence Detection

As introduced in section 6.2 in a XAS experiment the absorption coefficient μ given by

$$\mu \propto \ln\left(\frac{I_0}{I}\right) \tag{6.9}$$

is measured. Therefore, the incident and transmitted intensities I_0 and I in front of and behind the sample need to determined, which is usually done using ionization chambers. In an ionization chamber the incident photons ionize the atoms of the filling gas. The electrons are separated from the ions using high voltage. The resulting current is proportional to the number of absorbed photons.

However, in samples with low concentrations only a small fraction of photons is absorbed in the sample, causing a low signal to noise ratio. This can be overcome by using another experimental geometry, measuring XAS in fluorescence mode (I_F) as introduced in section 6.3. After the incoming photon is absorbed, the atom is in an excited state because the electron was promoted from the state with initial energy E_i into a energetically higher state E_f, leaving a hole in the former core level. The photon energy after this process is $\hbar\omega' = \hbar\omega(E_f - E_i)$. The excited state of the atom can be relaxed by an electron from an energetically higher shell. The residual energy is emitted as a photon with characteristic energy. By definition, the absorption coefficient is proportional to the amount of absorbed radiation and thus proportional to the number of by absorption excited states as sketched in section 6.2. The photons that are emitted by recombination, is proportional to the absorption coefficient as well.

The used detector is an energy dispersive segmented single crystal 100 pixel High-Purity Germanium detector from Canberra Industries. To avoid the transition of electrons into the valence band, the detector is operated at liquid nitrogen temperature (77 K).

Fluorescence radiation is isotropic, while scattering has an angular dependence. The probability of scattering in the elastic limit is given by

$$P(\alpha, \beta) \propto \left(1 - \sin^2\alpha \cos^2\beta\right)\, d\alpha d\beta, \tag{6.10}$$

where α denotes the angle relative to the incident direction and β the angle relative to the plane of polarization [Hei84]. Synchrotron radiation is horizontally polarized; in order to minimize the contribution from scattering the detector is mounted at the same table as the sample ($\beta = 0$). In order to minimize scattering the detector is placed perpendicularly to the incident beam ($\alpha = 90°$, see figure 6.7). Nevertheless, due to the finite dimensions of a detector elastic scattering can never be eliminated. Inelastic scattering (e.g. Compton scattering) shows a more complicated angular dependence. Therefore, this cannot be completely suppressed and will be considered later during data processing. The choice of the sample position with respect to the incident beam depends on the sample thickness. For the investigated samples an angle of $45°$ is chosen.

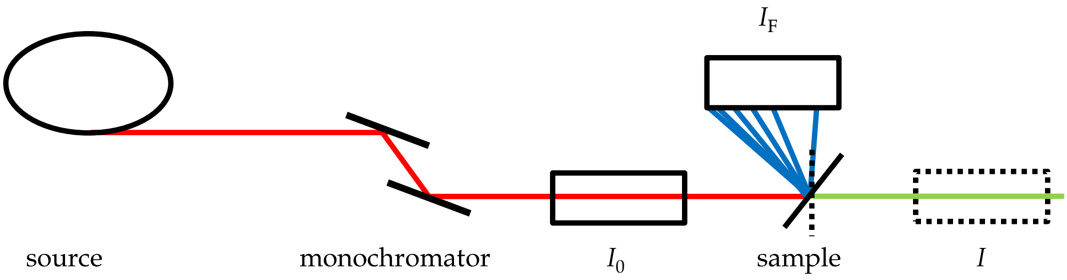

Figure 6.7: Experimental geometry for transmission I (green line) and fluorescence I_F (blue lines) detection [Bun10].

For data reduction a final fluorescence spectrum per incident energy needs to be calculated from the fluorescence spectrum each detector pixel has recorded. A reference measurement is used to calibrate each detector pixel. An example for a total spectrum at an incident energy $E_0 = 25.85\,\text{keV}$ is shown in figure 6.8. The K_α and K_β fluorescence lines of the krypton gas in the ionization chamber can be found at $12.647\,\text{keV}$ and $14.111\,\text{keV}$, respectively. For the sample investigated in this thesis the fluorescence line of interest is the Ag K_α line at $25.514\,\text{keV}$, which is superimposed by the (in-)elastic scattering. For dilute samples the fluorescence line of interest is substantially small compared to the scattering line.

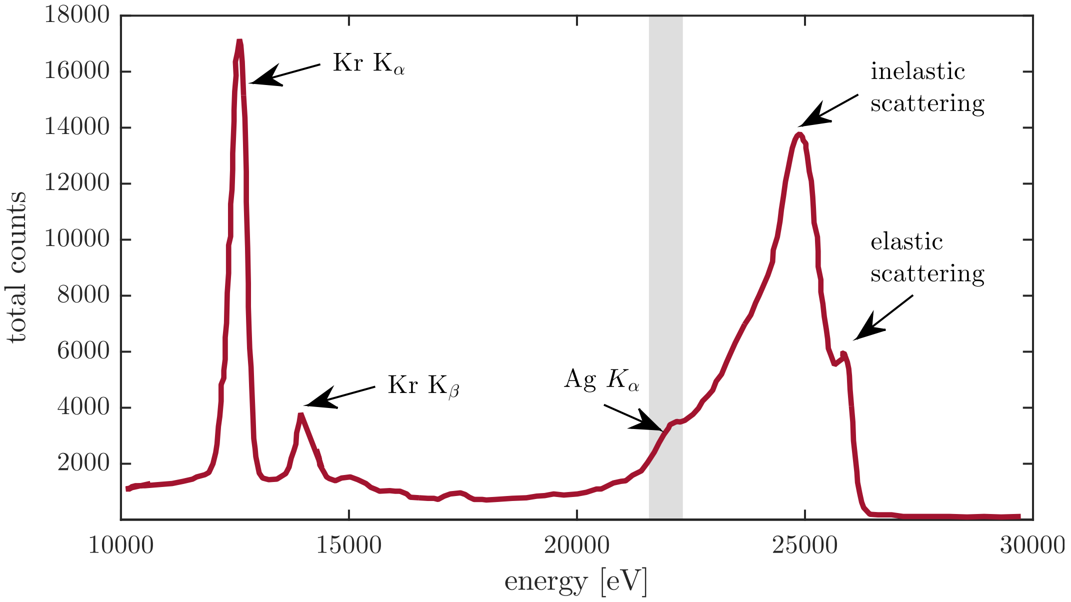

Figure 6.8: Total fluorescence spectrum of a dilute Ag sample ($10\,\mu\text{g/ml}$) at an incident energy $E_0 = 25.85\,\text{keV}$. The region of interest (ROI) between $21.6\,\text{keV}$ and $22.3\,\text{keV}$ is marked in grey.

There are two different ways to extract the number of counts that derive uniquely from the Ag K_α fluorescence line. One way to do so is to set a so-called region of interest (ROI). Here all counts in the area between 21.6 keV and 22.3 keV are integrated as indicated by the grey area in figure 6.8. However, this also includes undesired counts from the overlap with the tail of the Compton line, which results in a bad signal to noise ratio [Tam11]. Alternatively a fitting procedure has been developed by L. Martín Montoya [Mar16] and applied to the data. In the fitting procedure (exponentially modified) Gaussian functions are fitted to both the Compton spectrum and to the K_α fluorescence as exemplarily presented in figure 6.9. The contribution of the Ag K_α line (green area) can then be extracted from the total spectrum and contributions originating from the strong overlap with the tail from incoherent scattering are excluded. Another difficulty in setting the ROI is that position of the scattering line shifts away from the Ag K_α line, when the incident energy is increased. This is also avoided using the fitting algorithm.

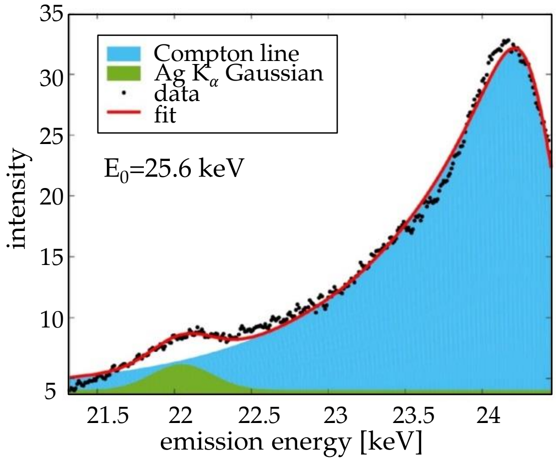

Figure 6.9: Fitting of exponentially modified Gaussian functions to extract the K_α fluorescence line.

In a next step the spectra recorded by each of the 100 detector pixels are reduced to one for each incident energy. The area under the K_α fluorescence peak then corresponds to one point in the XAS spectrum. The XAS spectra obtained from setting a ROI and from using the fitting algorithm for a sample containing 8 µg/ml Ag clusters are shown in figure 6.10. Both spectra are already normalized to the edge jump. In [Mar16] a threshold of 280 µmol/l is given, below which the fitted spectrum shows a significant improvement in terms of the signal to noise ratio. For Ag clusters ($\mathrm{M}_{\mathrm{Ag}} = 107.87\,\mathrm{g\,mol^{-1}}$) this corresponds to sample concentrations < 30.2 µg/ml. Therefore the fitting algorithm was applied to all XAS spectra shown in this thesis except for the reference spectra.

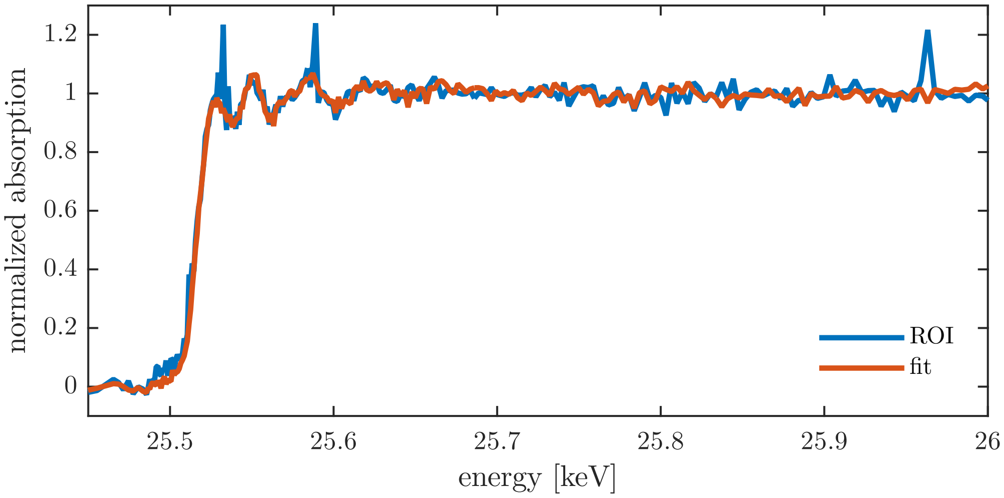

Figure 6.10: Applying the fitting algorithm to extract the contribution of the K_α fluorescence line from the total fluorescence spectrum significantly improves the signal to noise ratio of the XAS spectrum.

6.4.3 Experimental Implementation at P64

Figure 6.11 shows pictures of the experimental setup at P64. The sample cell was constructed in the master's thesis of Thomas Büning [Bün13]. Originally, the cell has been used to perform temperature-dependent X-ray diffraction measurements of liquids. For the purpose of this thesis the sample cell was adapted to realize X-ray absorption measurements. 2 ml of the sample under investigation is filled into the sample holder (inset in figure 6.11a)), which is sealed with Kapton windows that are screwed against Viton seals. The sample holder has a thickness of 1.16 cm, which corresponds to the absorption length of C_4MIM PF_6 (calculated using the database [Hen93]), and has a 45° bore. The beam path to the fluorescence detector is indicated by red arrows.

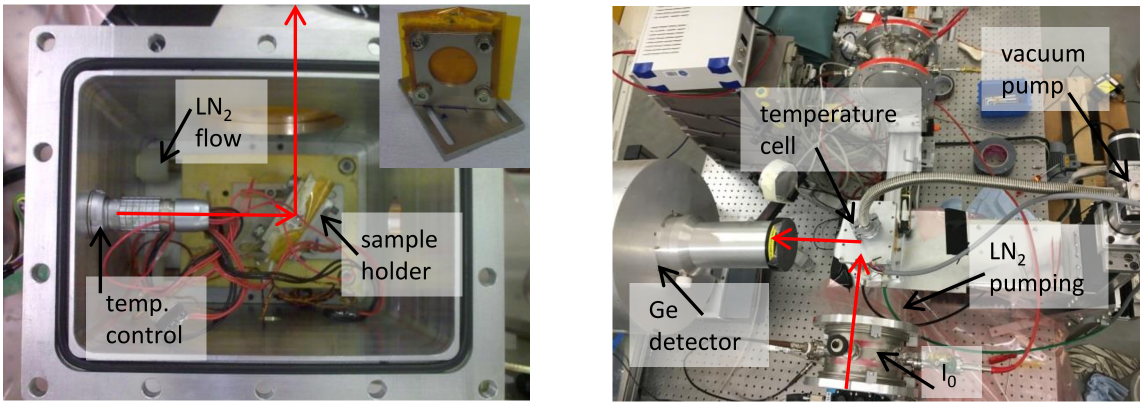

Figure 6.11: Pictures of the experimental setup at beamline P64. Vacuum pump and liquid nitrogen are located outside the experimental table. a) gives an insight into the sample cell that is thermally connected to the sample holder for the purpose of sample cooling. A detailed picture of the sample cell is given in the picture inset. b) gives an overview of the beam path and fluorescence detection with the Ge detector perpendicular to the incoming beam direction (red arrows).

Since temperature is a crucial parameter concerning sample stability, the sample needs to be cooled and to be kept at constant temperature to avoid aggregation during the experiment. Therefore the sample holder is mounted on the copper base of a temperature cell. During the first beamtime liquid nitrogen was pumped through the copper base to enable proper cooling. To adjust the desired sample temperature the liquid nitrogen flow is regulated by an "Analyt Mass Flow Controller GFC" flow regulator and counter heating is realized using a MINCO heating foil, which is mounted between copper base and sample holder. The current sample temperature is measured by two thermocouples at different positions at the sample holder. They are connected to a Lakeshore 340 temperature controller, that finally adjusts the heat output of the heating foil to obtain the desired sample temperature between $-100\,^{\circ}\mathrm{C}$ and $60\,^{\circ}\mathrm{C}$. During the second beamtime the flow of liquid nitrogen was replaced by a Lauda circulation thermostat.

Figure 6.11b) gives an overview of the complete experimental table with closed temperature cell. The cell is evacuated with a rotary vane pump to avoid the condensation of water at the sample holder. At the bottom of figure 6.11b) the krypton filled ionization chamber is shown which determines the incident beam intensity I_0 for normalization purposes. The beam path again is marked by red arrows. It enters the temperature cell through Kapton windows and penetrates the sample inside the sample holder. The emitted fluorescence photons are detected perpendicular to the incoming beam direction with the Ge fluorescence detector (see section 6.4.2).

6.4.4 Data Acquisition

At first a $100\,\mathrm{nm}$ Ag foil is measured as a reference. Afterwards the sample is filled into the sample holder and cooled down to avoid sample aggregation during the experiment. Usually more than one EXAFS scan is recorded for each sample, in particular if the concentration is very low. The spectra are merged afterwards by averaging all scans.

The energy of the incident photons is tuned from $200\,\mathrm{eV}$ below to $500\,\mathrm{eV}$ above the absorption edge. The used energy ranges are given relatively to the energy of the Ag K absorption edge. In the range between $-200\,\mathrm{eV}$ and $-50\,\mathrm{eV}$ a data point is taken every $10\,\mathrm{eV}$. In the pre-edge region this rough measurement is sufficient since it is only needed for the determination of the edge step and the pre-edge background subtraction during data analysis (see below). The range $-50\,\mathrm{eV}$ to $-30\,\mathrm{eV}$ and $-30\,\mathrm{eV}$ to $+20\,\mathrm{eV}$ are scanned in more detail ($\Delta E = 3\,\mathrm{eV}$ and $\Delta E = 0.5\,\mathrm{eV}$, respectively). Above the absorption edge ($+20\,\mathrm{eV}$ to $+500\,\mathrm{eV}$) the distance between two scanned intervals is extended to $\Delta E = 2\,\mathrm{eV}$. Due to the relation given in equation (6.7) ΔE can be enlarged without loosing sufficient data density in k-space. In total the recorded spectra consist of 256 data points; each point is scanned for 5 seconds. Including the time needed for monochromator movement an entire EXAFS spectrum is recorded in approximately 30 minutes. After conversion to k-space the EXAFS data is available up to $11.4\,\text{Å}^{-1}$, however, the usable k-range is limited to $9\,\text{Å}^{-1}$ (see discussion below).

Chapter 7

Atomic Arrangement: Results of XAS Measurements

Section 6.3 outlined how – with the help of the EXAFS equation – the EXAFS spectrum can be calculated for a given material, i.e. for known atomic arrangement. In practice one is interested in the inverse problem, namely extracting information about the sample from the recorded EXAFS spectra. The first section 7.1 of this chapter deals with the process of data treatment, which is necessary to convert the data into a standardized form. In a next step the data fitting process is explained.

Afterwards (section 7.2) the results of the EXAFS measurement of a gradually aggregated sample is discussed regarding nearest neighbor distance and coordination number. It is thus possible to draw conclusions on structural changes during the aggregation process. Section 7.3 discusses the experimental results for a sample already aggregated during cluster deposition. Besides conventional EXAFS measurement a setup for simultaneous EXAFS and UV/Vis absorption spectroscopy was developed, which is introduced in section 7.4.

7.1 EXAFS Data Reduction

Before evaluation the data need to be prepared in order to extract the fine structure $\chi(k)$ from the measured absorption spectra $\mu(E)$. For data reduction and fitting the Python based software package LARCH [New13] was used. All steps necessary for data reduction are briefly discussed in the following chapter based on [Cal13], taking the spectrum of Ag film reference as an example. Afterwards the data fitting process is presented in order to obtain structural information of the cluster samples.

7.1.1 Data Calibration and Alignment

During a beamtime it can happen that the monochromator does not retain the energy calibration during several scans, which can be corrected by repeating the reference scans between single sample scans and **aligning** the single scans in case of an energy shift. Sometimes sharp deviations of 20% and more in $\mu(E)$, so-called **glitches**, originating from the monochromator, the electronics or the sample itself, need to be corrected by interpolating a value from the surrounding data points. All spectra recorded for one sample are merged.

Following these steps, an absorption spectrum $\mu(E)$ as shown in figure 7.1a) is obtained. This example shows the step-by-step data reduction for the measurement of an Ag foil.

7.1.2 Extraction of the Fine Structure $\chi(k)$

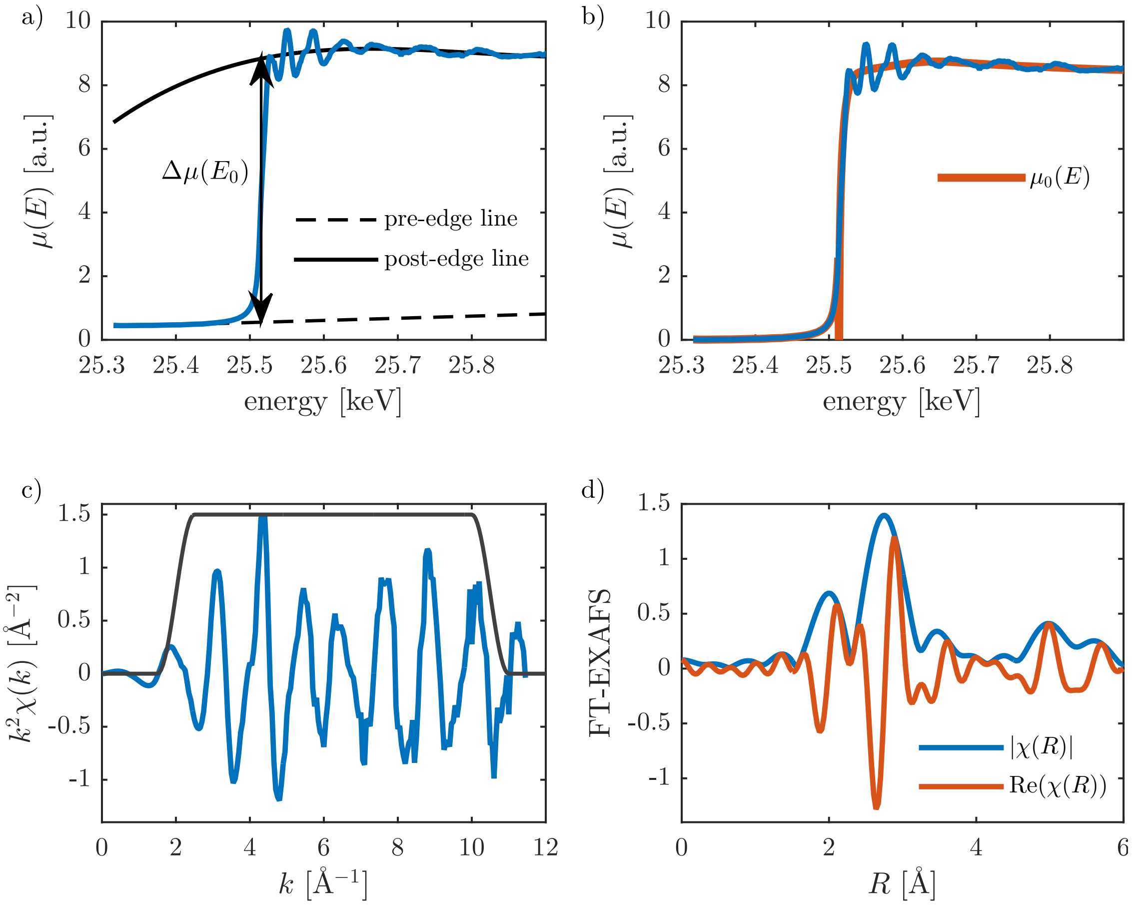

Figure 7.1: Steps of EXAFS data reduction: a) Determination of threshold energy as well as pre-edge function (dotted line) and normalization line (solid) for spectra normalization and pre-edge background subtraction. b) Determination of the background spline function $\mu_0(E)$ (red line) calculated using the AUTOBK algorithm [New93]. A value of $R_{\text{bkg}} = 1.5$ Å was used. c) Extracted and k^2-weighted $\chi(k)$ (blue line) from the Ag reference measurement together with the Hanning-type window (black line) with tapering parameter dx= 1, which is discussed in 7.1.3. d) Magnitude (blue line) as well as the real part (red line) of the FT for the Ag reference measurement.

Before data evaluation the fine structure $\chi(E)$, given by

$$\chi(E) = \frac{\mu(E) - \mu_0(E)}{\Delta\mu(E_0)}, \tag{7.1}$$

has to be extracted from the absorption coefficient $\mu(E)$. E_0 is the absorption edge energy and thus denoting the point, that represents the zero energy ($k = 0$) for the photoelectron. It is usually determined by calculating the first inflection point of $\mu(E)$ (blue line) as shown in figure 7.1a).

In order to determine the edge step $\Delta\mu(E_0)$ for data normalization a linear pre-edge line and a normalization line behind the absorption edge are calculated. In the latter case a second or third degree polynominal is used which should not consider the strong oscillations directly behind the edge. The edge step is then given by the difference between pre-edge and normalization line at E_0. The pre-edge background is removed by subtracting the linear function used for edge step determination described above to eliminate any energy dependencies of the absorption signal other than from the absorption edge. The data is normalized setting the edge step to one, accounts for multiplicative factors like sample thickness, concentration or absorption by the gas in the ionization chambers. For the shown example an energy range of -150 eV to -60 eV relative to E_0 was used for pre-edge fitting, while a second order polynominal from 75 eV to 500 eV behind the edge was chosen for post-edge fitting.

Figure 7.1b) shows the contribution $\mu_0(E)$ (red line) of the bare atom, which does not contribute to the EXAFS oscillations. Since $\mu_0(E)$ cannot be experimentally determined and is not known in general, its course has to be calculated theoretically applying the AUTOBK algorithm [New93], which used polynomial splines of fourth order. An ideal background subtraction suppresses all contributions with unphysically high frequencies, which corresponds to removed Fourier components below R_{bkg} in r-space (see also figure 7.1d)). As a rule of thumb R_{bkg} is approximately half the next neighbor distance. For the shown example a parameter R_{bkg} is chosen [Cal13].

Following all data reduction steps described above, the fine structure $\chi(E)$ is extracted from the EXAFS measurement. Due to the relation between the fine structure and the wavelength of the photoelectron χ is usually given depending on the wave vector k (see equation (6.7)). $\chi(k)$ is often referred to as the "k-space". It decays rather quickly with increasing k; to counteract this effect $\chi(k)$ is usually weighted by k^n with $n = 1, 2, 3$ to give uniform intensity to all oscillations (see figure 7.1c), blue line). Otherwise later the decrease in $\chi(k)$ would lead to broad distorted peaks in the Fourier transformation.

7.1.3 Fourier Transformation

The frequencies of the oscillations in $\chi(k)$ correlate to neighboring coordination shells around the absorbing atom. In the EXAFS equation (6.6) this is taken into account by the sum of damped sine waves. Rapidly oscillating contributions correspond to larger path lengths; all included frequencies can be isolated via Fourier transformation (FT).

Experimental data is always only available in a limited k-range requiring a finite FT in an interval $[k_{\text{min}}, k_{\text{max}}]$. However, carrying out the FT over a limited data range $[k_{\text{min}}, k_{\text{max}}]$ introduces truncation effects. Therefore a window function $W(k)$ is used to gradually increase the amplitude of the data at the endpoints of the chosen interval to avoid sharp discontinuities in the FT of the data. The FT finally reads:

$$\tilde{\chi}(R) = \frac{1}{2\pi} \int_{k_{\text{min}}}^{k_{\text{max}}} k^n W(k) \chi(k) e^{i2kR} \, \mathrm{d}k \tag{7.2}$$

A k^2-weighting and a Hanning-type window (cosine-squared taper) were used to transform the Ag reference data in a k-range between $2\,\text{Å}^{-1}$ and $9\,\text{Å}^{-1}$. k_{min} is chosen depending on where the background spline stops being strongly dependent on small changes in the background parameters, while k_{max} should be exceeded as large as possible with respect to sufficient data quality. A FT is a complex function with real and imaginary part, both providing independent information. In this thesis magnitude (blue) and real part (red) of the FT will be given while discussing the r-space data as shown in figure 7.1d) between $0\,\text{Å}$ and $6\,\text{Å}$.

The EXAFS equation describes the sum over all possible scattering paths; Fourier transforming $\chi(k)$ gives thus features equal to the next-neighbor distances. Although those features correspond to groups of atoms at different distances (this is what will be referred to as a coordination shell), it is important to mention that the FT does not peak at the real interatomic distances. This is why the EXAFS TF is often called a pseudo radial distribution. The photoelectron experiences a phase shift ($\delta(k)$ in equation (6.6)), which is caused by the movement of the photoelectron in the varying potential of the absorbing and backscattering atom. It can be shown, that the frequency of the sine is changed from $2R_i$ to $2R_i - \alpha_j$ with α_i constant, therefore all FT features are shifted by α_j towards smaller R [Ste75]. The value of α_i is usually between $0.2\,\text{Å}$ and $0.5\,\text{Å}$ [Bun10]. Moreover, multiple scattering gives rise to further peaks in the FT. Therefore the EXAFS FT should never be treated as a radial distribution function. Nevertheless, data processing in r-space is really helpful since the underlying structure can be fitted shell by shell to the data.

7.1.4 EXAFS Data Fitting

The process of EXAFS fitting is schematically shown in figure 7.2. The data fitting is usually performed in r-space, using a limited range of FT data to isolate certain contributions to the fit. In this thesis only contributions from the first single scattering path are taken into account. To set up a fitting model for the EXAFS data, one usually starts with an appropriate bulk structure, in this case Ag bulk (fcc structure with a lattice constant of $4.09\,\text{nm}$ [Dav25]). Some of the parameters in the EXAFS equation (6.6) are calculated *ab-initio* using the software package FEFF9 [Reh10], while others are found by least-square fitting to the experimental data [New01].

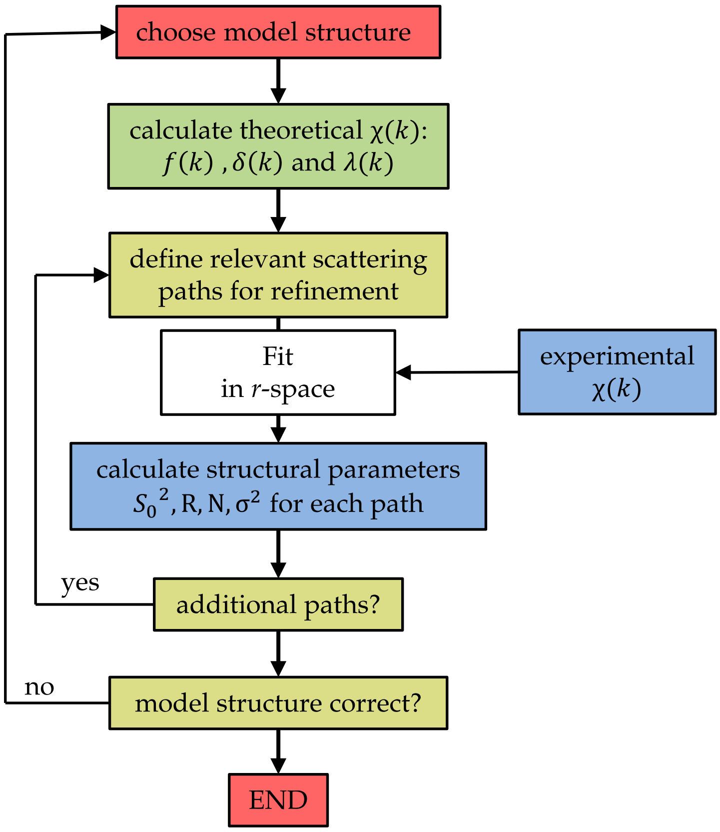

Figure 7.2: Fitting procedure of EXAFS data for an unknown structure.

For the *ab-initio* calculations the self-consistent multiple scattering code FEFF9 uses a list of atomic coordinates as input, which also contains information about the system (e.g. absorbing atom and absorption edge), as well as further parameters giving details of the calculation. FEFF calculates the electronic structure of the atoms surrounding the absorbing atom using a relativistic atomic potential approach. To reduce computing time a muffin-tin approximation is used. Afterwards the overlaps of the wave functions and the scattering phase shifts are calculated. Details on the impact of the internal calculation parameters are given in the FEFF documentation [Reh13]. In the end of the calculation FEFF returns the EXAFS contribution $\chi_j(k, p_j)$ for each path (single paths as well as multiple scattering paths). Each of the paths contributing to the modeled $\chi(k)$ has a set of parameters p_j, which are modified during the fit to match the data using conventional least-squares fitting with the FEFFIT code [New95] as implemented in LARCH. Further, FEFF weights the possible scattering paths according to how strong they influence the resulting EXAFS spectrum. Generally, single scattering paths have a higher impact and the shorter a scattering paths is the more important is it for the total spectrum.

Within the data fitting process the structural parameters S_0^2, n_i, R_i and σ_i are varied for each path. Additionally parameters can be constrained in order to reduce the number of parameters. While for experimental data E_0 is usually determined using the inflection point, FEFF chooses $k = 0$ to be at the Fermi energy E_F caused by the use of self-energy and complex scattering potentials [Reh10]. Thus, the energy shift ΔE_0 is included in the refinement for energy calibration.

In principle an unlimited number of paths, each containing the parameters p_j, can be used to model an EXAFS spectrum. However, experimental EXAFS data only contain a limited amount of information. The Nyquist theorem gives an estimation for the maximum number of parameters that can independently be fitted:

$$N_{\text{indp}} = \frac{2\Delta k \Delta R}{\pi} \tag{7.3}$$

Eq. (7.3) describes the ratio between the width of the fitting space $\Delta R = R_{\text{max}} - R_{\text{min}}$ and the resolution of the Fourier transformation $\Delta r = \frac{\pi}{2\Delta k} = \frac{\pi}{2(k_{\text{max}} - k_{\text{min}})}$. The number of independent points limits the number of parameters used in the fit. For the fits of the first coordination shell performed in this thesis ($\Delta k = 7\,\text{Å}^{-1}$, $\Delta R = 2.3\,\text{Å}$) the number of independent points is $N_{\text{indp}} \approx 10$. To achieve a reliable fit the parameters should be approximately half the number of independent points, which restricts the data fitting to the first coordination shell for the measured cluster spectra.

In order to quantify a fit mismatch, the statistical quantity of the $\mathcal{R}$-factor is used [Cal13]:

$$\mathcal{R} = \frac{\sum_{i=1}^{N} (\text{data}_i - \text{fit}_i)^2}{\sum_{i=1}^{N} (\text{data}_i)^2} \tag{7.4}$$

This value gives the deviation of the refinement of the model calculation from the experimental data, normalized to the experimental data. A value of $\mathcal{R} < 0.2$ denotes an acceptable fit to the data [Kon00].

7.2 Sample Aggregation Studied With EXAFS

7.2.1 Experimental Approach

In order to investigate structural changes during sample aggregation, EXAFS spectra for different phases of aggregation have been recorded using the setup introduced in section 6.4.3. Each measurement was performed at 250 K to avoid sample aggregation during the measurement, starting with separated Ag clusters with a diameter of 2 nm in the sample. To reach the next aggregation phase, the sample is warmed up to room temperature for several hours according to the time scales determined in section 5.2.2. The progress of aggregation is controlled via UV/Vis absorption spectroscopy (see section 7.2.2). Once the desired aggregation state is reached, the sample is cooled down to 250 K again to avoid further aggregation during the EXAFS measurement. Besides the separated clusters in sample

DO67, EXAFS spectra of two different phases of aggregation (denoted as *intermediate state* and *aggregated clusters*) have been investigated.

7.2.2 Radiation Damage

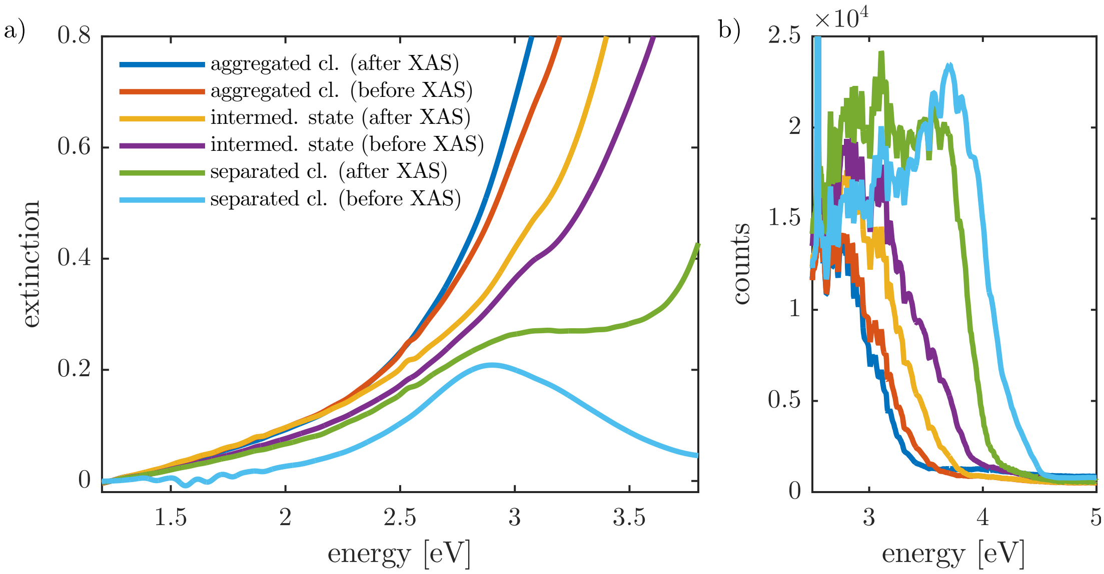

Figure 7.3: a) Development of the cluster plasmon monitored by UV/Vis absorption spectroscopy before and after each EXAFS measurement. b) Increased extinction due to modified cut-off wavelength caused by radiation damage.

The UV/Vis absorption spectra used to monitor the sample aggregation are shown in figure 7.3a). The cluster plasmon shape has remarkably changed after 5 hours of X-ray exposure. Although the left flank of the plasmon is still visible, the extinction is significantly increased above 3 eV. The sample is warmed up to and stored at room temperature for 80 minutes. The UV/Vis absorption spectrum has changed after that time, although the typical aggregation behavior presented in section 5.2.2 cannot be reproduced. This effect is even more pronounced after the measurement of the "intermediate aggregation state" (10 hours of X-ray exposure). The last EXAFS measurement ("aggregated clusters", 10 hours of X-ray exposure) is performed after the sample again aggregated at room temperature for another 80 minutes. After that no cluster plasmon can be recognized in the UV/Vis absorption spectrum.

The increase of the extinction after X-ray exposure can be explained by a radiation induced change of the sample. Figure 7.3b) shows the sample counts in the range between 200 and 600 nm (6.2 eV and 2 eV), from which the extinction is calculated using equation (4.49). Although the total counts cannot directly be compared to each other since a new reference spectrum is recorded before each measurement, figure 7.3b) clearly reveals an increased shift of the cut-off wavelength from 267 nm (4.65 eV) to 351 nm (3.5 eV) for increasing X-ray exposure time. The same effect has been seen for pure ionic liquid, that also has been placed into the temperature cell for 19.5 hours as shown in figure 7.4.

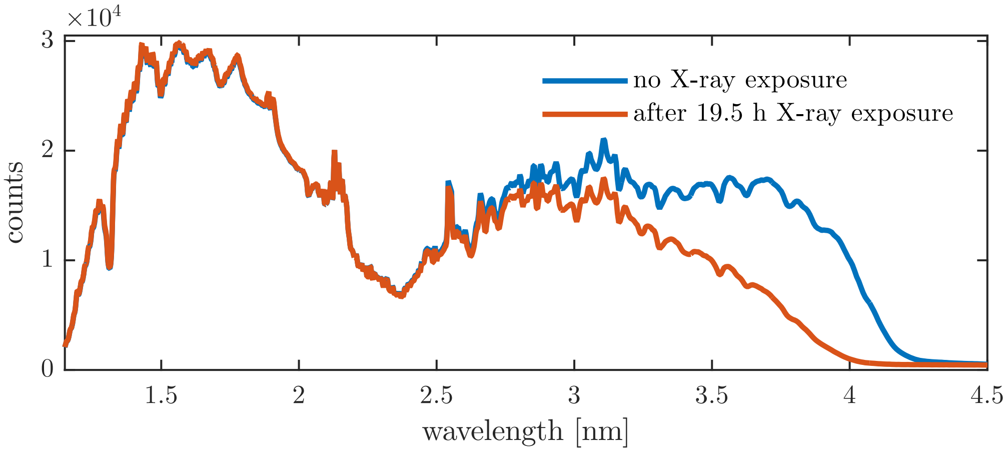

Figure 7.4: The shift of the cut-off wavelength to higher wavelengths also occurs for pure ionic liquid.

The long X-ray exposure times have been necessary due to the low amount of silver in the sample volume causing a low signal to noise ratio. Thus, during the entire aggregation experiment the sample has been exposed to the X-ray beam for 45 hours in total. Measurements performed during an earlier beamtime of Ag crystals in IL at the Ag L_2 edge (ID26, ESRF) revealed a beam-induced damage that became obvious in a discoloration of the sample [Eng14]. TEM images revealed the fragmentation of the clusters into nanoclusters, although the production TEM images of ionic liquid stabilized clusters has to be handled with care as already discussed in section 5.2. However, these results cannot be directly compared to the results obtained here since the energies of L_2- and K-edge significantly differ in energy (3.52 and 25.51 keV).

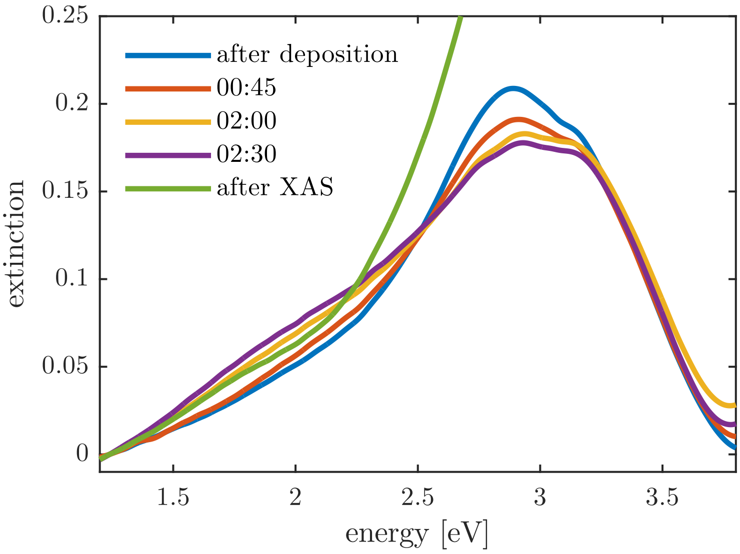

Figure 7.5: Aggregation monitored by UV/Vis absorption spectroscopy. All legend entries are given in *HH:MM*. After 02:30 the EXAFS measurement of the aggregated sample, denoted as "control experiment", is started.

The X-ray exposure seems to damage the ionic liquid. In order to ensure that changes in the EXAFS spectrum during aggregation are not erroneously occurring due to radiation damage, a control experiment has been performed. Clusters from the same sample, containing separated clusters, are filled into a cuvette and the sample aggregation is monitored using UV/Vis spectroscopy (see figure 7.5). Once the desired aggregation phase (comparable to the measurement of the "aggregated clusters") is reached, the sample is transferred into the EXAFS sample holder, cooled down to 250 K and a comparison EXAFS experiment is performed.

Figure 7.5 shows the sample aggregation as already discussed in section 5.2.1. After the XAS experiment the same radiation damage effect is observed. The analysis of the XAS data will show, if the radiation damage also influences the cluster structure of the sample.

7.2.3 EXAFS Fitting Results

Unfortunately the signal to noise ratio of the first aggregation phase ("2nd EXAFS") is too low for quantitative EXAFS analysis. Thus, this sample will later be discussed in section 7.2.6. Therefore in the following the designations "separated clusters" and "aggregated clusters" are used, corresponding to the 1st and 3rd EXAFS measurement shown in figure 7.3.

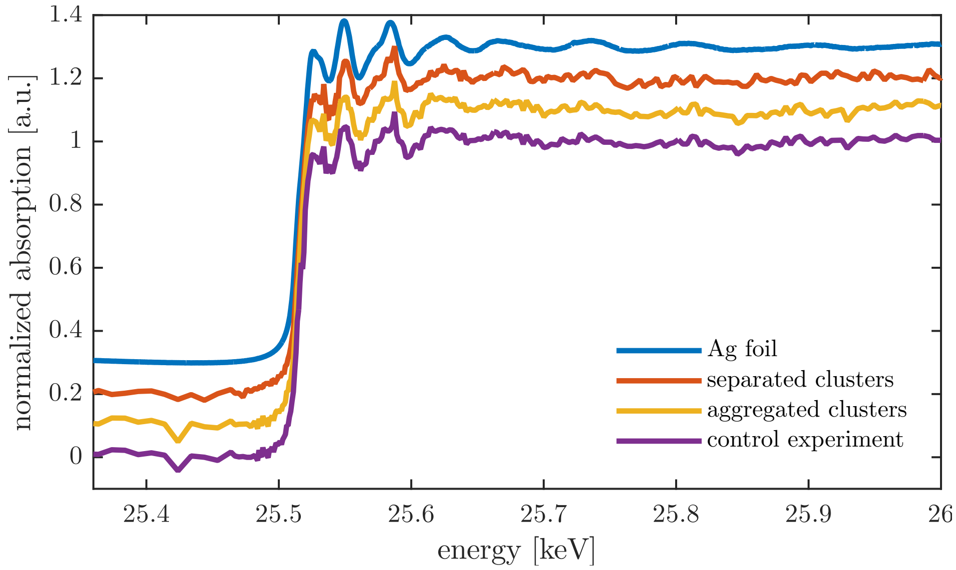

Figure 7.6: Merged XAS spectra for all measured samples. The spectra are shifted for reasons of clarity.

Figure 7.6 shows the measured absorption coefficient $\mu(E)$, normalized to 1 and shifted on the y-axis for reasons of clarity. During the normalization process (figure 7.1a)) the edge jump $\Delta\mu(E_0)$ is determined, which is proportional to the total amount of material in the sample [Van16]. While $\Delta\mu(E_0) = 8.4$ for the Ag reference foil, the edge step for the sample containing the separated clusters is 0.25 due to the low sample concentration. The edge step of the sample containing the aggregated clusters and of the control experiment is 0.23. Thus $\Delta\mu(E_0)$ does not significantly change during aggregation within the estimated error due to the fitting of pre-edge and normalization line. The fact that $\Delta\mu(E_0)$ does not change during aggregation means that the total amount of silver inside the sample does not change. As a consequence, no cluster material sediments during the aggregation as for example reported for mono-disperse Fe_3C nanoparticles in C_2MIM TfO or C_2MIM Bf_4 [Kha10a]. This is a hint for the formation of either larger bulk-like structures or the mentioned chain-like aggregates (see section 4.3.4).

Figure 7.7 shows the k^2-weighted EXAFS spectra in k-space for all mentioned samples after background removal according to the approach introduced in section 7.1.2. The amplitude of the oscillations is reduced for all cluster samples compared to the reference measurement. Due to the comparably large fraction of surface atoms with less neighbor atoms than bulk the overall coordination number (CN) of cluster spectra is expected to decrease. This can directly be seen in $\chi(k)$ because it is directly proportional to the coordination number n_i (see equation (6.6)). Slight differences between the spectra of separated and aggregated clusters can be detected in k-space and the spectra of the aggregated clusters and of the control experiment (yellow and purple lines) look similar.

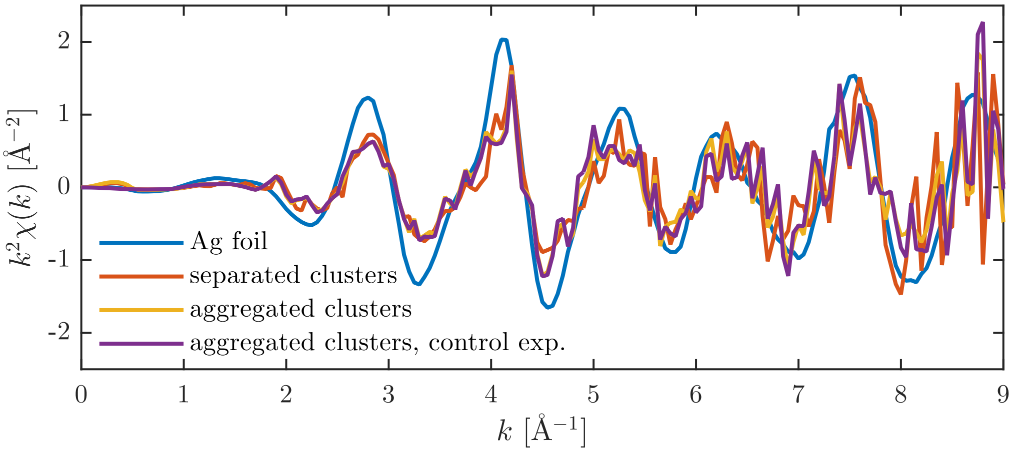

Figure 7.7: k^2-weighted EXAFS spectrum for separated and aggregated clusters compared to spectrum of an Ag foil. The slightly reduced amplitude of the cluster spectra suggests a reduced coordination number as expected for small clusters.

Figure 7.8 (black, solid lines) shows the spectra Fourier transformed in the k range from 2.0 Å to 9.0 Å using a Hannig type window (see figure 7.1c)). In the fitting process the structural parameters R_1 and n_1 of the first coordination shell are determined. At first the EXAFS data of the Ag foil are fitted in r-space (r_{min}=1.2 Å to r_{max}=3.5 Å) to the first coordination shell of Ag bulk according to the approach introduced in section 7.1.4.

The value ΔE_0 is determined to account for the phase difference between the experimental and theoretical backscattering paths. For all later refinements the same Ag bulk fitting model is used and thus $\Delta E_0 = -3.48$ eV is set to the value obtained from the Ag bulk fit for every fit.

As already mentioned, the coordination number is decreased for small clusters. Since S_0^2 is multiplied by n_i in the EXAFS equation for each scattering path, it is pointless to fit both parameters because they are 100% correlated and thus indistinguishable in a statistical sense [Rav07]. Therefore S_0^2, which is a material dependent parameter, is set to a fixed value obtained from the bulk Ag refinement ($S_0^2 = 0.97$). The path degeneration is forced to be 1 and path amplitude is set to $S_0^2 \cdot n_i$, while n_i is allowed to vary in the fit.

Figure 7.8a) shows the results of fitting the first single scattering path (red dashed lines) of Ag bulk to the data, while the figures 7.8b)-d) present the fits to the cluster data. The R-factors of all fits are well below 0.2. In order to ensure the reliability of the results, r-space refinements have been carried out in both k^2- and k^3-weighting (not shown here) and the results were consistent.

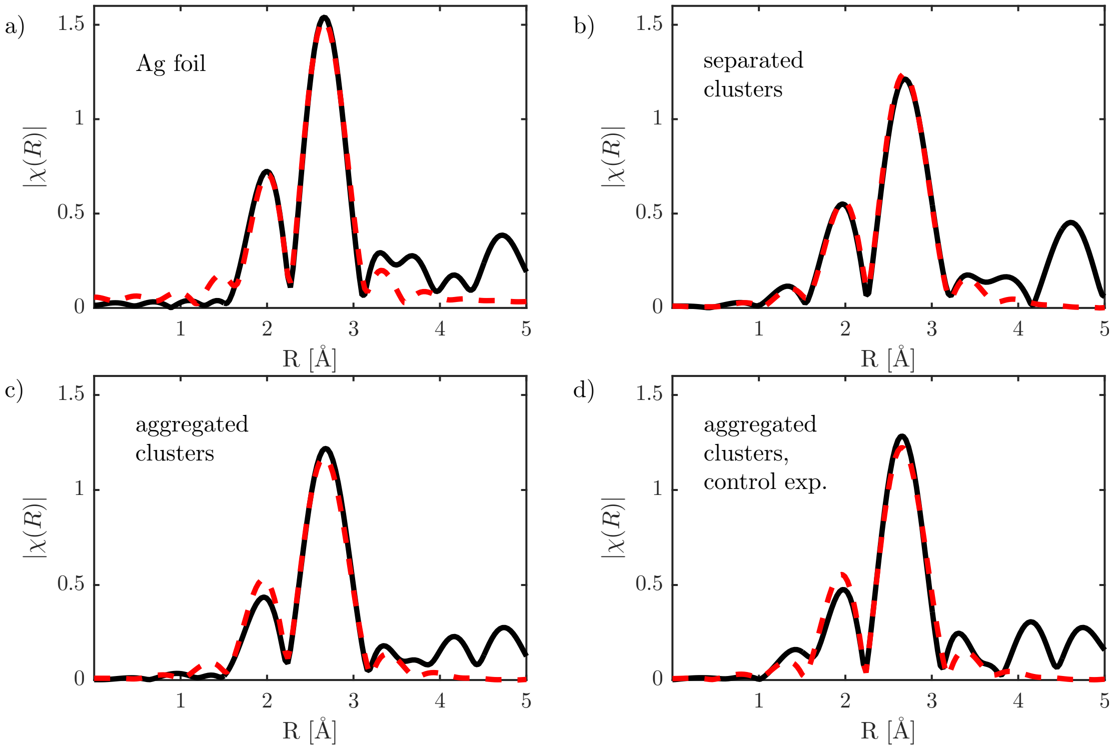

Figure 7.8: Fourier transform (solid lines) of the data and fitting (dashed lines) of the first single scattering path of Ag bulk: a) Ag foil, b) separated clusters, c) aggregated clusters, d) control experiment

Table 7.1 summarizes the refinement of the structural parameters of the fits shown in figure 7.8. The numbers in parenthesis give the uncertainties of the fit.

	Ag foil	separated clusters	aggregated clusters	aggregated clusters, control exp.
R	2.86 ± 0.01	2.83 ± 0.01	2.86 ± 0.01	2.86 ± 0.01
σ^2 [Å^2]	0.012 ± 0.001	0.009 ± 0.001	0.008 ± 0.001	0.008 ± 0.001
C_3 [10^{-3} Å^3]	0.012 ± 0.001	-0.5 ± 0.2	0.1 ± 0.3	0.2 ± 0.4
n_1	12 (fixed)	9.2 ± 0.9	10.6 ± 1.1	9.0 ± 1.4

Table 7.1: Determination of the structural parameters of the first coordination shell for the investigated XAS spectra.

7.2.4 Bond Length Contraction

For the Ag foil a first shell bond length of (2.86 ± 0.01) Å was obtained from the fit; this value differs from the one given by the model structure (2.89 Å), which has been obtained by diffraction [Dav25]. The reason for this is a slightly asymmetric bond length distribution for bulk silver in the first coordination shell that cannot be accounted for by including a cumulant to the fit C_3. Timoshenko *et al.* observed a similar behavior for gold and were able to account for the asymmetry by performing Reverse Monte Carlo simulations [Tim17b]. In contrast to the bulk value a reduced first shell bond length of (2.83 ± 0.01) Å was found for the sample containing separated 2 nm Ag clusters. This bond length contraction is a well-known effect [Apa79] and can be explained by a redistribution of charges that scales with the cluster size. Since the number of nearest neighbors at the cluster surface is significantly smaller than in bulk, resulting in reduced repulsive interactions between the non-bonded electron pairs [Gor77; Jon75]. The bond length contraction of the separated 2 nm Ag clusters determined in this thesis is 1.05% (relative to the bulk value), which is in good agreement with measured lattice contractions of Au nanoparticles determined by Zhang *et al.* (1.1% for Au nanoparticles with a diameter of 2.4 nm) [Zha03].

For the aggregated clusters and the control sample the fit revealed a first shell bond length of 2.86 Å suggesting a relaxation of the interatomic distance back towards the bulk value. The bond length contraction becomes also visible in the back-transform of $\chi(R)$ to a filtered $\tilde{\chi}(k)$:

$$\tilde{\chi}(k) = \frac{2}{\sqrt{2\pi}} \int_{R_{\text{min}}}^{R_{\text{max}}} \chi(R) e^{-2kR} \, \mathrm{d}R \tag{7.5}$$

This process is also known as Fourier filtering since it allows to isolate certain frequencies or distances, respectively. Figure 7.9 shows the Fourier filtered $\tilde{\chi}(k)$ calculated using equation 7.5 with $R_{\text{min}} = 1.2$ Å and $R_{\text{min}} = 3.5$ Å. The oscillation of the spectra of the separated clusters becomes further apart in k, which is due to the contracted Ag-Ag bond [Zha03].

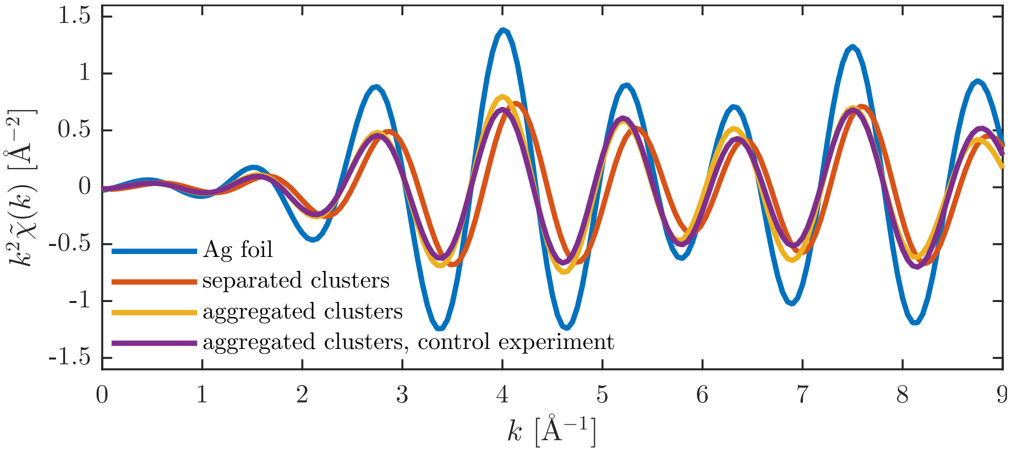

Figure 7.9: Fourier backtransform of the first coordination shell ($R_{\text{min}} = 1.2$ Å to $R_{\text{min}} = 3.5$ Å).

7.2.5 Coordination Number

In contrast to the CN of fcc bulk ($n_1 = 12$) the decrease of the coordination number of clusters is a consequence of the fact that the surface atoms of a cluster are having fewer neighboring atoms (see figure 7.10), hence causing the overall coordination number to decrease.

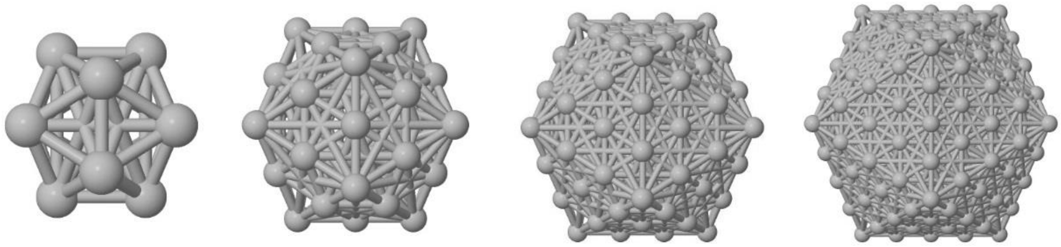

$N_1 = 13$
92.3% surface

$N_2 = 55$
76.4% surface

$N_3 = 147$
62.6% surface

$N_4 = 309$
52.4% surface

Figure 7.10: Mackay icosahedra with k closed shells with N_k atoms (figure generated using Jmol [Han10]). Smaller clusters have a larger surface to volume fraction than larger ones.

Assuming an hexagonal packing of the surface atoms, for a cluster with radius R the total number of atoms N and the number of surface atoms N_{surf} can be calculated by

$$N = \frac{V_{\text{cluster}}}{V_{\text{atom}}} = \frac{\frac{4}{3}\pi R^3}{5.66 r^3} \quad \text{and} \quad N_{\text{surf}} = \frac{A_{\text{cluster}}}{A_{\text{atom}}} = \frac{4\pi R^2}{3.46 r^2} \tag{7.6}$$

with the atom radius of silver $r = 0.1445\,\text{nm}$.

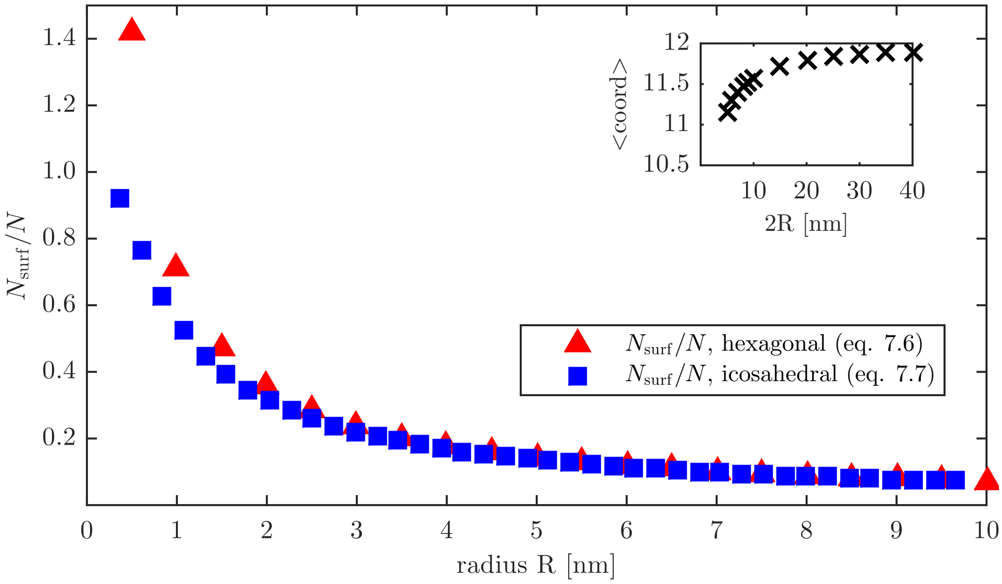

Figure 7.11: Fraction of surface atoms depends on the cluster size. The triangles show the approximation of N/N_{surf} for hexagonal close-packed atoms at the surface. The squares show N/N_{surf} for the Mackay icosahedra. Both approaches are similar for large R. The inset shows the average CN calculated using equation (7.9) for large clusters.

However, this approach fails for small clusters as shown in figure 7.11, where the fraction $N/N_{\text{surf}} > 1$. Thus, icosahedral Mackay clusters with hexagonally packed surface facets are considered, which are energetically favored for small clusters due to their fivefold symmetry. It could be shown that small icosahedral clusters with k closed shells are particularly stable (geometric magic clusters, see figure 7.10) consisting of N_k atoms [Mac62; Ech81]. The kth shell consists of $10k^2 - 2$ atoms. The surface to volume ratio can thus be calculated using

$$\left(\frac{N_{\text{surf}}}{N}\right)_k = \frac{N_k - N_{k-1}}{N_k} \tag{7.7}$$

with $N_0 = 1$. The cluster radius is given by

$$R_k = \left(\frac{3}{4\pi} N_k V_{\text{atom}}\right)^{1/3}. \tag{7.8}$$

This approach gives the correct limit $N_{\text{surf}}/N \to 1$ for small clusters. For larger clusters both formulations yield the same N_{surf}/N.

Based on these considerations the average coordination number for clusters of different sizes can be estimated. Assuming 12 nearest neighbors for the inner atoms in the cluster and 9 nearest neighbors at the hexagonal packed cluster surface, the average coordination number is of the first coordination shell is given by

$$\begin{aligned}\langle \text{coord}_{\text{hex}} \rangle &= \frac{12 \cdot (N - N_{\text{surf}}) + 9 \cdot N_{\text{surf}}}{N} \\ &= 12 - 3 \cdot \frac{N_{\text{surf}}}{N}.\end{aligned} \tag{7.9}$$

For icosahedral clusters the average coordination number of the first coordination shell can be calculated by counting the nearest neighbors depending on their position at the cluster surface (cnf. figure 7.10). Atoms in the "inner shell" of an icosahedron have 12 nearest neighbors. All nearest neighbors are summed up and divided by the total number N_k of atoms. The average coordination number $\langle \text{coord}_{\text{ico}} \rangle$ is given in table 7.2 together with the corresponding N_k and the radii calculated using equation (7.8).

k	N_k	R_k [nm]	$\langle \text{coord}_{\text{ico}} \rangle$
1	13	0.3756	6.46
2	55	0.6075	8.51
3	147	0.8431	9.47
4	309	1.0800	10.02
5	561	1.3175	10.62

Table 7.2: Coordination number for small icosahedra consisting of N_k atoms.

Using this preliminary considerations, now the obtained CNs of the first coordination shell can be discussed. The fitted value $n_1 = 9.2 \pm 0.9$ for the separated clusters ($2R = 2 \pm 0.6$ nm) is in accordance with the coordination numbers for this cluster size given in table 7.2, that were also confirmed in other experimental studies [Jen99; Pri12].

For small clusters different minimum-energy configurations besides icosahedra have been proposed as structural motifs, e.g. truncated octahedral or cuboctahedral morphologies. These configurations have been investigated by Glasner *et al.* concerning their size dependent coordination numbers [Gla07].

If clusters coalesce to large bulk-like structures with several $10\,\text{nm}$ diameter, this becomes apparent in an increase of the coordination number. For example, a cluster with a diameter of 40 nm has a small surface to volume ratio of $\approx \frac{7\cdot 10^4}{2\cdot 10^6} = 3.5\%$ and thus, according to equation 7.9, an average coordination number of 11.9. However, the results of the EXAFS fitting revealed a coordination number of 10.6 ± 1.1, which is significantly smaller, even within the experimental error bar. From this result a coalescence of the clusters to particles of several $10\,\text{nm}$ diameter can be excluded, although the shape of the UV/Vis absorption spectrum suggests this shape as a possible explanation for the measured extinction spectra (see section 5.2.2). However, the larger error bars of the CN in the EXAFS analysis is due to the limited k-range available for data fitting, which yields to a comparably large error of $S_0^2 = 0.97 \pm 0.07$. Therefore the EXAFS analysis is complemented by XANES analysis introduced in the next section to evaluate the results of the EXAFS measurements.

7.2.6 Analysis of the XANES Data

In order to support the results obtained by common EXAFS fitting presented in table 7.1 also the XANES up to $100\,\text{eV}$ above the absorption edge can be investigated. The XANES signal also contains information about the nearest neighbors distances and bond angles. Differences in cluster size and shape also affect the XANES as shown for $2\,\text{nm}$ Ag clusters embedded in PDMS [Roe16]. Further, XANES does not suffer from the data quality limitations. However, the structural information cannot easily be extracted from the XANES by fitting to an analytical equation as given for the EXAFS region (equation (6.6)).

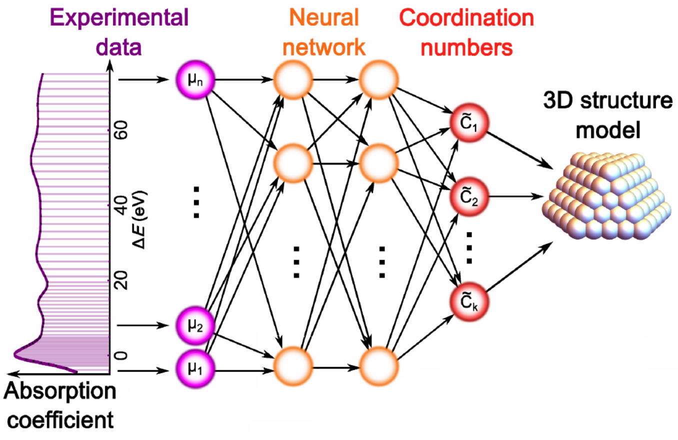

Figure 7.12: Neuronal network based analysis of experimental XANES data in order to determine coordination numbers [Tim17c].

To decipher the 3D structure of nanoparticles a recently developed supervised machine learning based XANES analysis approach was employed to analyze the recorded cluster spectra. This method was developed by Timoshenko *et al.* and uses *ab-initio* an artificial neural network for XANES analysis [Tim17c]. XANES calculations using the FEFF [Reh10] and FDMNES [Bun09] codes for different nanoparticle sizes and shapes [Gla07], which are well-defined with known CN, are used as training data sets for the artificial neural networks. Due to their limited size clusters have non-equivalent absorbing sites, each yielding a different XANES. Thus, experimental XANES is an average of all these contributions [Hof12; Baz97]. Figure 7.12 shows the neural network that yields a non-linear relation between the spectral features of the XANES and the coordination number, that in turn characterizes the cluster size and shape.

This approach has successfully been validated for the first four coordination shell of experimental XANES data of supported Pt clusters at the Pt L_3-edge, that already had been pre-characterized using TEM and EXAFS [San09; Rol10a; Rol10b]. One major advantage of this approach is that it does not require high quality EXAFS data, that is in particular difficult to obtain for dilute samples.

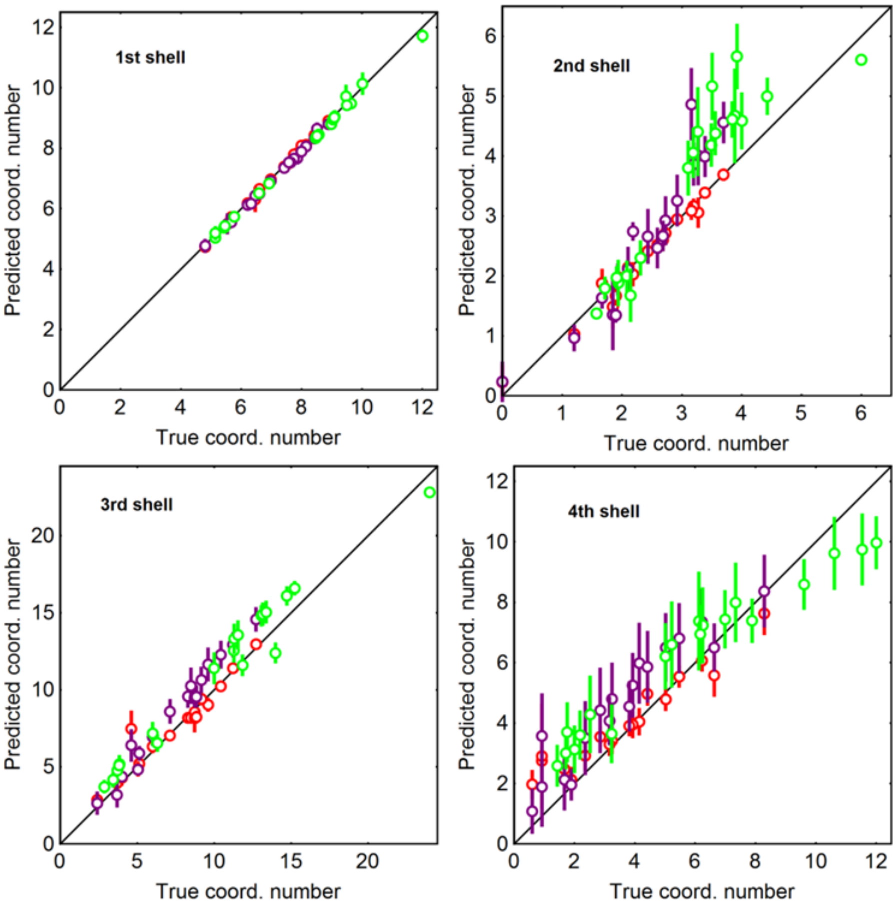

Figure 7.13: Validation of the neural network calculated for the XANES Ag K-edge. Different colors represent different datasets. The solid line serves as a guide to the eye. The figure is provided by J. Timoshenko [Tim17a].

Both *ab-initio* codes FEFF and FDMNES work reasonably well for Ag bulk and are in agreement with the experimental data. For this thesis the neural network has been trained using theoretical Ag K-edge XANES spectra of different sized and formed nanoparticles. The following shapes have been used: octahedral, truncated octahedral, cuboctahedral, cubic (with fcc-type structure and also truncated with additional (110) or (111) planes) as well as icosahedral and hcp structures. For all these structures a nearest-neighbor distance of $2.89\,\text{Å}$ (in accordance with the bulk value [Dav25]) has been chosen. The neural network is then validated, relying on theoretical, particle averages XANES data calculated using FEFF and FDMNES, that yield the "true" CNs. As a matter of course different structures have been used for neural network training and validation. Figure 7.13 shows the true CNs versus the CNs predicted by the neural network. The error bars are obtained by different neural networks trained on different datasets.

Figure 7.14 shows Ag K-edge XANES spectra and corresponding particle-averaged coordination numbers for Ag clusters consisting of 10 to 185 atoms for one specific cluster shape. It is clearly visible that the spectrum of the Ag_{10} clusters shows less features than spectra of clusters with more atoms. Hence also the XANES is sensitive to the surface to volume ratio of a cluster.

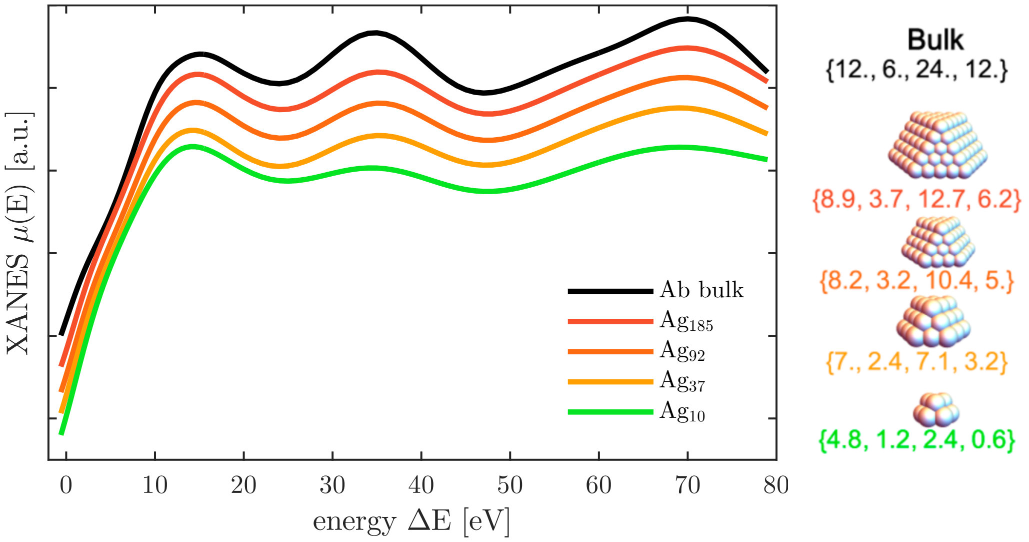

Figure 7.14: Ag K-edge XANES spectra and particle-averaged coordination numbers for Ag clusters of different size compared to Ag bulk [Tim17a].

The neural network analysis was focused on the first coordination shell since this information is usually sufficient to investigate the cluster size. In table 7.3 the results obtained by neural network XANES analysis are compared to the results of conventional EXAFS analysis discussed in the previous section 7.2.5. Table 7.3 also includes the already mentioned sample denoted as "intermediate aggregation state". However, the signal to noise ratio is too low, prohibiting conventional EXAFS fitting in this case. Since the neural network XANES analysis only includes data up to 100 eV above the absorption edge, also samples with poor data quality could be analyzed.

Besides the samples containing Ag clusters in ionic liquids also the XAFS data of a sample containing Ag clusters prepared by DNA templated synthesis [Gwi08; ONe09] are investigated. The Ag K edge spectra were recorded by Dr. D. Nykypanchuk from the Center for Functional Nanomaterials at Brookhaven National Laboratory at the X18A beamline of NSLS at Brookhaven National Laboratory. The high quality EXAFS data were provided by Timoshenko *et al.* [Tim17a]. The data are used to ensure the neural network works correctly for a broader range of particle sizes.

sample	n_1 (EXAFS)	n_1 (XANES)
Ag foil	12 (fixed)	11.7 ± 0.2
separated clusters	9.2 ± 0.9	8.0 ± 0.6
intermediate aggregation state	*not available*	8.3 ± 0.3
aggregated clusters	10.6 ± 1.1	9.0 ± 0.2
aggregated clusters, control exp.	9.0 ± 1.4	8.7 ± 0.3
Ag clusters, DNA synthesis	5.0 ± 1.6	5 ± 1

Table 7.3: Comparison of the first coordination shell CNs obtained by common EXAFS analysis (cf. section 7.2.5) and neural network XANES analysis.

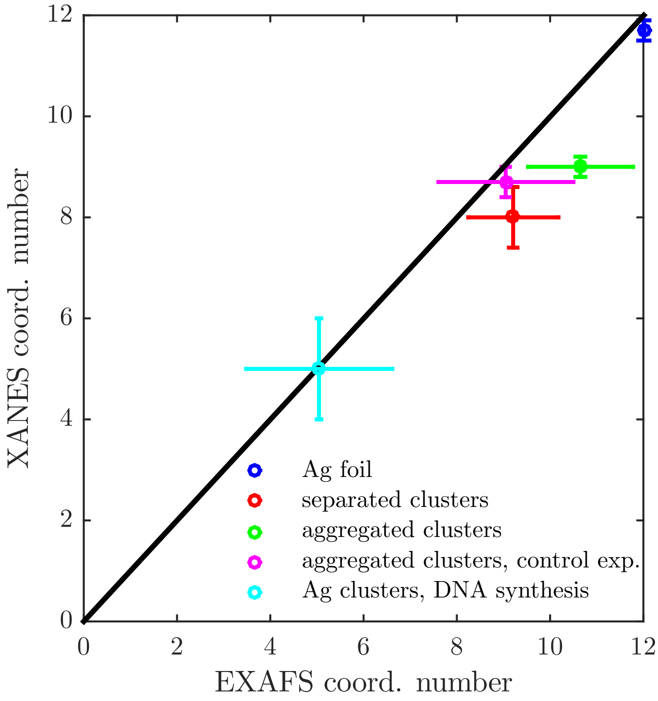

Figure 7.15: Comparison of the first shell coordination number n_1 obtained by conventional EXAFS and neural network XANES analysis.

The results of both methods are visualized in figure 7.15. Again the black line serves as a guide to the eye for perfect accordance of both methods. For the samples "separated clusters" → "intermediate aggregation state" → "aggregated clusters" a gradual increase of the CN from 8.0 to 9.0 is found. Both EXAFS and XANES analysis suggest that the CNs of all cluster samples are well below the value found for the Ag foil. Thus the cluster size remains close to 2 nm, excluding the presence of large nanoparticles with a diameter of several 10 nm. Note that no error bar is given for the EXAFS coordination number of the Ag foil because it was fixed to 12 during the fit while determining the value for S_0^2. Thus the error bars for the coordination number fitting of the other samples derive from the error of S_0^2 from the bulk fit.

By extending the EXAFS analysis to more than one coordination shell it would in principle be possible to differentiate between different cluster shapes (e.g. cuboctahedral, icosahedral, truncated octahedron) as demonstrated in [Tim17c], but in this thesis the analysis is restricted to the first coordination shell due to the limited available k-range. Further, the analysis of the aggregated clusters is difficult due to the expected broad distribution of particle size and shape.

7.3 Structure of Clusters Aggregated During Deposition

In section 5.1.4 sample *DO54*, containing $83.7\,\mu\text{g}$ Ag clusters, has been discussed. The *in-situ* spectra show aggregation already during deposition. In this section the corresponding EXAFS spectra will be analyzed. The measurement has been preformed in line to the approach introduced in the previous section 7.2.1. The sample is filled into the sample holder, mounted in the temperature cell and cooled down to $250\,\text{K}$ to avoid further aggregation. Compared to the samples discussed in the previous section sample *DO54* contains approximately ten times the amount of cluster material. Although the fluorescence line fitting algorithm does not improve the quality of the spectra here, the fitting routine has been applied.

After merging the recorded spectra, the edge step is determined during data reduction. Since the $\Delta\mu_0(E)$ is proportional to the amount of silver inside the sample, a value of $\approx \Delta\mu_0(E) = 10 \cdot 0.25$ is expected. This is significantly less than $\Delta\mu_0(E) = 0.15$, which is the value obtained for sample *DO54*. Obviously some cluster material seems to have sedimented during aggregation.

The fitting process of the first coordination shell is similar to the description in section 7.2.3. However, there are remarkable differences to the previous discussed samples, aggregated at room temperatures.

A first shell Ag-Ag bond length of $(2.81 \pm 0.01)\,\text{Å}$ is obtained, being significantly smaller than for the separated and the aggregated clusters as well as the Ag bulk foil. Further, the coordination number is found to be $n_1 = 10.08 \pm 1.36$.

The XANES has also been analyzed using the same neuronal network trained with the models introduced in section 7.2.6. However, this algorithm reveals $n_1 = 7.8 \pm 0.7$, which deviates strongly from the value obtained by common EXAFS fitting. This case shows the common drawback of all supervised machine learning methods: their application fails for data, which is not similar to those used for training, e.g. if the interatomic distance differs significantly from the ones used in the training data set (2.89 Å).

However, the fit of the third cumulant reveals $C_3 = (0.9 \pm 0.3) \cdot 10^{-3}\,\text{Å}^3$, which is significantly larger than the values obtained for the other cluster samples given in table 7.1, which might be a hint that the cumulant expansion does not converge well because the distribution is too broad. In order to solve that problem more than one path would have to be considered, which is not possible due to the limited k-range.

7.4 Setup for Simultaneous X-ray and UV/Vis Absorption Spectroscopy

An additional experiment has been set up at beamline P64, realizing a simultaneous measurement of XAS and UV/Vis Absorption spectroscopy. By adjusting the sample temperature, the aggregation speed can be controlled. A pumping circuit needs to be setup to measure the cluster plasmon and XAS of the same portion of the sample. Another limitation is, that only 15 ml of a sample can be produced during one deposition, which also limits the volume of the tubes used in the pumping circuit. For sample transfer within the circuit a peristaltic pump is used.

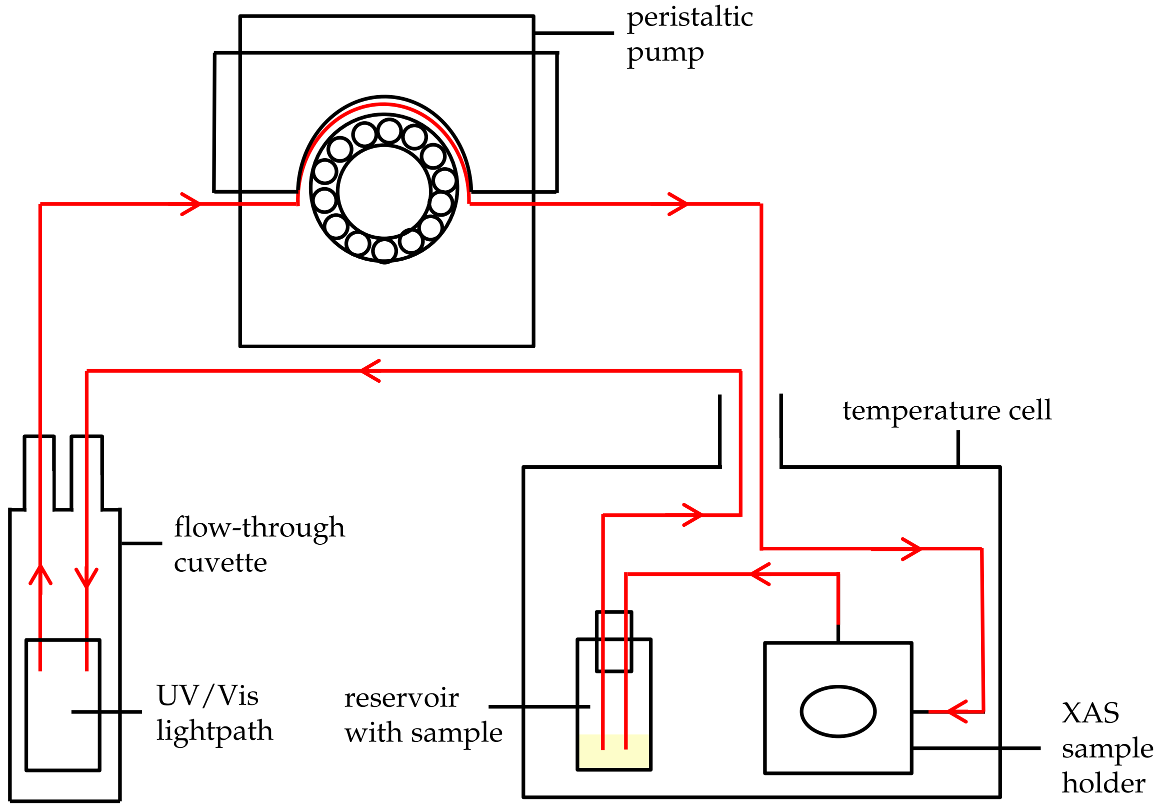

Figure 7.16: Basic setup of the pumping circuit for simultaneous UV/Vis and X-ray absorption spectroscopy measurements.

A modified sample holder (compare figure 6.11) with two capillary tubes (diameter 1.1 mm, wall thickness 0.25 mm) are used. The sample is pumped through a silica glass flow-through cuvette (optical path length 1 cm, volume 450 µl). The intake and drain outlet of the flow-through cuvette have a outer diameter of 3.5 mm. Sample holder and flow-through cuvette are connected using Tygon® pump tubes. To fill the tubes the circuit is interrupted between sample holder and flow-through cuvette. Both ends of the tubes are connected with a reservoir, containing the rest of the sample. Using this approach possible bubbles can be removed from the circuit.

During beamtime the sample needs to be cooled and the sample temperature should be maintained to decelerate aggregation. Therefore the XAS cell, connected with the pump tubes is placed in the temperature cell, cooled by a circulation thermostat down to $\approx -4\,°\mathrm{C}$. The remaining parts of the pumping circuit (peristaltic pump, flow-through cuvette with cuvette holder, reservoir and fiber optic cables) are placed in a polystyrene box equipped with two water-cooled copper plates. Thus the reservoir has a temperature of $2\,°\mathrm{C}$. The pump tubes connecting the XAS cell and flow-through cuvette are isolated as far as possible to avoid sample heating during the time the sample is pumped through the connecting tubes. The pumping speed in the tube is approx. 1 cm/s.

During the simultaneous UV/Vis and X-ray absorption spectroscopy experiment the extinction was recorded every 10 minutes. Figure 7.17a) shows the development of the cluster plasmon during the XAS experiment, which lasted 33 hours.

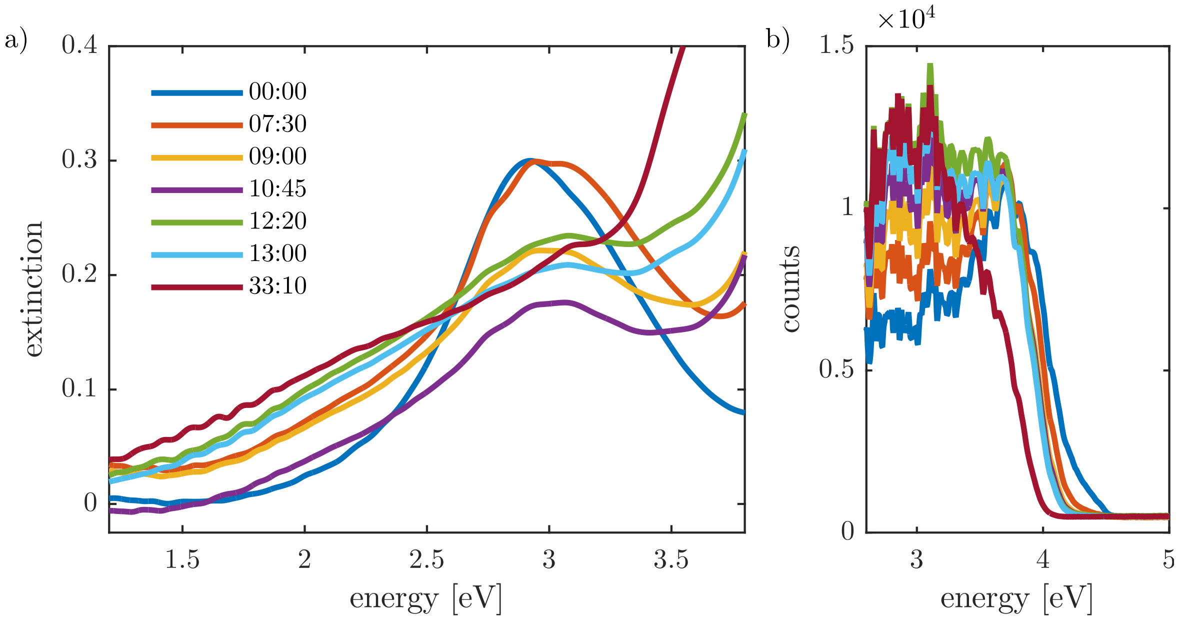

Figure 7.17: a) Sample aggregation during the simultaneous UV/Vis absorption spectroscopy and EXAFS experiment. The legend denotes the time during the experiment in *HH:MM*. b) Radiation damage induced shift of the cut-off wavelength to lower energies.

The phases of aggregation defined in section 5.2.2 for the sample stored in the refrigerator cannot be found in figure 7.17. On the one hand this could be caused by the radiation damage induced changes in the optical spectrum (figure 7.17b)). On the other hand is the aggregation accelerated during this experiment. Although the sample in the sample holder and the reservoir has a temperature well below the refrigerator temperature, a proper cooling of the sample inside the connecting tubes could not be guaranteed. Thus, after 12 hours a cluster plasmon (green line) cannot clearly be recognized.

Due to the low concentration of silver inside the sample at least 10 spectra are required for merging, which corresponds to a total measurement time of 5 hours. Using the experimental setup in its current condition does not allow to record corresponding EXAFS spectra with sufficient quality. Thus, no EXAFS results are presented here. Although very CPU consuming, an idea would be to evaluate the XANES range using the neural network analsis as introduced in section 7.2.6, since this method does not require high quality EXAFS data.

Cooling the sample to lower temperatures (in order to further slow down the aggregation process) would require an alternative to a water cooling circuit. However, this would not solve the problem concerning the insufficient cooling of the connecting tubes. Further, a colder samples temperature results in a lower sample viscosity, causing problems in the sample transportation process through the tubes.

However, in general the setup for simultaneous UV/Vis and X-ray absorption spectroscopy allows to study cluster structure changes *in-situ* (e.g. after adding reagents) can be a powerful tool to explore the emerging field of nanoparticles immersed in ionic liquids.

Chapter 8

Summary and Outlook

In this thesis the stability and aggregation behavior of preformed silver clusters deposited into C_4MIM PF_6, a room temperature ionic liquid, have been investigated. Ionic liquids are currently under discussion for being a suitable electrosteric stabilizer for clusters due to their ionic nature and their asymmetric structure. However, their stabilizing mechanism and the long-term stability is controversially discussed. In this thesis a new experimental approach of using preformed 2 nm silver clusters for deposition into C_4MIM PF_6 has been introduced. This approach differs from all other sample production methods reported in literature with cluster growth in the ionic liquid where the processes of formation of new particles and particle aggregation are indistinguishably taking place simultaneously, while using preformed clusters allows to assign structural changes in the sample to aggregation. Sample structure and aggregation were investigated by combining two complementary experimental techniques: UV/Vis absorption spectroscopy and X-ray absorption spectroscopy.

In a series of experiments optimal deposition parameters have been obtained to allow the production of samples containing macroscopic amounts of silver clusters up to a concentration of 10 µg/ml.

The interaction between the ionic liquid and the deposited Ag clusters can be accessed via the peak position and peak width of the cluster plasmon resonance in the *in-situ* UV/Vis absorption spectra recorded during cluster deposition (section 5.1.1).

Preformed clusters seem to be less sensitive to external influences like the water content of their environment compared to cluster growth in the ionic liquid for which many studies revealed a significant destabilization, if the water content of the sample was increased. Due to the low pressure during cluster deposition compared to the pressure used during a sputtering deposition and the complete formation of the cluster before deposition the cluster seems to be protected against those influences.

In all performed experiments storage at room temperature leads to sample aggregation within 24 hours. In section 5.2.2 was found that the aggregation process can significantly be slowed down by cooling the sample during storage. For storage temperatures below the glass transition temperature ($T_g = -76\,°\mathrm{C}$) the sample aggregation can completely be stopped. A repeated warming of the sample over the melting temperature ($T_m = 11\,°\mathrm{C}$)

and subsequent cooling with liquid nitrogen does not affect sample stability. This study has shown that the improved sample stability at low storage temperatures can be explained using diffusion limited coagulation model assuming temperature independent coagulation probabilities. It turned out that the suppression of the Brownian motion due to the significantly increased viscosity of cold ionic liquids is the main contributing effect concerning sample stability.

The comparison between the measured UV/Vis absorption spectra and Generalized Mie Theory calculations of various aggregate formations (section 4.3.4) led to the assumption that either linear chains of aggregates are formed or that the clusters coalesce to larger particles with a diameter of several 10 nm. However, it is not possible to differentiate between cluster agglomeration and cluster coalescence. Thus X-ray absorption spectroscopy measurements have been performed at beamline P64 (DESY, Hamburg) in order to resolve the sample structure during aggregation using a custom built, cooled sample holder. Analyzing the fine structure (EXAFS) of those measurements enables the determination of the coordination number and nearest neighbor distances, at least for the first coordination shell.

Those experiments presented in section 7.2 revealed that the first coordination shell of separated clusters is slightly compressed by 1.05%. Further, the coordination number is decreased to 8 (compared to 12 for an fcc structure). Both values are typical for 2 nm clusters due to the high surface to volume ratio ($\approx 50\%$), again verifying that the clusters stay separated in the ionic liquid while being stored in liquid nitrogen. After aggregation, which has been monitored by UV/Vis absorption spectroscopy, a relaxation of the interatomic distance of the first coordination shell was observed, but no significant increase of the coordination number was observed as it would be expected for a cluster with several 10 nm diameter. An independent neural network based analysis of the near edge spectrum (XANES) confirms the results for the coordination number obtained by EXAFS fitting. Thus, by combining the experimental results of UV/Vis and X-ray absorption spectroscopy the coalescence to very large particles can be excluded. The Generalized Mie Theory calculations suggest a chain-like arrangement of the clusters during aggregation, in which the original single cluster size of 2 nm remains unchanged.

Besides $C_4MIM\ PF_6$ also other ionic liquids have been investigated in section 5.3. The work was focused to imidazolium-based ionic liquids to enable the comparison with literature. Besides a variation of the alkyl chain length also the anions were exchanged. Depending on its composition, the properties of an ionic liquid can vary significantly. The first results of cluster depositions into other ionic liquids were presented, revealing that also $C_4MIM\ BF_4$ and $C_4MIM\ Tf_2N$ are suitable for the production of stable samples, while clusters in C_4MIM DCA are unstable. The mixture of clusters and $C_8MIM\ PF_6$ is complicated due to the high viscosity of the ionic liquid. However, a systematic study also concerning longterm and temperature-dependent stability is still pending. In interesting approach would be to heat the highly viscous ionic liquid $C_8MIM\ PF_6$ to approx. 40 °C [Har06] as shown in 5.1.3 to lower its viscosity, improving the mixing process. A subsequent cooling to room temperature or even lower (as discussed in section 5.2.2) could improve sample stability.

EXAFS spectra with improved signal to noise ratio should be recorded to enlarge the k-space available for fitting. Thus, it would be possible to determine the coordination numbers of the second and third coordination shell, enabling the possibility to reconstruct the 3D cluster structure. The structure determination of an aggregated sample is hampered by the fact that the size distribution is broadened due to the presence of separated and diversely formed aggregated clusters as it is also the case for the interpretation of UV/Vis absorption spectra.

Further, THECLA's ability to also produce gold clusters [Hil01a] should be used to investigate ionic liquid stabilized gold clusters. UV/Vis and X-ray absorption spectroscopy measurements similar to those presented in this thesis should be performed. Sputtering experiments carried out by Alexander Kononov reveal a delayed formation of gold nanoparticles in C_4MIM PF_6, which may be a hint for different diffusion behavior, which directly should influence sample aggregation time scales. The approach of cluster preformation in the gas phase can be extended to different materials or even alloys.

Bibliography

[Abe07] S. Z. E. Abedin, M. Pölleth, S. A. Meiss, J. Janek, and F. Endres. "Ionic liquids as green electrolytes for the electrodeposition of nanomaterials". *Green Chem.* **9** (2007): 549–553.

[Als11] J. Als-Nielsen and D. McMorrow. "Bibliography". In: *Elements of Modern X-ray Physics*. Hoboken, NJ, USA: John Wiley & Sons, Inc., 2011, 403–406. ISBN: 9780470973950.

[AlT14] M. S. AlTuwaim, K. H. A. E. Alkhaldi, A. S. Al-Jimaz, and A. A. Mohammad. "Temperature Dependence of Physicochemical Properties of Imidazolium-, Pyrolidinium-, and Phosphonium-Based Ionic Liquids". *Journal of Chemical & Engineering Data* **59** (2014): 1955–1963.

[Apa79] G. Apai, J. F. Hamilton, J. Stohr, and A. Thompson. "Extended X-Ray-Absorption Fine Structure of Small Cu and Ni Clusters: Binding-Energy and Bond-Length Changes with Cluster Size". *Physical Review Letters* **43** (1979): 165–169.

[Ast05] D. Astruc, F. Lu, and J. R. Aranzaes. "Nanoparticles as Recyclable Catalysts: The Frontier between Homogeneous and Heterogeneous Catalysis". *Angewandte Chemie International Edition* **44** (2005): 7852–7872.

[Att99] D. Attwood. *Soft X-rays and Extreme Ultraviolet Radiation*. Cambridge University Press, 1999. ISBN: 9781139164429.

[Bat14] Z. Batsoev. "Messungen zur Strömung und Materialverteilung in einer Walze für die Clusterdeposition in Flüssigkeiten". Bachelor thesis. TU Dortmund, 2014.

[Baz97] D. Bazin, D. Sayers, J. J. Rehr, and C. Mottet. "Numerical Simulation of the Platinum LIII Edge White Line Relative to Nanometer Scale Clusters". *Journal of Physical Chemistry B* **101** (1997): 5332–5336.

[Ber10] M. J. Berger, J. H. Hubbell, J. Chang, J. S. Coursey, R. Sukumar, D. S. Zucker, and K. Olsen. *XCOM: Photon Cross Section Database*. 2010. URL: `https://www.nist.gov/pml/xcom-photon-cross-sections-database` (visited on 08/26/2017).

[Ber91] K. J. Berg, A. Berger, and H. Hofmeister. "Small silver particles in glass surface layers produced by sodium-silver ion exchange - their concentration and size depth profile". *Zeitschrift für Physik D Atoms, Molecules and Clusters* **20** (1991): 309–311.

[Bil03] I. Billard, G. Moutiers, A. Labet, A. El Azzi, C. Gaillard, C. Mariet, and K. Lützenkirchen. "Stability of Divalent Europium in an Ionic Liquid: Spectroscopic Investigations in 1-Methyl-3-butylimidazolium Hexafluorophosphate". *Inorganic Chemistry* **42** (2003): 1726–1733.

[Boh98] C. F. Bohren and D. R. Huffman. *Absorption and Scattering of Light by Small Particles*. Weinheim, Germany: Wiley-VCH Verlag GmbH, 1998. ISBN: 9783527618156.

[Bun09] O. Bunău and Y. Joly. "Self-consistent aspects of x-ray absorption calculations". *Journal of Physics: Condensed Matter* **21** (2009): 345501–345512.

[Bun10] G. Bunker. *Introduction to XAFS*. Cambridge: Cambridge University Press, 2010, ISBN: 9780511809194.

[Bün13] T. Büning. "Einfluss von Temperatur und Druck auf die supramolekulare Struktur langkettiger Alkohole". PhD thesis. TU Dortmund, 2013.

[Bun83] G. Bunker. "Application of the ratio method of EXAFS analysis to disordered systems". *Nuclear Instruments and Methods in Physics Research* **207** (1983): 437–444.

[Cal13] S. Calvin. *XAFS for Everyone*. Boca Raton, FL: CRC Press, Taylor and Francis Group, 2013, ISBN: 9781439878637.

[Cim09] V. Cimpeanu, M. Kočevar, V. I. Parvulescu, and W. Leitner. "Preparation of Rhodium Nanoparticles in Carbon Dioxide Induced Ionic Liquids and their Application to Selective Hydrogenation". *Angewandte Chemie International Edition* **48** (2009): 1085–1088.

[Cla00] B. S. Clausen and J. K. Nørskov. "Asymmetric pair distribution functions in catalysts". *Topics in Catalysis* **10** (2000): 221–230.

[Cre08] T. Cremer, M. Killian, J. M. Gottfried, N. Paape, P. Wasserscheid, F. Maier, and H.-P. Steinrück. "Physical Vapor Deposition of [EMIM][Tf2N]: A New Approach to the Modification of Surface Properties with Ultrathin Ionic Liquid Films". *ChemPhysChem* **9** (2008): 2185–2190.

[Cri12] J. C. Crittenden, R. R. Trussell, D. W. Hand, K. J. Howe, and G. Tchobanoglous. *MWH's Water Treatment*. Vol. 2. 4. Hoboken, NJ, USA: John Wiley & Sons, Inc., 2012: ISBN: 9781118131473.

[Das09] P. Dash and R. W. J. Scott. "1-Methylimidazole stabilization of gold nanoparticles in imidazolium ionic liquids". *Chemical Communications* (2009), 812–814.

[Das10] P. Dash, S. M. Miller, and R. W. Scott. "Stabilizing nanoparticle catalysts in imidazolium-based ionic liquids: A comparative study". *Journal of Molecular Catalysis A: Chemical* **329** (2010): 86–95.

[Dav25] W. P. Davey. "Precision Measurements of the Lattice Constants of Twelve Common Metals". *Physical Review* **25** (1925): 753–761.

[Dav39] E. David. "Deutung der Anomalien der optischen Konstanten dünner Metallschichten". *Zeitschrift für Physik* **114** (1939): 389–406.

[Deb01] P. G. Debenedetti and F. H. Stillinger. "Supercooled liquids and the glass transition". *Nature* **410** (2001): 259–267.

[Der93] B. Derjaguin and L. Landau. "Theory of the stability of strongly charged lyophobic sols and of the adhesion of strongly charged particles in solutions of electrolytes". *Progress in Surface Science* **43** (1993): 30–59.

[Des01] R. R. Deshmukh, R. Rajagopal, and K. V. Srinivasan. "Ultrasound promoted C–C bond formation: Heck reaction at ambient conditions in room temperature ionic liquids". *Chemical Communications* (2001), 1544–1545.

[DES12] DESY Photon Science. *PETRA III extension project: Beamlines P64/P65 for X-ray absorption spectroscopy. Technical design report*. 2012.

[Did03] S. V. Didziulis, K. D. Butcher, and S. S. Perry. "Small Cluster Models of the Surface Electronic Structure and Bonding Properties of Titanium Carbide, Vanadium Carbide, and Titanium Nitride". *Inorganic Chemistry* **42** (2003): 7766–7781.

[Dru00] P. Drude. "Zur Elektronentheorie der Metalle". *Annalen der Physik* **306** (1900): 566–613.

[Dup02] J. Dupont, G. S. Fonseca, A. P. Umpierre, P. F. P. Fichtner, and S. R. Teixeira. "Transition-Metal Nanoparticles in Imidazolium Ionic Liquids: Recycable Catalysts for Biphasic Hydrogenation Reactions". *Journal of the American Chemical Society* **124** (2002): 4228–4229.

[Dup10] J. Dupont and J. D. Scholten. "On the structural and surface properties of transition metal nanoparticles in ionic liquids". *Chemical Society Reviews* **39** (2010): 1780–1804.

[Ear06] M. J. Earle, J. M. Esperança, M. A. Gilea, J. N. Canongia Lopes, L. P. Rebelo, J. W. Magee, K. R. Seddon, and J. A. Widegren. "The distillation and volatility of ionic liquids". *Nature* **439** (2006): 831–834.

[Eas05] J. Eastoe. "Surfactant Aggregation and Adsorption at Interfaces". In: *Colloid Science. Principles, methods and applications*. Ed. by T. Cosgrove. Oxford, UK: Blackwell Publishing Ltd., 2005. Chap. 4, 50–74. ISBN: 9781444305395.

[Ech81] O. Echt, K. Sattler, and E. Recknagel. "Magic Numbers for Sphere Packings: Experimental Verification in Free Xenon Clusters". *Physical Review Letters* **47** (1981): 1121–1124.

[Ehr62] H. Ehrenreich and H. R. Philipp. "Optical Properties of Ag and Cu". *Physical Review* **128** (1962): 1622–1629.

[Eng14] D. C. Engemann. "Silver clusters deposited into polymers , aerogels and ionic liquids studied with X-ray and optical spectroscopy". PhD thesis. TU Dortmund, 2014.

[Eng16] D. C. Engemann, S. Roese, and H. Hövel. "Preformed 2 nm Ag Clusters Deposited into Ionic Liquids: Stabilization by Cation-Cluster Interaction". *The Journal of Physical Chemistry C* **120** (2016): 6239–6245.

[Fer09] S. C. Fernandes, S. K. Moccelini, C. W. Scheeren, P. Migowski, J. Dupont, M. Heller, G. A. Micke, and I. C. Vieira. "Biosensor for chlorogenic acid based on an ionic liquid containing iridium nanoparticles and polyphenol oxidase". *Talanta* **79** (2009): 222–228.

[Fon04] G. S. Fonseca, J. D. Scholten, and J. Dupont. “Iridium Nanoparticles Prepared in Ionic Liquids: An Efficient Catalytic System for the Hydrogenation of Ketones”. *Synlett* (2004), 1525–1528.

[Fra58] C. v. Fragstein and H. Römer. “Über die Anomalie der optischen Konstanten”. *Zeitschrift für Physik* **151** (1958): 54–71.

[Fra85] F. Frank, W. Schulze, B. Tesche, J. Urban, and B. Winter. “Formation of metal clusters and molecules by means of the gas aggregation technique and characterisation of size distribution”. *Surface Science* **156** (1985): 90–99.

[Fre04] C. P. Fredlake, J. M. Crosthwaite, D. G. Hert, S. N. V. K. Aki, and J. F. Brennecke. “Thermophysical Properties of Imidazolium-Based Ionic Liquids”. *Journal of Chemical & Engineering Data* **49** (2004): 954–964.

[Fre10] M. Freemantle. *An Introduction to Ionic Liquids*. RSC Publishing, 2010. ISBN: 978-1-84755-161-0.

[Fri77] C. Friedel and J. M. Crafts. “Sur une nouvelle méthode générale de synthèse d’hydrocarbures, d’acétones, etc.” *Comptes rendus des séances* **84** (1877): 1392.

[Fu17] F. Fu, Y. Li, Z. Yang, G. Zhou, Y. Huang, Z. Wan, X. Chen, N. Hu, W. Li, and L. Huang. “Molecular-Level Insights into Size-Dependent Stabilization Mechanism of Gold Nanoparticles in 1-Butyl-3-methylimidazolium Tetrafluoroborate Ionic Liquid”. *The Journal of Physical Chemistry C* **121** (2017): 523–532.

[Gab88] S. Gabriel and J. Weiner. “Ueber einige Abkömmlinge des Propylamins”. *Ber. dtsch. Chem. Ges* **21** (1888): 2226.

[Gal99] P. Galletto, P. F. Brevet, H. H. Girault, R. Antoine, and M. Broyer. “Enhancement of the Second Harmonic Response by Adsorbates on Gold Colloids: The Effect of Aggregation”. *The Journal of Physical Chemistry B* **103** (1999): 8706–8710.

[Gao15] J. Gao, R. S. Ndong, M. B. Shiflett, and N. J. Wagner. “Creating Nanoparticle Stability in Ionic Liquid [C4mim][BF4] by Inducing Solvation Layering”. *ACS Nano* **9** (2015): 3243–3253.

[Gér82] J. M. Gérardy and M. Ausloos. “Absorption spectrum of clusters of spheres from the general solution of Maxwell’s equations. II. Optical properties of aggregated metal spheres”. *Physical Review B* **25** (1982): 4204–4229.

[Gla07] D. Glasner and A. I. Frenkel. “Geometrical Characteristics of Regular Polyhedra: Application to EXAFS Studies of Nanoclusters”. In: *AIP Conference Proceedings*. Vol. 882. 1. AIP, 2007: pp. 746–748. ISBN: 0735403848.

[Gor77] M. Gordon, F. Cyrot-Lackmann, and M. Desjonquéres. “On the influence of size and roughness on the electronic structure of transition metal surfaces”. *Surface Science* **68** (1977): 359–367.

[Gri04] D. J. Griffiths. *Introduction to Quantum Mechanics*. Prentice Hall International, 2004.

[Gsp86] J. Gspann. “On the phase of metal clusters”. *Zeitschrift für Physik D Atoms, Molecules and Clusters* **3** (1986): 143–145.

[Gwi08] E. G. Gwinn, P. O'Neill, A. J. Guerrero, D. Bouwmeester, and D. K. Fygenson. "Sequence-Dependent Fluorescence of DNA-Hosted Silver Nanoclusters". *Advanced Materials* **20** (2008): 279–283.

[Hab06] H. Haberland, K. Kleinermanns, and F. Träger. "Cluster". In: *Bergmann Schäfer, Lehrbuch der Experimentalphysik, Band 5, Gase, Nanosysteme, Flüssigkeiten*. Ed. by K. Kleinermanns. Walter de Guyter GmbH & Co. KG, 10785 Berlin, 2006. Chap. 9, 817–976. ISBN: 978-3-11-017484-7.

[Hab91] H. Haberland, M. Karrais, and M. Mall. "A new type of cluster and cluster ion source". *Zeitschrift für Physik D Atoms, Molecules and Clusters* **20** (1991): 413–415.

[Hae04] A. J. Haes, W. P. Hall, L. Chang, W. L. Klein, and R. P. Van Duyne. "A Localized Surface Plasmon Resonance Biosensor: First Steps toward an Assay for Alzheimer's Disease". *Nano Letters* **4** (2004): 1029–1034.

[Ham58a] W. Hampe. "Beitrag zur Deutung der anomalen optischen Eigenschaften feinstteiliger Metallkolloide in großer Konzentration. I: Bestimmung des Füllfaktors dünner Schichten eines Kolloids Gold-SiO2". *Zeitschrift für Physik* **152** (1958): 470–475.

[Ham58b] W. Hampe. "Beitrag zur Deutung der anomalen optischen Eigenschaften feinstteiliger Metallkolloide in großer Konzentration. II: Experimentelle Ermittung einer Absorptionskurve und Deutung des Absorptionsmechanismus des Systems Gold-SiO2". *Zeitschrift für Physik* **152** (1958): 476–494.

[Han10] R. M. Hanson. "Jmol-a paradigm shift in crystallographic visualization". *Journal of Applied Crystallography* **43** (2010): 1250–1260.

[Har05] K. R. Harris, L. A. Woolf, and M. Kanakubo. "Temperature and Pressure Dependence of the Viscosity of the Ionic Liquid 1-Butyl-3-methylimidazolium Hexafluorophosphate". *Journal of Chemical & Engineering Data* **50** (2005): 1777–1782.

[Har06] K. R. Harris, M. Kanakubo, and L. A. Woolf. "Temperature and pressure dependence of the viscosity of the ionic liquids 1-methyl-3-octylimidazolium hexafluorophosphate and 1-methyl-3-octylimidazolium tetrafluoroborate". *Journal of Chemical and Engineering Data* **51** (2006): 1161–1167.

[Hat10] Y. Hatakeyama, S. Takahashi, and K. Nishikawa. "Can Temperature Control the Size of Au Nanoparticles Prepared in Ionic Liquids by the Sputter Deposition Technique?" *The Journal of Physical Chemistry C* **114** (2010): 11098–11102.

[He15] Z. He and P. Alexandridis. "Nanoparticles in ionic liquids: interactions and organization". *Phys. Chem. Chem. Phys.* **17** (2015): 18238–18261.

[Hei84] W. Heitler. *The Quantum Theory of Radiation*. Dover Books on Physics, 1984, ISBN: 978-0486645582.

[Hen09] S. Hennes. "Herstellung und Charakterisierung von Clustern in einer Überschallexpansion". Diploma thesis. TU Dortmund, 2009.

[Hen93] B. Henke, E. Gullikson, and J. Davis. "X-Ray Interactions: Photoabsorption, Scattering, Transmission, and Reflection at E = 50-30,000 eV, Z = 1-92". *Atomic Data and Nuclear Data Tables* **54** (1993): 181–342.

[Hil01a] A. Hilger. "Grenzflächen-Analyse durch Mie-Plasmon-Spektroskopie an Edelmetallclustern". PhD thesis. RWTH Aachen, 2001.

[Hil01b] A. Hilger, M. Tenfelde, and U. Kreibig. "Silver nanoparticles deposited on dielectric surfaces". *Applied Physics B: Lasers and Optics* **73** (2001): 361–372.

[Hof12] S. Hoffmann. "Structure and electronic properties of supported noble metal clusters". PhD thesis. TU Dortmund, 2012.

[Hol08] J. D. Holbrey, R. D. Rogers, R. A. Mantz, P. C. Trulove, V. A. Cocalia, A. E. Visser, J. L. Anderson, J. L. Anthony, J. F. Brennecke, E. J. Maginn, T. Welton, and R. A. Mantz. "Physicochemical Properties". In: *Ionic Liquids in Synthesis*. Ed. by P. Wasserscheid and T. Welton. 1st ed. Weinheim, Germany: Wiley-VCH Verlag GmbH & Co. KGaA, 2008. Chap. 3, 57–174. ISBN: 9783527312399.

[Höv93] H. Hövel, S. Fritz, A. Hilger, U. Kreibig, and M. Vollmer. "Width of cluster plasmon resonances: Bulk dielectric functions and chemical interface damping". *Physical Review B* **48** (1993): 18178–18188.

[Höv95] H. Hövel. "Grenzflächeneigenschaften von Metallclustern". PhD thesis. RWTH Aachen, 1995.

[Ins] P. Instruments. *Abbe Refractometer Operating Manual*. URL: `https://de.scribd.com/document/195063358/Ba-Abbe-Refraktometer-Ar4` (visited on 05/29/2016).

[Ito04] H. Itoh, K. Naka, and Y. Chujo. "Synthesis of Gold Nanoparticles Modified with Ionic Liquid Based on the Imidazolium Cation". *Journal of the American Chemical Society* **126** (Mar. 2004): 3026–3027.

[Jan13] C. Janiak. "Ionic Liquids for the Synthesis and Stabilization of Metal Nanoparticles". *Zeitschrift für Naturforschung B* **68** (2013): 1059–1089.

[Jen12] R. Jenkins. "X-Ray Diffraction". In: *X-Ray Fluorescence Spectrometry*. Hoboken, NJ, USA: John Wiley & Sons, Inc., 2012, 37–51. ISBN: 978-0-471-29942-4.

[Jen99] A. Jentys. "Estimation of mean size and shape of small metal particles by EXAFS". *Physical Chemistry Chemical Physics* **1** (1999): 4059–4063.

[Joh72] P. B. Johnson and R. W. Christy. "Optical constants of the noble metals". *Physical Review B* **6** (1972): 4370–4379.

[Jon75] R. Jones, P. Jennings, and G. Painter. "Cluster calculations of the electronic structure of transition metal surfaces". *Surface Science* **53** (1975): 409–428.

[Kam10] T. Kameyama, Y. Ohno, T. Kurimoto, K.-i. Okazaki, T. Uematsu, S. Kuwabata, and T. Torimoto. "Size control and immobilization of gold nanoparticles stabilized in an ionic liquid on glass substrates for plasmonic applications". *Phys. Chem. Chem. Phys.* **12** (2010): 1804–1811.

[Kha10a] V. Khare, A. Kraupner, A. Mantion, A. Jeličić, A. F. Thünemann, C. Giordano, and A. Taubert. "Stable Iron Carbide Nanoparticle Dispersions in [Emim][SCN] and [Emim][N(CN)2] Ionic Liquids". *Langmuir* **26** (2010): 10600–10605.

[Kha10b] V. Khare, Z. Li, A. Mantion, A. A. Ayi, S. Sonkaria, A. Voelkl, A. F. Thünemann, and A. Taubert. "Strong anion effects on gold nanoparticle formation in ionic liquids". *J. Mater. Chem.* **20** (2010): 1332–1339.

[Koe05] M. Koel. "Ionic Liquids in Chemical Analysis". *Critical Reviews in Analytical Chemistry* **35** (2005): 177–192.

[Kon00] D. C. Koningsberger, B. L. Mojet, G. E. V. Dorssen, and D. E. Ramaker. "XAFS spectroscopy; fundamental principles and data analysis". *Topics in Catalysis* **10** (2000): 143–155.

[Kon17] A. Kononov. "Sputterdeposition von Gold- und Silbernanopartikeln in ionischer Flüssigkeit: Spektroskopie der Plasmonanregungen". Master thesis. TU Dortmund, 2017.

[Kon88] D. Koningsberger and R. Prins, eds. *X-Ray Absorption: Principles, Applications, Techniques of EXAFS, SEXAFS and XANES*. New York - Chichester - Brisbane - Toronto - Singapore: John Wiley + Sons, 1988. ISBN: 0-471-87547-3.

[Kow08] M. H. Kowsari, S. Alavi, M. Ashrafizaadeh, and B. Najafi. "Molecular dynamics simulation of imidazolium-based ionic liquids. I. Dynamics and diffusion coefficient". *The Journal of Chemical Physics* **129** (2008): 224508.

[Kra11] A. Kraynov and T. E. Müller. "Concepts for the stabilization of metal nanoparticles in ionic liquids". *Applications of Ionic Liquids in Science and Technology* (2011), 1–27.

[Kre69] U. Kreibig and C. v. Fragstein. "The limitation of electron mean free path in small silver particles". *Zeitschrift für Physik* **224** (1969): 307–323.

[Kre97] U. Kreibig. *Handbook of optical properties Vol. II: Optics of small particles, interfaces and surfaces*. Ed. by P. Hummel and R. Wissmann. Boca Raton, FL: CRC Press, 1997,

[Küp85] J. Küppers. "Auger-Effekt: Auger Electron Spectroscopy". *Nachrichten aus Chemie, Technik und Laboratorium* **33** (1985). Ed. by J. Küppers: 726–727.

[Kuw10] S. Kuwabata, T. Tsuda, and T. Torimoto. "Room-Temperature Ionic Liquid. A New Medium for Material Production and Analyses under Vacuum Conditions". *The Journal of Physical Chemistry Letters* **1** (2010): 3177–3188.

[Lei16] J. Leinonen. *PyMieCoated*. 2016. URL: `https://github.com/jleinonen/pymiecoated` (visited on 03/21/2017).

[Lia07] Y. Liang, N. Hilal, P. Langston, and V. Starov. "Interaction forces between colloidal particles in liquid: Theory and experiment". *Advances in Colloid and Interface Science* **134-135** (2007): 151–166.

[Lip17] F. Lippert. "Aggregationsverhalten von Metallclustern in unterschiedlichen ionischen Flüssigkeiten". Master thesis. TU Dortmund, 2017.

[Liu13] X. Liu, F. Wang, A. Niazov-Elkan, W. Guo, and I. Willner. "Probing Biocatalytic Transformations with Luminescent DNA/Silver Nanoclusters". *Nano Letters* **13** (2013): 309–314.

[Loc08] V. Lockett, R. Sedev, J. Ralston, M. Horne, and T. Rodopoulos. "Differential Capacitance of the Electrical Double Layer in Imidazolium-Based Ionic Liquids: Influence of Potential, Cation Size, and Temperature". *The Journal of Physical Chemistry C* **112** (2008): 7486–7495.

[Lóp07] I. López-Martin, E. Burello, P. N. Davey, K. R. Seddon, and G. Rothenberg. "Anion and Cation Effects on Imidazolium Salt Melting Points: A Descriptor Modelling Study". *ChemPhysChem* **8** (2007): 690–695.

[Lu12] Y. Lu and W. Chen. "Size effect of silver nanoclusters on their catalytic activity for oxygen electro-reduction". *Journal of Power Sources* **197** (2012): 107–110.

[Lyk05] J. Lyklema. "Vol. IV Particulate colloids". In: *Fundamentals of Interface and Colloid Science:* Amsterdam: Elsevier, 2005. ISBN: 9780080454399.

[Mac07] D. R. MacFarlane and K. R. Seddon. "Ionic Liquids - Progress on the Fundamental Issues". *Australian Journal of Chemistry* **60** (2007): 3–5.

[Mac62] A. L. Mackay. "A dense non-crystallographic packing of equal spheres". *Acta Crystallographica* **15** (1962): 916–918.

[Mar16] L. A. Martín Montoya. "Automatic reduction of large x-ray fluorescence datasets applied to XAS and mapping experiments". PhD thesis. Universität Paderborn, 2016.

[Mie08] G. Mie. "Beiträge zur Optik trüber Medien, speziell kolloidaler Metallösungen". *Annalen der Physik* **330** (1908): 377–445.

[Mor02] I. D. Morrison and S. Ross. *Colloidal Dispersions: Suspensions, Emulsions, and Foams*. Wiley- Interscience, New York, 2002. ISBN: 978-0-471-17625-1.

[Nam76] N. Nambu, N. Hiraoka, K. Shigemura, S. Hamanaka, and M. Ogawa. "A Study of the 1,3,5-Trialkylbenzenes with Aluminum Chloride-Hydrogen Chloride Systems". *Bulletin of the Chemical Society of Japan* **49** (1976): 3637–3640.

[Nel02] W. M. Nelson. "Are Ionic Liquids Green Solvents?" In: *Ionic Liquids*. Ed. by R. D. Rogers and K. R. Seddon. Vol. 818. ACS Symposium Series. Washington, DC: American Chemical Society, July 2002: 30–41. ISBN: 0-8412-3789-1.

[New01] M. Newville. "EXAFS analysis using FEFF and FEFFIT". *Journal of Synchrotron Radiation* **8** (Mar. 2001): 96–100.

[New08] M. Newville. *Fundamentals of XAFS*. 2008. URL: `http://xafs.org/Tutorials?action=AttachFile%7B%5C&%7Ddo=get%7B%5C&%7Dtarget=Newville%7B%5C_%7Dxas%7B%5C_%7Dfundamentals.pdf` (visited on 12/12/2016).

[New13] M. Newville. "Larch: An Analysis Package for XAFS and Related Spectroscopies". *Journal of Physics: Conference Series* **430** (2013): 012007.

[New93] M. Newville, P. Līviņš, Y. Yacoby, J. J. Rehr, and E. A. Stern. "Near-edge x-ray-absorption fine structure of Pb: A comparison of theory and experiment". *Physical Review B* **47** (1993): 14126–14131.

[New95] M. Newville, B. Ravel, D. Haskel, J. Rehr, E. Stern, and Y. Yacoby. "Analysis of multiple-scattering XAFS data using theoretical standards". *Physica B: Condensed Matter* **208-209** (1995): 154–156.

[Nod82] K. Noda, M. Ohashi, and K. Ishida. "Viscosities and densities at 298.15 K for mixtures of methanol, acetone, and water". *Journal of Chemical & Engineering Data* **27** (1982): 326–328.

[Oli09] F. C. C. Oliveira, L. M. Rossi, R. F. Jardim, and J. C. Rubim. "Magnetic Fluids Based on γ-Fe 2 O 3 and CoFe 2 O 4 Nanoparticles Dispersed in Ionic Liquids". *The Journal of Physical Chemistry C* **113** (2009): 8566–8572.

[ONe09] P. R. O'Neill, L. R. Velazquez, D. G. Dunn, E. G. Gwinn, and D. K. Fygenson. "Hairpins with Poly-C Loops Stabilize Four Types of Fluorescent Ag n :DNA". *The Journal of Physical Chemistry C* **113** (2009): 4229–4233.

[Ott05] L. S. Ott, M. L. Cline, M. Deetlefs, K. R. Seddon, and R. G. Finke. "Nanoclusters in Ionic Liquids: Evidence for N -Heterocyclic Carbene Formation from Imidazolium-Based Ionic Liquids Detected by 2 H NMR". *Journal of the American Chemical Society* **127** (2005): 5758–5759.

[Pau03] Y. U. Paulechka, G. J. Kabo, A. V. Blokhin, O. A. Vydrov, J. W. Magee, and M. Frenkel. "Thermodynamic Properties of 1-Butyl-3-methylimidazolium Hexafluorophosphate in the Ideal Gas State". *Journal of Chemical & Engineering Data* **48** (2003): 457–462.

[Pau05] A. Paul, P. K. Mandal, and A. Samanta. "How transparent are the imidazolium ionic liquids? A case study with 1-methyl-3-butylimidazolium hexafluorophosphate, [bmim][PF6]". *Chemical Physics Letters* **402** (2005): 375–379.

[Pel07] G. Pellegrini, G. Mattei, V. Bello, and P. Mazzoldi. "Interacting metal nanoparticles: Optical properties from nanoparticle dimers to core-satellite systems". *Materials Science and Engineering: C* **27** (2007): 1347–1350.

[Per93] B. Persson. "Polarizability of small spherical metal particles: influence of the matrix environment". *Surface Science* **281** (1993): 153–162.

[PET17] PETRAIII. *PETRA III faculty informaion*. 2017. URL: `http://photon-science.desy.de/facilities/petra%7B%5C_%7Diii/facility%7B%5C_%7Dinformation/index%7B%5C_%7Deng.html` (visited on 09/20/2017).

[Pis06] D. Pissuwan, S. M. Valenzuela, and M. B. Cortie. "Therapeutic possibilities of plasmonically heated gold nanoparticles". *Trends in Biotechnology* **24** (2006): 62–67.

[Ple08] N. V. Plechkova and K. R. Seddon. "Applications of ionic liquids in the chemical industry". *Chem. Soc. Rev.* **37** (2008): 123–150.

[Pri12] S. W. T. Price, N. Zonias, C.-K. Skylaris, T. I. Hyde, B. Ravel, and A. E. Russell. "Fitting EXAFS data using molecular dynamics outputs and a histogram approach". *Physical Review B* **85** (2012): 075439.

[Pus14] M. J. Pushie, I. J. Pickering, M. Korbas, M. J. Hackett, and G. N. George. "Elemental and Chemically Specific X-ray Fluorescence Imaging of Biological Systems". *Chemical Reviews* **114** (2014): 8499–8541.

[Qui11] M. Quinten. *Optical Properties of Nanoparticle Systems*. Weinheim, Germany: Wiley-VCH Verlag GmbH & Co. KGaA, Jan. 2011. ISBN: 9783527633135.

[Qui93] M. Quinten and U. Kreibig. "Absorption and elastic scattering of light by particle aggregates". *Applied Optics* **32** (1993): 6173–6182.

[Ras11] S. K. Rastogi, V. J. Rutledge, C. Gibson, D. A. Newcombe, J. R. Branen, and A. L. Branen. “Ag colloids and Ag clusters over EDAPTMS-coated silica nanoparticles: synthesis, characterization, and antibacterial activity against Escherichia coli”. *Nanomedicine: Nanotechnology, Biology and Medicine* **7** (2011): 305–314.

[Rav07] B. Ravel and S. D. Kelly. “The Difficult Chore of Measuring Coordination by EXAFS”. In: *AIP Conference Proceedings*. Vol. 882. AIP, 2007: pp. 150–152. ISBN: 0735403848.

[Red08] E. Redel, R. Thomann, and C. Janiak. “First Correlation of Nanoparticle Size-Dependent Formation with the Ionic Liquid Anion Molecular Volume”. *Inorganic Chemistry* **47** (2008): 14–16.

[Reh10] J. J. Rehr, J. J. Kas, F. D. Vila, M. P. Prange, and K. Jorissen. “Parameter-free calculations of X-ray spectra with FEFF9”. *Physical Chemistry Chemical Physics* **12** (2010): 5503.

[Reh13] J. J. Rehr. *Feff9.6 User’s Guide*. 2013. URL: `http://leonardo.phys.washington.edu/feff/Docs/feff9/feff90/feff90%7B%5C_%7Dusers%7B%5C_%7Dguide.pdf` (visited on 01/11/2015).

[Ric10] K. Richter, A. Birkner, and A.-V. Mudring. “Stabilizer-Free Metal Nanoparticles and Metal-Metal Oxide Nanocomposites with Long-Term Stability Prepared by Physical Vapor Deposition into Ionic Liquids”. *Angewandte Chemie International Edition* **49** (2010): 2431–2435.

[Ric11] K. Richter, A. Birkner, and A.-V. Mudring. “Stability and growth behavior of transition metal nanoparticles in ionic liquids prepared by thermal evaporation: how stable are they really?” *Physical Chemistry Chemical Physics* **13** (2011): 7136–7141.

[Rid74] J. A. Riddick, W. B. Bunger, and T. K. Sakano. “Organic Solvents: Physical Properties and Methods of Purification”. *Journal of Chromatographic Science* **12** (1974): 38A–38A.

[Roe16] S. Roese, D. Engemann, S. Hoffmann, K. Latussek, C. Sternemann, and H. Hövel. “PDMS embedded Ag clusters: Coalescence and cluster-matrix interaction”. *Journal of Physics: Conference Series* **712** (2016): 012068.

[Rol10a] B. Roldan Cuenya, A. I. Frenkel, S. Mostafa, F. Behafarid, J. R. Croy, L. K. Ono, and Q. Wang. “Anomalous lattice dynamics and thermal properties of supported size- and shape-selected Pt nanoparticles”. *Physical Review B* **82** (2010): 155450.

[Rol10b] B. Roldan Cuenya, J. R. Croy, S. Mostafa, F. Behafarid, L. Li, Z. Zhang, J. C. Yang, Q. Wang, and A. I. Frenkel. “Solving the Structure of Size-Selected Pt Nanocatalysts Synthesized by Inverse Micelle Encapsulation”. *Journal of the American Chemical Society* **132** (2010): 8747–8756.

[Rub08] J. C. Rubim, F. A. Trindade, M. A. Gelesky, R. F. Aroca, and J. Dupont. “Surface-Enhanced Vibrational Spectroscopy of Tetrafluoroborate 1- n -Butyl-3-methylimidazolium (BMIBF4) Ionic Liquid on Silver Surfaces”. *The Journal of Physical Chemistry C* **112** (2008): 19670–19675.

[San09] S. I. Sanchez, L. D. Menard, A. Bram, J. H. Kang, M. W. Small, R. G. Nuzzo, and A. I. Frenkel. "The Emergence of Nonbulk Properties in Supported Metal Clusters: Negative Thermal Expansion and Atomic Disorder in Pt Nanoclusters Supported on γ-Al2O3". *Journal of the American Chemical Society* **131** (2009): 7040–7054.

[San99] A. Sanchez, S. Abbet, U. Heiz, W.-D. Schneider, H. Häkkinen, R. N. Barnett, and U. Landman. "When Gold Is Not Noble: Nanoscale Gold Catalysts". *The Journal of Physical Chemistry A* **103** (1999): 9573–9578.

[Sch07] H. S. Schrekker, M. A. Gelesky, M. P. Stracke, C. M. Schrekker, G. Machado, S. R. Teixeira, J. C. Rubim, and J. Dupont. "Disclosure of the imidazolium cation coordination and stabilization mode in ionic liquid stabilized gold(0) nanoparticles". *Journal of Colloid and Interface Science* **316** (2007): 189–195.

[Sed00] K. R. Seddon, A. Stark, and M.-J. Torres. "Influence of chloride, water, and organic solvents on the physical properties of ionic liquids". *Pure and Applied Chemistry* **72** (2000): 2275–2287.

[Sei91] M. Seidl, K. Meiwes-Broer, and M. Brack. "Finite-size effects in ionization potentials and electron affinities of metal clusters". *The Journal of Chemical Physics* **95** (1991): 1295–1303.

[Shi00] A. N. Shipway, E. Katz, and I. Willner. "Nanoparticle arrays on surfaces for electronic, optical, and sensor applications". *ChemPhysChem* **1** (2000): 18–52.

[Sla07] J. M. Slattery, C. Daguenet, P. J. Dyson, T. J. S. Schubert, and I. Krossing. "How to Predict the Physical Properties of Ionic Liquids: A Volume-Based Approach". *Angewandte Chemie International Edition* **46** (2007): 5384–5388.

[Sme05] A. B. Smetana, K. J. Klabunde, and C. M. Sorensen. "Synthesis of spherical silver nanoparticles by digestive ripening, stabilization with various agents, and their 3-D and 2-D superlattice formation". *Journal of Colloid and Interface Science* **284** (2005): 521–526.

[Ste75] E. A. Stern, D. E. Sayers, and F. W. Lytle. "Extended x-ray-absorption fine-structure technique. III. Determination of physical parameters". *Physical Review B* **11** (1975): 4836–4846.

[Sug15] D. Sugioka, T. Kameyama, S. Kuwabata, and T. Torimoto. "Single-step preparation of two-dimensionally organized gold particles via ionic liquid/metal sputter deposition". *Phys. Chem. Chem. Phys.* **17** (2015): 13150–13159.

[Sup01] P. Supaphol and J. Spruiell. "Isothermal melt- and cold-crystallization kinetics and subsequent melting behavior in syndiotactic polypropylene: a differential scanning calorimetry study". *Polymer* **42** (2001): 699–712.

[Suz09] T. Suzuki, K.-i. Okazaki, T. Kiyama, S. Kuwabata, and T. Torimoto. "A Facile Synthesis of AuAg Alloy Nanoparticles Using a Chemical Reaction Induced by Sputter Deposition of Metal onto Ionic Liquids". *Electrochemistry* **77** (2009): 636–638.

[Swa03] R. P. Swatloski, J. D. Holbrey, and R. D. Rogers. "Ionic liquids are not always green: hydrolysis of 1-butyl-3-methylimidazolium hexafluorophosphate". *Green Chemistry* **5** (2003): 361–363.

[Tam11] Y. Tamenori, M. Morita, and T. Nakamura. "Two-dimensional approach to fluorescence yield XANES measurement using a silicon drift detector". *Journal of Synchrotron Radiation* **18** (2011): 747–752.

[Tan12] D. Tang, Z. Chen, J. Hu, G. Sun, S. Lu, and C. Hu. "CO oxidation catalyzed by silver nanoclusters: mechanism and effects of charge". *Physical Chemistry Chemical Physics* **14** (2012): 12829–12837.

[Tan74] N. Taniguchi. "On the basic concept of 'nano-technology'". *Proceedings of International Conference Production Engineering, Tokyo, Part II, Japan Society of Precision Engineering* **245** (1974).

[Teo86] B. K. Teo. *EXAFS: Basic Principles and Data Analysis*. Vol. 9. Inorganic Chemistry Concepts. Berlin, Heidelberg: Springer Berlin Heidelberg, 1986. ISBN: 978-3-642-50033-6.

[Tim17a] J. Timoshenko. *Private Communication*. 2017.

[Tim17b] J. Timoshenko and A. I. Frenkel. "Probing structural relaxation in nanosized catalysts by combining EXAFS and reverse Monte Carlo methods". *Catalysis Today* **280** (2017): 274–282.

[Tim17c] J. Timoshenko, D. Lu, Y. Lin, and A. I. Frenkel. "Supervised Machine-Learning-Based Determination of Three-Dimensional Structure of Metallic Nanoparticles". *The Journal of Physical Chemistry Letters* **8** (2017): 5091–5098.

[Tor06] T. Torimoto, K.-i. Okazaki, T. Kiyama, K. Hirahara, N. Tanaka, and S. Kuwabata. "Sputter deposition onto ionic liquids: Simple and clean synthesis of highly dispersed ultrafine metal nanoparticles". *Applied Physics Letters* **89** (2006): 243117.

[Tri06] A. Triolo, A. Mandanici, O. Russina, V. Rodriguez-Mora, M. Cutroni, C. Hardacre, M. Nieuwenhuyzen, H.-J. Bleif, L. Keller, and M. A. Ramos. "Thermodynamics, Structure, and Dynamics in Room Temperature Ionic Liquids: The Case of 1-Butyl-3-methyl Imidazolium Hexafluorophosphate ([bmim][PF6])". *The Journal of Physical Chemistry B* **110** (2006): 21357–21364.

[Uen08] K. Ueno, A. Inaba, M. Kondoh, and M. Watanabe. "Colloidal Stability of Bare and Polymer-Grafted Silica Nanoparticles in Ionic Liquids". *Langmuir* **24** (2008): 5253–5259.

[Van11] E. Vanecht, K. Binnemans, J. W. Seo, L. Stappers, and J. Fransaer. "Growth of sputter-deposited gold nanoparticles in ionic liquids". *Physical Chemistry Chemical Physics* **13** (2011): 13565–13571.

[Van12] E. Vanecht, K. Binnemans, S. Patskovsky, M. Meunier, J. W. Seo, L. Stappers, and J. Fransaer. "Stability of sputter-deposited gold nanoparticles in imidazolium ionic liquids". *Physical Chemistry Chemical Physics* **14** (2012): 5662–5671.

[Van16] C. Van Bokhoven, Jeroen A. Lamberti. *X-Ray Absorption and X-Ray Emission Spectroscopy*. Ed. by J. A. Van Bokhoven and C. Lamberti. Chichester, UK: John Wiley & Sons, Ltd, 2016. ISBN: 9781118844243.

[Ver47] E. J. W. Verwey. "Theory of the Stability of Lyophobic Colloids." *The Journal of Physical and Colloid Chemistry* **51** (1947): 631–636.

[Wal13] D. Walter. "Primary Particles - Agglomerates - Aggregates". In: *Nanomaterials*. Weinheim, Germany: Wiley-VCH Verlag GmbH & Co. KGaA, Apr. 2013, 9–24.

[Wal14] P. Walden. "Molecular weights and electrical conductivity of several fused salts". *Bull. Acad. Imper. Sci. (St. Petersburg)* (1914), 405–422.

[Wec04] E. Weckert. "PETRA III: A New High Brilliance Synchrotron Radiation Source at DESY". In: *AIP Conference Proceedings*. Vol. 705. AIP, 2004: pp. 73–76.

[Weg17] S. Wegner and C. Janiak. "Metal Nanoparticles in Ionic Liquids". *Topics in Current Chemistry* **375** (2017): 65.

[Wel12] E. Welter. "PETRA III extension project for X-ray absorption spectroscopy" (2012).

[Wid87] G. Widmann. "DSC of amorphous materials". *Thermochimica Acta* **112** (1987): 137–140.

[Wil92] J. S. Wilkes and M. J. Zaworotko. "Air and water stable 1-ethyl-3-methylimidazolium based ionic liquids". *Journal of the Chemical Society, Chemical Communications* (1992), 965.

[Yua13] X. Yuan, Y. Tay, X. Dou, Z. Luo, D. T. Leong, and J. Xie. "Glutathione-Protected Silver Nanoclusters as Cysteine-Selective Fluorometric and Colorimetric Probe". *Analytical Chemistry* **85** (2013): 1913–1919.

[Zha03] P. Zhang and T. K. Sham. "X-Ray Studies of the Structure and Electronic Behavior of Alkanethiolate-Capped Gold Nanoparticles: The Interplay of Size and Surface Effects". *Physical Review Letters* **90** (2003): 245502.

Acknowledgements

First of all, I would like to thank my supervisor Prof. Dr. Heinz Hövel. He gave me the opportunity to work independently and self-responsibly and I am grateful for inspiring discussions, the support in the lab and during beamtimes.

I am also very grateful to Prof. Dr. Manfred Bayer for his interest in my work and for being the second assessor and to Dr. Bärbel Siegmann and Prof. Dr. Mirko Cinchetti for completing the examination board.

I would like to thank Prof. Dr. Metin Tolan for giving me the opportunity to be a member at his chair and for all conferences I could attend and the experiences I could gather. Thanks to Dr. Christian Sternemann for his good advices and valuable discussions concerning the EXAFS beamtime preparation and data evaluation.

Thanks to Dr. David Engemann for introducing me into cluster physics and the operating instructions to THECLA. All the work in the lab would not have been possible without the help of several bachelor and master students. At this point my thanks go to Christian Albers, Zdravko Batsoev, Andreas Gruhn, Alexander Kononov and Florian Lippert. Dominik Wolter always stood in, when any help was needed.

I would like to thank Mirko Elbers, Dr. Holger Göhring, Alexander Kononov, Florian Lippert and Dominik Wolter for their support during the beamtimes. In this context I acknowledge the support of the local contact of P64, Dr. Vadim Murzin and of course the DESY machine group for providing synchrotron radiation. Dr. Ligia Marín Montoya helped me extracting the K_α peak from the fluorescence data. Dr. Wolfgang Caliebe made it possible start the XAS experiments during an inhouse beamtime in advance to a first regular beamtime. Thank you! Thanks to Mirko Elbers for sharing his experience and troubleshooting during my first steps of EXAFS fitting. Thanks to Dr. Janis Timoshenko and Prof. Dr. Anatoly Frenkel from Stony Brooks University, NY, for the fruitful collaboration and for providing the neural network based XANES analysis of my data.

Thanks to Susanne Kralemann and the mechanical workshop at the physics department of the TU Dortmund for producing the sample holders, mounting the tiny capillaries to the sample holder and for their reliable support concerning repairs. Further, I would like to thank Dirk Schemionek and Gisela Pike from the preparation laboratory for borrowing the peristaltic pump and their ideas and help to seal the pumping circuit.

For proofreading this thesis I thank Dr. Christian Sternemann, Karsten Köster, Dr. Petra Roese and Rudolf Roese.

I would like to thank Dominik Wolter, Dr. Holger Göhring, Dr. Paul Salmen and Dr. Julian Schulze for sharing an office (or at least the unoccupied chairs), having lunch, liters of coffee, tea, several Nimm2, for discussing physical topics, fun facts and news provided by Germany's largest daily newspaper. I am also thankful for the whole chair E1a good working atmosphere. Almost every day I liked to come to work (except for the days a new skimmer had to be built).

Throughout my years of study I met a lot of people that I had many good (and some strenuous) times with: Sebastian Brandt, Sebastian Clever, Frederik Herbst, Jan-Philipp Köhle, Thorben Menne and Janine Müller. One of us left forever much too early. Although Janine Müller got lost somewhere in the field of particle physics, from the first semester she has become very dear to my heart. Thanks for having our weekly coffee date!

Since kindergarten times I have my friend Inka Petrikowski at my side and I guess our ways won't separate. I am sure to have found a friend for life.

I would like to thank my parents for their love, for motivating me and for their unconditional support throughout my entire life. I am very grateful to Karsten. Thank you for making me smile, especially in times I need it the most.